AD-A142 342 HGCDTE SURFACE AND DEFECT STUDY PROGRAM(U) SANTA BARBARA RESEARCH CENTER GOLETA CALIF J A WILSON ET AL. JUL 83 SBRC-40497 MDA903-83-C-0108 1/2

UNCLASSIFIED F/G 20/12 NL

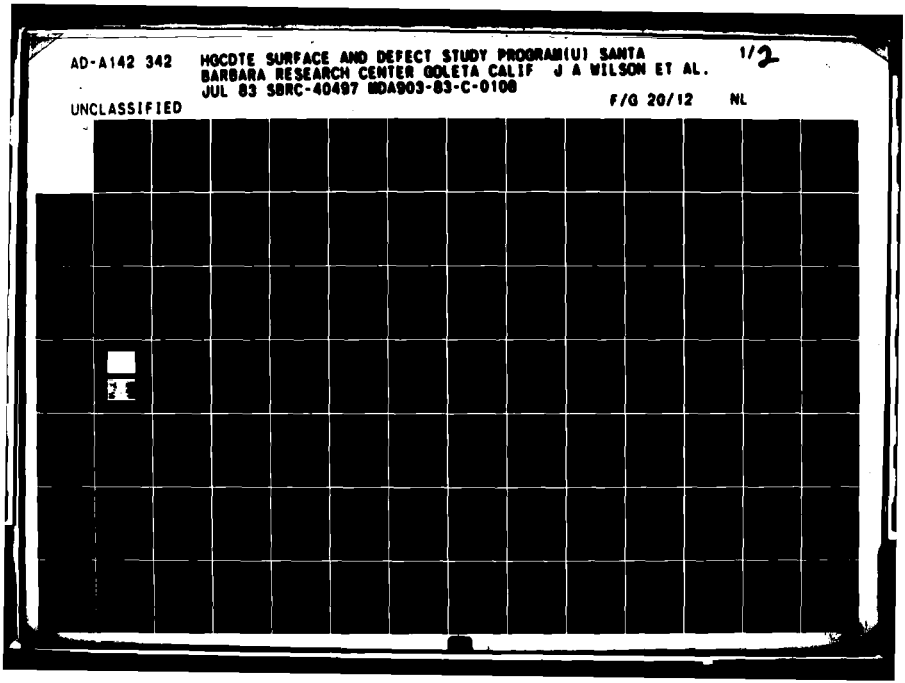

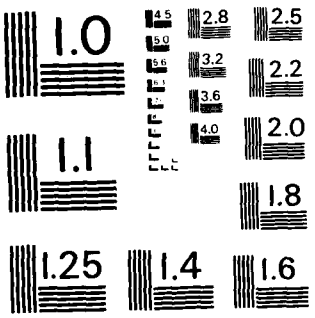

MICROCOPY RESOLUTION TEST CHART
NATIONAL BUREAU OF STANDARDS - 1963 - A

AD-A142 342

HgCdTe SURFACE AND DEFECT STUDY PROGRAM

J.A. Wilson
Santa Barbara Research Center
Goleta, CA 93117

W.E. Spicer, J.A. Silberman,
S. Cole, and D. Laser
Stanford Electronics Laboratories
Stanford, CA 94305

A. Sher
SRI International
Menlo Park, CA

R.G. Wilson
Hughes Research Laboratories
Malibu, CA

July 1983

INTERIM TECHNICAL REPORT

Contract No. MDA-903-83-C-0108

The views, opinions, and findings contained in this report are those of the authors and should not be construed as an official Department of Defense position, policy, or decision, unless so designated by other official documentation

Prepared for:
DARPA
1400 Wildon Blvd.
Arlington, Virginia 22209
Attention: Dr. Richard A. Reynolds
Material Science Division

DTIC FILE COPY

This document has been approved for public release and sale; its distribution is unlimited.

84 03 08 016

SECURITY CLASSIFICATION OF THIS PAGE (When Data Entered)

REPORT DOCUMENTATION PAGE

READ INSTRUCTIONS BEFORE COMPLETING FORM

1. REPORT NUMBER: 0002AC	2. GOVT ACCESSION NO.: AD-A142 342
3. RECIPIENT'S CATALOG NUMBER:	
4. TITLE (and Subtitle): HgCdTe Surface and Defect Study Program	5. TYPE OF REPORT & PERIOD COVERED: Interim Technical Report July 1983
	6. PERFORMING ORG. REPORT NUMBER: 40497
7. AUTHOR(s): Jerry A. Wilson, Joel Silberman, S. Cole, W.E. Spicer, D. Laser, A. Sher and R.G. Wilson	8. CONTRACT OR GRANT NUMBER(s): MDA-903-83-C-0108
9. PERFORMING ORGANIZATION NAME AND ADDRESS: SBRC, 75 Coromar Drive, Goleta, CA 93117 — Stanford Electronics Laboratories, Stanford, CA 94305	10. PROGRAM ELEMENT, PROJECT, TASK AREA & WORK UNIT NUMBERS:
11. CONTROLLING OFFICE NAME AND ADDRESS: Defense Advanced Research Project Administration, 1400 Wilson Blvd, Arlington, VA 22209	12. REPORT DATE: July 1983
	13. NUMBER OF PAGES:
14. MONITORING AGENCY NAME & ADDRESS (if different from Controlling Office): Night Vision and Electro-Optics Laboratory, NV&EOL-RD, Fort Belvoir, VA 22060	15. SECURITY CLASS. (of this report): Unclassified
	15a. DECLASSIFICATION/DOWNGRADING SCHEDULE:

16. DISTRIBUTION STATEMENT (of this Report)

17. DISTRIBUTION STATEMENT (of the abstract entered in Block 20, if different from Report)

18. SUPPLEMENTARY NOTES

19. KEY WORDS (Continue on reverse side if necessary and identify by block number)

HgCdTe, CdTe, HgTe, photoemission spectroscopy, electronic structure, interface states, DLTS, alloy bonding, capacitance voltage, implant, channeled implant, TEM, passivation.

20. ABSTRACT (Continue on reverse side if necessary and identify by block number)

This report presents results of the first six-month period of a three-year study of the surface and defects of HgCdTe.

In an investigation of MIS interfaces using Photox™ SiO_2 on HgCdTe, effects of the choice of gate metal composition are presented. Contribution to flatband bias, measured by capacitance voltage, of insulator fixed charge is determined. Effect of water on interface electrical and mechanical

DD FORM 1 JAN 73 1473 EDITION OF 1 NOV 65 IS OBSOLETE

SECURITY CLASSIFICATION OF THIS PAGE (When Data Entered)

properties are presented. Studies of the initial stages of oxidation of UHV cleaned HgCdTe using photoemission spectroscopy are presented. The effect of Hg bonding on ease of defect formation is discussed and using TEM, defects in bulk and LPE grown material are surveyed.

Detailed calculations of s, p and hybrid (sp^3) energies are presented for Hg, Cd, Zn, Te, Se, and S. Bond energies of pure binaries and in the alloy are calculated. Trends are interpreted to show replacement of Cd by Zn stabilizing the alloy.

SIMS profiles of channeled implants of B, Al, and Na into (110) $Hg_{0.7}Cd_{0.3}Te$ are shown for several surface treatments on preimplant annealed and unannealed surfaces.

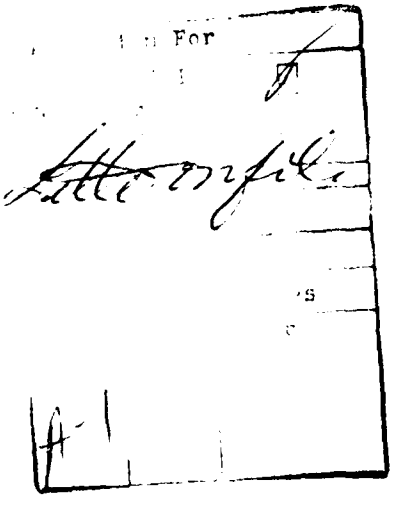

SUMMARY

Interface Study

- The choice of gate metal in MIS devices using Photox™ SiO_2 has been shown to alter layer resistivity and interface state density (N_{SS}). Ti/Au is the best performer of those tried.
- The contribution to flatband bias due to interface fixed charge in MIS devices has been determined. For a dessicated device the charge can be as low as -10^9 cm^{-2}; incorporation of H_2O increases the change by $+1 \times 10^{11}$ cm^{-2}.
- The relative amounts of SiOH, H_2O, and SiH have been found to be dependent on deposition rate. SiOH benefits interface mechanical integrity, while H_2O reversibly affects N_{SS} and Q_{fixed}.

Surface Study

- The initial stages of oxide formation on (110) HgCdTe have been studied to determine effects on electronic structure and resultant oxide. Oxygen uptake is enhanced by using oxygen excited by an ionization gauge in the line of sight to the sample. A complex Te oxide is formed which retains Cd but not Hg. The Cd content is enhanced at the oxide surface (10Å thick).
- The same characteristic of the Hg states which cause E_g to vary weakens Hg bonding. Resulting instabilities of the alloy and ease of defect formation are discussed as are their impact on surface and surface region properties.
- HgCdTe and CdTe are subject to considerable damage by ion milling (2 keV) but not by e^- beam (120 keV) during TEM.
- Preliminary experiments show that the introduction of large densities of dislocations by bulk plastic deformation does not affect the carrier type of p-type MCT grown by the CR process.
- Etch pits produced by the defect etchant 'Polisar etch 2' on the (111) A face of MCT grown by the Cr process are frequently associated with isolated Te precipitates. The proportion of pits associated with dislocations is much lower.
- The interfacial region between an HgCdTe layer grown by LPE and its CdTe substrate contains a high density of dislocations lying along (110) directions in a predominantly hexagonal network. Over a region less than 1000Å in thickness their mean spacing is consistent with accommodation of the lattice parameter mismatch between the two materials. The fact that this interfacial defect structure extends into the layer for several micrometers from the substrate creates a dilemma concerning the origin of this large number of dislocations, and leads us to the suggestion that fluctuations in composition may be responsible.
- The surface of HgCdTe cleaned at room temperature shows many steps which are associated with large densities of dislocations. Low-temperature cleaning should improve surface quality.

Alloy Bonding

Present best estimates of s, p and hybrid (sp^3) energies are presented for Hg, Cd, Zn, Te, Se, and S. These values still differ by 5% for Hg and Cd and ~10% for Zn. Bond energies of pure binaries are calculated, as are the change in these as the alloy is formed. Trends in these data indicate:

1. HgTe is destabilized by the presence of CdTe,
2. HgTe is slightly stabilized by ZnTe, and
3. the dislocation formation energy of ZnTe is significantly higher than in CdTe.

Expect HgZnTe to be more stable than HgCdTe.

Channeled Implant Task

Channeled ion implants have been done in (110) HgCdTe. SIMS profiles are presented for B^+ into wafers with different surface treatments and anneals. Also presented are a comparison of profiles for B, Al, and N_2.

SBRC

CONTENTS

Section		Page
	SUMMARY	iii
	INTRODUCTION	1
1	INTERFACE STUDY	3
2	SURFACE STUDY	37
3	ALLOY BONDING	137
4	CHANNELED IMPLANT	149

(This Page Intentionally Left Blank)

INTRODUCTION

This program is structured with SBRC as the prime contractor, with groups at Stanford University's engineering laboratory, SRI. International and Hughes Research Laboratory as subcontractors. Tasks are designed to take advantage of the unique capabilities of each, and which taken together will form a complete picture of the surface and defect physics of HgCdTe. As a result of the recently concluded MCT surface study program (DARPA Contract No. MDA 903-80-C-0496), it has become clear than the core issue underlying all aspects of the HgCdTe crystal growth and device fabrication, including surface effects, is the stability of the alloy against defect formation, particularly the ease of exciting Hg from its lattice site and its high mobility in the alloy.

Hg diffusion has been implicated in the surface type conversion (p to n) on cleaving of vacancy-dominated HgCdTe during photoemission measurements. Investigation of this effect has led to a detailed study of the bonding structure of the bulk alloy and to the discovery of the breakdown of the virtual crystal approximation. This breakdown is caused by the 10.5 eV greater binding energy of the Hg $6s^2$ valence states as opposed to the Cd $5s^2$ valence states.

A key result is the realization that the bulk and surface (or interfaces) of HgCdTe cannot be treated as "independent" entities as is the case (to the first approximation) with all other semiconductors studied to date. These results have given rise to new efforts in this contract, now underway, which include:

1. Quantitative theoretical studies of the HgCdTe bond energies and their relation to electronic and materials properties of the alloy, this done primarily at SRI; and
2. studies of "mechanical" properties, including TEM, plastic yield, and associated effects.

The study of the dynamics of oxidation is continuing at Stanford in conjunction with the development of surface treatments and passivation at SBRC. The devices produced at SBRC are being used as a probe, through DLTS and admittance spectroscopy, of Hg migration and defect formation in the surface region of processed HgCdTe. This ties all the other task results into practical device applications. We have already detected what is believed to be a dramatic decrease of the trap activity of the Hg vacancy near the device interface as a result of surface treatments. This work is extremely important and forms the central issue for SBRC's tasks. Finally the role of defects and Hg

vacancies in diode junction formation are being studied by a channeled implant task conducted at Hughes Research Laboratory. This effort is newly incorporated in the program.

The work outlined above has been reported in detail in the 2nd U.S. MCT workshop in Dallas in February 1983 and in all cases but one (Prof. Walter Harrison's invited paper on the theory of bonding in MCT) have been written up as full articles for the conference Proceedings with copies sent to DARPA.

This report presents results of the first six-month period of a three-year extension (to conclude in November 1985) of the studies begun under the original Surface Studies Program (DARPA Contract MDA 903-83-C-0108). The report is in four sections, each covering the work done by the four major groups. The results presented in each section, however, do represent whole program collaborations. These are titled: Interface Study, Surface Study, Alloy Bonding and Channeled Implants.

Section 1
INTERFACE STUDY

INTRODUCTION

The purpose of the interface study task of this program is to determine the electronic structure of HgCdTe at the interface with various insulators and oxides as incorporated in a passivated device. We examine in close detail the effects which are fundamental to the nature of HgCdTe and its defects.

We have seen as a result of the first two years of this study that surface treatments and material properties, especially defects, play a major role in final interface properties.[1] In the case of Photox™ SiO_2 on HgCdTe, the interface state structure which is controlled by the details of the bonding at the interface is very sharply affected by the presence of a Te-rich oxide.[2,3] This oxide grows on exposure to air of a surface which has a nonalloy composition as a result of certain surface treatments. These treatments are incorporated in a two-step surface preparation consisting of a polish followed by an etch. This was chosen because of its reliability and consistency in producing desirable C-V results. The interfaces produced are electrically similar to those produced with anodic oxide layers except that the surface state densities are generally lower, and the interface fixed charge is dramatically lower. Neither type of interface shows high concentrations of discrete surface states nor any indication of Fermi-level pinning. The bonding is essentially "oxide-like" for both interfaces. It was found, however, that for the Photox™ interfaces the Te-oxide reacts with adsorbed silane (SiH_4) during the Photox™ deposition, and it is the bonding of this resulting transition region with the HgCdTe that determines many of the final properties.[2]

The surface treatments used have been shown to selectively remove cations leaving a Te-rich surface. The details of the process determine the relative amounts of Cd or Hg removed. Processes which include mechanical action such as polishing tend to favor Hg removal. These processes also produce a strong alteration of the crystalline surface. Using electrolytic electroreflectance (EER) we have seen selective removal of the cation in amounts up to 4 atomic percent by use of certain etches.[4] This represents a concentration of vacancies well beyond those important for doping. We can expect this to have a strong effect on surface band structure. To first order the acceptor levels resulting from Hg vacancies can be expected to delocalize and broaden into the

valence band effectively narrowing the surface energy gap. It is more likely, however, that this high concentration of vacancies coupled with the mechanical energy of a polish results in a partial recrystallization of the surface layer to a higher x value, consistent with the lower amount of cations. This frees Te for oxidation and results in the wider E_g of a higher x-value alloy. The larger surface E_g acts as a barrier aiding in passivation. In addition to alterations of surface bandgap, many localized defects are likely to result such as Hg vacancies, Hg interstitials or antisite Te.

We have seen alterations of bulk electronic structure due to surface treatments extending to hundreds of Angstroms for nonstoichiometry[4] and to thousands of Angstroms for altered trap activity.[1] It is because of these types of effects that HgCdTe surface passivation cannot be treated as an isolated process ignoring effects on bulk properties.

It has become clear that in order to effectively passivate HgCdTe the entire interface region must be treated as a whole. The structure important for Photox™ MIS devices is shown schematically in Figure 1. This can be conceptualized as consisting of five regions. From right to left they are: the stoichiometric region of the bulk alloy; the nonstoichiometric or damaged region at the surface with a depth of hundreds to possibly thousands of angstroms; a transitional layer of reduced oxide between the HgCdTe and insulator; the applied Photox™ SiO_2 which also acts to seal the surface; and the metal overlayer which acts as a gate.

The electronic properties of these regions which are of particular importance for device passivation are listed in Table 1. These are being investigated with a combination of capacitance voltage (CV), deep level transient spectroscopy (DLTS) and low frequency admittance spectroscopy (LFAS) correlated to photoemission (PES) results obtained at Stanford. The CV technique allows measurement of the work function difference between the gate and substrate and insulator fixed charge as a flatband bias (V_{fb}). Separation of these contributions to V_{fb} constitute the bulk of the results presented in this section of the Interim Report.

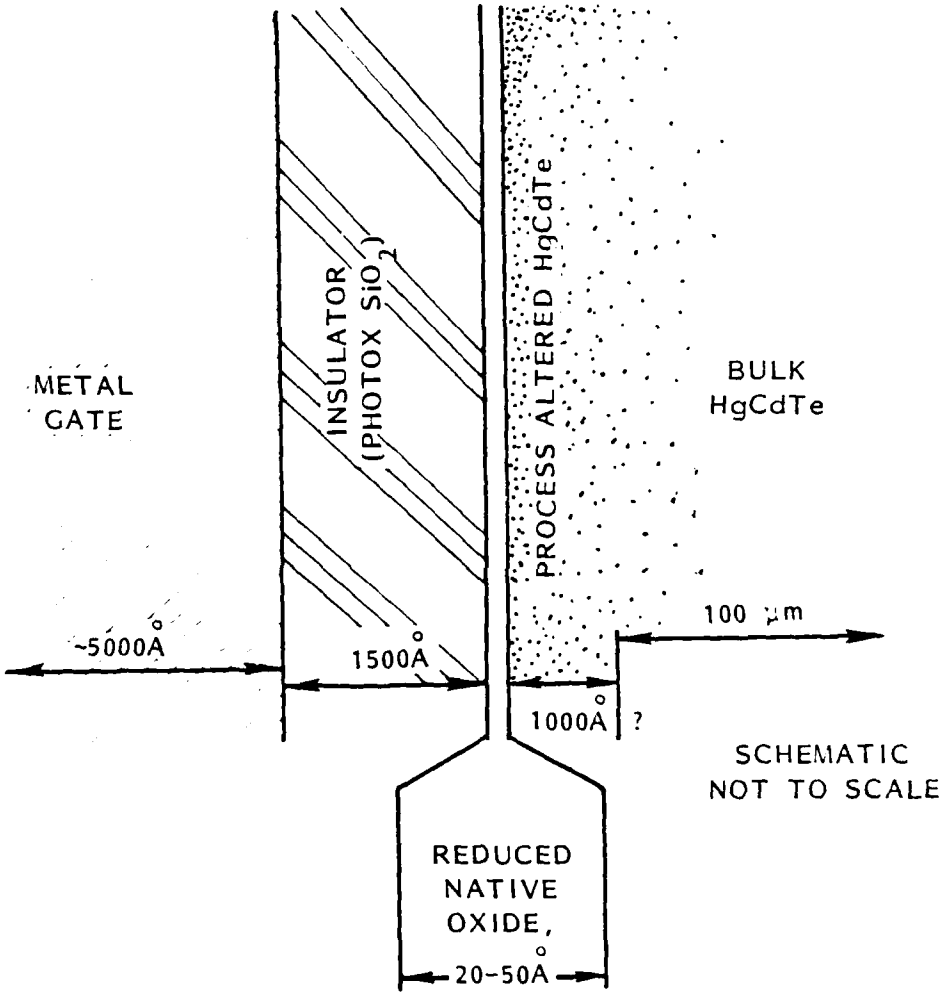

Figure 1. Schematic Representation of an MIS Structure on HgCdTe Showing the Regions Which Contribute to the Device Electrical Behavior. The Effect of Each Region is Outlined in Table 1.

Table 1

REGION	PARAMETER
Bulk HgCdTe	E_g, traps
Damaged HgCdTe	E_gs, band bending (ψ_s) Electron affinity (χ_s) Energy barriers (change of x or doping) Point defects, traps Localized states (amorphous region)
Native Oxide (Reduced)	Interface states (N_{SS}) Fixed charge (Q_f) Interface trap charge (Q_{it})
Insulator (Photox™)	Fixed charge (Q_f) Interface trap charge (Q_{it})
Metal Gate	Work function (W_m)

FLATBAND VOLTAGE

For eventual use as a passivation, the structures obtained thus far using deposited Photox™ are quite attractive. The material is chemically inert and produces very low flatband voltages (-0.4 to +0.2V). In these respects it eliminates the principal shortcomings of other common choices such as ZnS and anodic oxide. These latter are also easily attacked by reagents commonly used in device processing and in the case of ZnS is strongly altered by atmospheric water vapor. The actual interface state structure with SiO_2 is also seen to be altered by atmospheric water but this is completely reversible and with proper precaution is not a problem, as discussed in the appendix.

Eventual passivation of a PV device surface is a bit more complicated than producing good MIS interfaces, though an MIS capability is a necessary minimum condition. While detailed analytical study of the effects of various MIS properties on diode behavior is beyond the scope of this study program, some empirical results are available from developmental programs at SBRC and serve to illustrate the important parameters. These results indicate a strong dependence of device R_0A (zero bias resistance times junction area) and reverse bias current levels on the bias applied to a gate over the junction region.

Figure 2 shows results of R_0A plotted versus applied gate bias for a double layer LPE junction. The structure is an n^+ layer grown on a p-type substrate with a cutoff wavelength at 77K of 9 μm. Data as shown for two single element devices taken at 30K and 77K. The R_0A is highest for gate bias between about zero and -5 volt. In the region of zero bias R_0A drops abruptly by at least three orders of magnitude, for the 30K curve. For this diode to operate at peak performance requires a small negative gate bias.

With an n^+-on-p structure the depletion region is much greater on the p side. This also holds for the maximum width of a field-induced depletion region at the surface. The volume involved on the lightly doped p side under a positively charged gate is much larger than on the degenerately doped n side under a negatively charged gate. Hence, when the p side is depleted there is a larger volume from which to sweep minority carriers to the surface, causing a sharp reduction in lifetime. The effect of surface depletion is less important on the heavily doped side. For a diode with both p and n side more nearly equivalently doped the region of high R_0A will become quite narrow around flatband. This relationship has been discussed briefly by Grove and Fitzgerald[5] and plays the dominant role limiting R_0A.

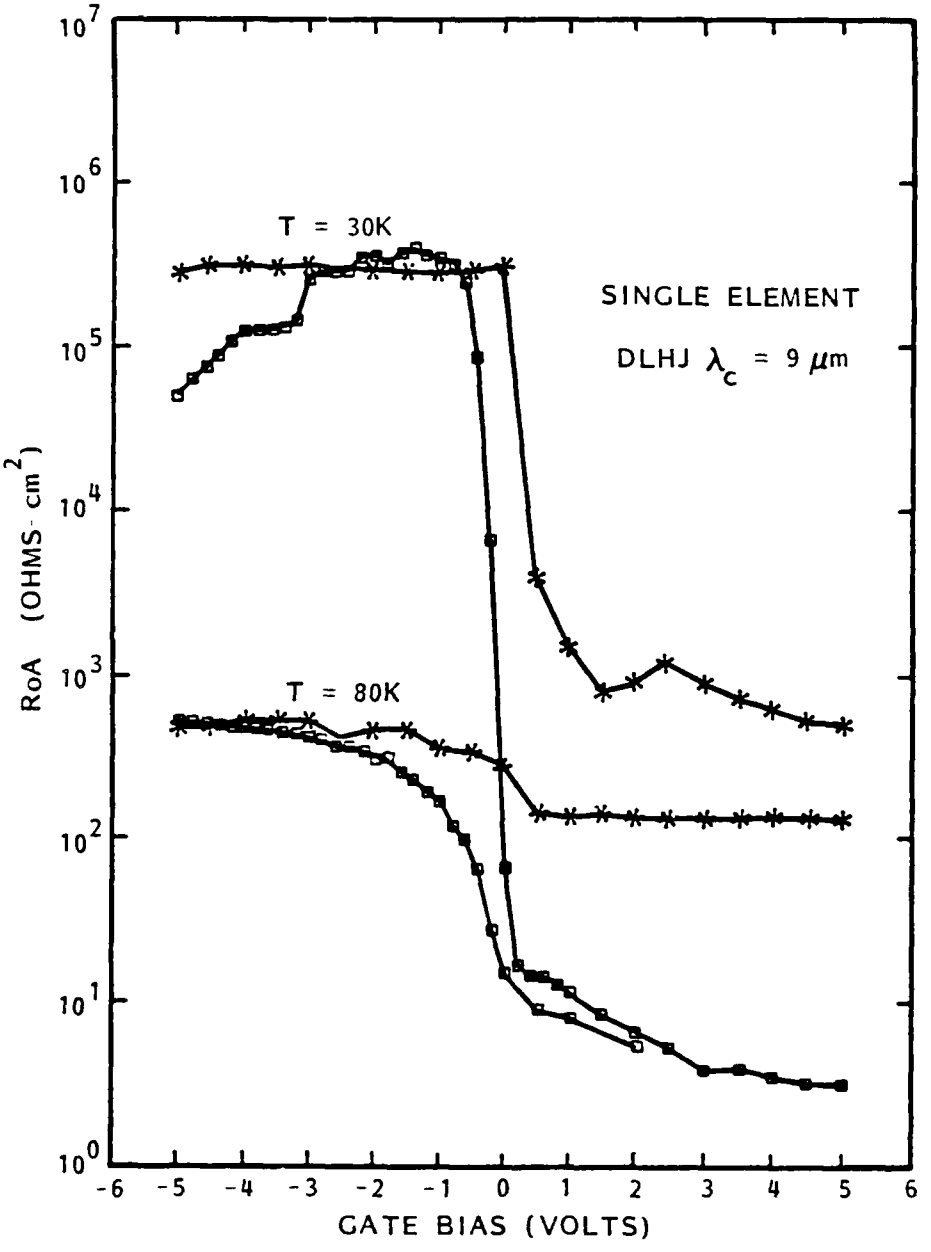

Figure 2. R_oA versus Applied Gate Bias for Single Element Double Layer Heterojunction Diode with λ_c = 9 µm at 77K

This type of behavior is quite general, having been seen in HgCdTe diodes operating at wavelengths from 2 μm to 10 μm, for diodes grown by double layer epitaxy. A different dependence has been seen with implanted junctions. Figure 3 shows IV curves for a MWIR device ($\lambda_c \approx 5$ μm) made by B^+ implant into LPE HgCdTe. This has nominally the same n^+-on-p structure. Here the R_0A is improved for positive gate biases as are the reverse bias characteristics. Reverse bias current should be as flat as possible to enhance uniformity when coupling multiple-element arrays to a CCD readout. The difference in behavior is believed due to the effects of gate bias on a strong trap tunneling current in the highly-doped region of the implanted diode. The MIS parameter of primary concern for passivation development is seen to be flatband bias. Once this is controlled for a given device, the surface state density and bulk trapping are expected to play a role in limiting minority carrier lifetime,[6] and possibly acting as a source of 1/f noise.[7]

Flatband bias seen in MIS devices occurs as a combination of work function difference between the metal gate and the semiconductor surface across the insulator, and charge in the region of the interface. In the case of insulators with V_{fb} of several volts or more, such as anodic oxide, insulator fixed charge dominates. This is most likely due to details of the bonding in the insulator or at the interface with the substrate. With Photox™ SiO_2, V_{fb} has been reduced to a level where fixed charge, charged interface traps, and work function difference are capable of making equal contributions. This is illustrated in Figure 4 which shows a comparison of high-frequency capacitance curves using different compositions of gate metal. The usual gate metal of thin Ti (400Å) overcoated with Au (4000Å) was applied to half of a wafer coated with Photox™ SiO_2, while on the other half a thin Cr layer replaced the Ti. It can readily be seen that the Cr gate shifts the curves to a more negative V_{fb} by about 0.7V, just the difference in work function between Cr and Ti.[8]

The displacement is clearly seen to be larger than the scatter in individual V_{fb}s for each gate. The scatter seen in Figure 4 is typical of devices made over the surface of an average wafer. No dependence of V_{fb} on the position of the actual device on the surface has been seen. The source of this nonuniformity remains to be determined.

The insulator capacitance (C_{ins}) as measured in strong accumulation is seen to vary by up to 10 pF about the average. The principal cause of this is

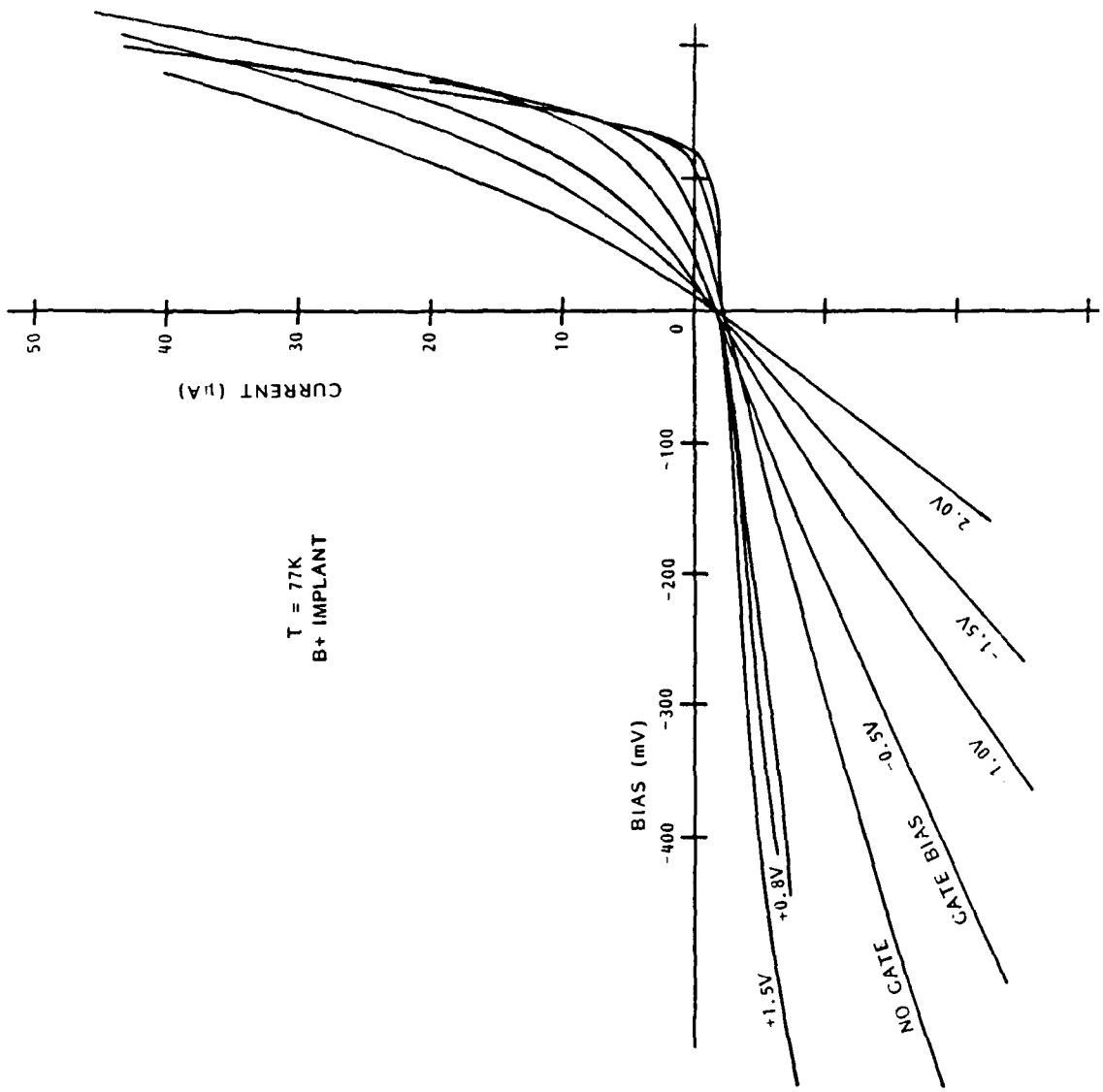

Figure 3. Dependence of the Current Voltage Relationship of a B^+ Implant Junction in HgCdTe on Gate Bias

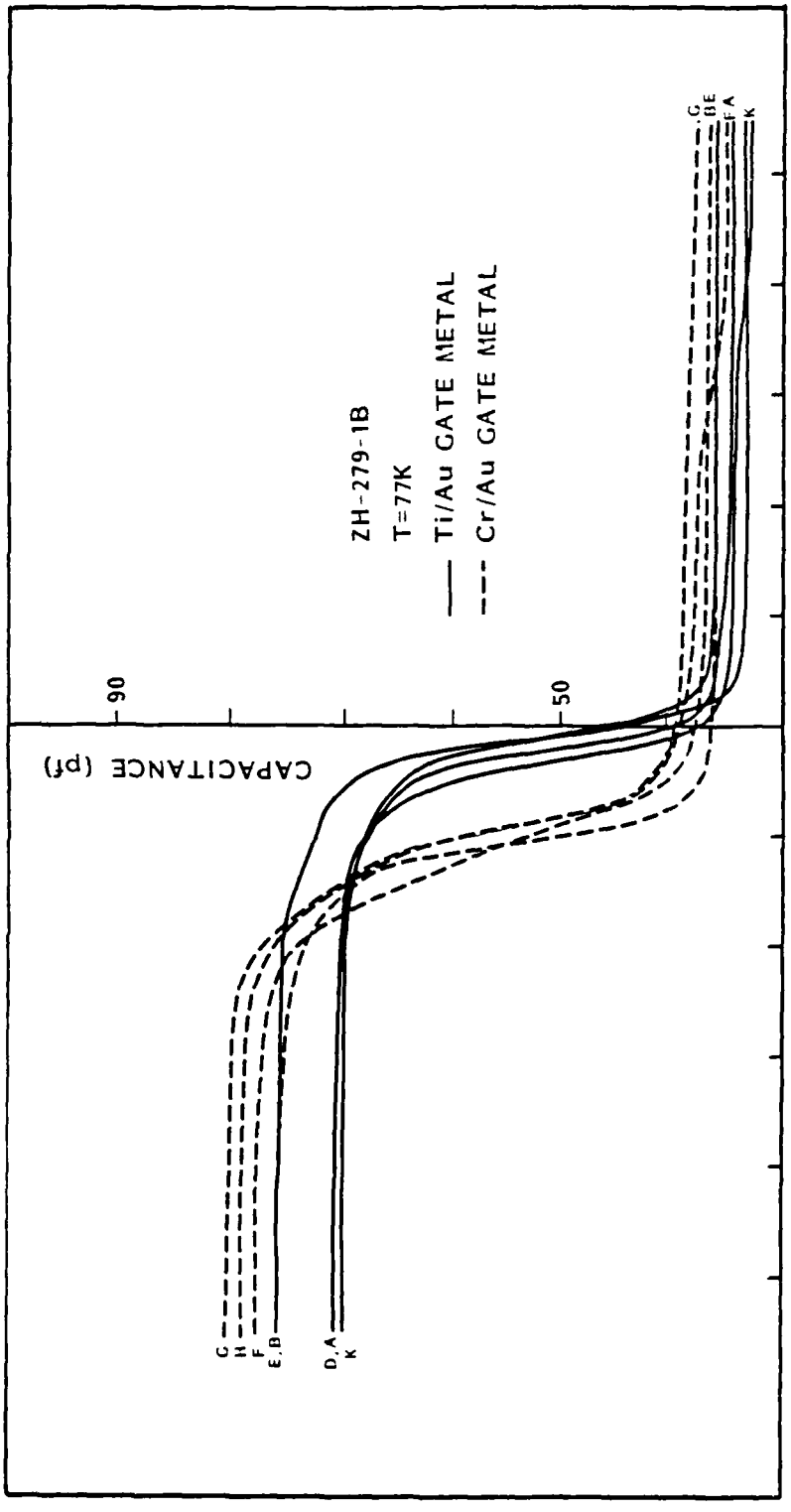

Figure 4. Effect of Gate Metal Work Function Charge on C-V Characteristics of MIS Device Using 1500Å Photox™ SiO_2

variation in area of the shadow masks used to simultaneously produce large numbers of devices. This variation increases with mask use. This set of data is displayed "as taken" without correction for variation in area. To determine SiO_2 dielectric constant, for example, the actual area of each device is optically determined.

During this reporting period we have completed the first of a series of experiments designed to separate the relative contributions to V_{fb} of the materials' work functions from that of net interface charge. The technique is in principle very straightforward and is to measure the flatband bias as a function of insulator thickness. The contributions due to fixed charge (Q_f) and interface trap charge (Q_{it}) will vary with thickness while work function difference (W_{ms}) will not, as shown in Equation (1).

$$V_{fb} = - \frac{Q_f + Q_{it}}{C_{ins}} + W_{ms} \qquad (1)$$

where C_{ins} is inversely proportional to insulator thickness. The contribution due to trap charge can be determined from the distortion of the quasi-static capacitance curve.

The most straightforward way to do this is to take an MIS device, characterize it, then etch away insulator, deposit a new gate, remeasure, and so on. The yield of this technique on HgCdTe would be close to zero due to the mechanical fragility of the interface. Additionally, due to the porosity inherent in the low-temperature CVD SiO_2, it would be impossible to guarantee the interface charge had not been altered by the chemicals used. Hence, two higher yield alternate techniques were used. The first was to deposit SiO_2 in successive steps, masking portions of the substrate to achieve several thicknesses side by side on the same substrate. The second was to cut the substrate into four or five sections and deposit a different thickness insulator on each in successive depositions. Both these techniques depend on production of equivalent interfaces under several separate gates. This depends heavily on good uniformity of the wafer properties, treatments, and depositions. A very good indication of the equivalency of devices is from the equivalency of the form of the high and low frequency C-V curves so that appropriate sets of samples may be selected. Parts made by both techniques have been measured and show two types of interfaces with different amounts of fixed charge.

Several wafers representing the last parts of an ingot which had produced legendary photoconductors and MIS devices (ZH-270) were exposed to the stepped deposition technique. The insulator was deposited in four steps to produce nominal thicknesses of 500, 1000, 2000, and 4000Å. Our standard Ti/Au gate metal was deposited to make a MIS device. As can be seen in Figure 5, the variation in V_{fb}, as indicated by these 1 MHz curves, is very low. These wafers were then diced to isolate each thickness and bonded into TO-8 headers. This allows us to record quasi-static capacitance measurements. Our quasi-static measurements are made from about +5.0 to -5.0V with a sweep rate of 50 to 100 mV/sec or about 10^{-2} Hz. These particular samples, though showing very good C-V curves (both high and low frequency), did not show any measurable storage times so that this scan rate is a good approximation to actual quasi-static conditions. We used Berglund integration to obtain surface potential from applied gate bias as shown in Equation (2).

$$\psi_s = \psi_{so} + \int_{V_{GO}}^{V_G} dV_G \left[1 - \frac{C_{LF}(V_G)}{C_{ins}}\right] \tag{2}$$

where C_{ins} is insulator capacitance, V_G is applied gate bias, ψ_s is surface potential (ψ_{so} is fixed in strong accumulation by V_{GO}) and $C_{LF}(V_G)$ is low frequency capacitance measured at V_G. In turn, C_{LF} consists of insulator capacitance, surface charge capacitance (C_s) and interface trap capacitance (C_{iT}) as shown in Equation (3).

$$C_{LF} = \frac{1}{C_{ox}} + \frac{1}{C_s + C_{iT}}. \tag{3}$$

Figure 6 shows a plot of ψ_s versus V_G obtained for one such measurement compared to a curve generated for this device in the absence of interface traps. These curves are used to determine the applied bias at which flatband occurs. In Figure 7, the values of V_{fb} obtained are plotted versus the actual SiO_2 thickness as measured by monochromatic (λ = 6320Å) ellipsometry. Net insulator fixed charge is obtained from the slope of the line fit to these points, while the intercept is determined by the electrochemical potential differences between the gate metal and the HgCdTe surface.

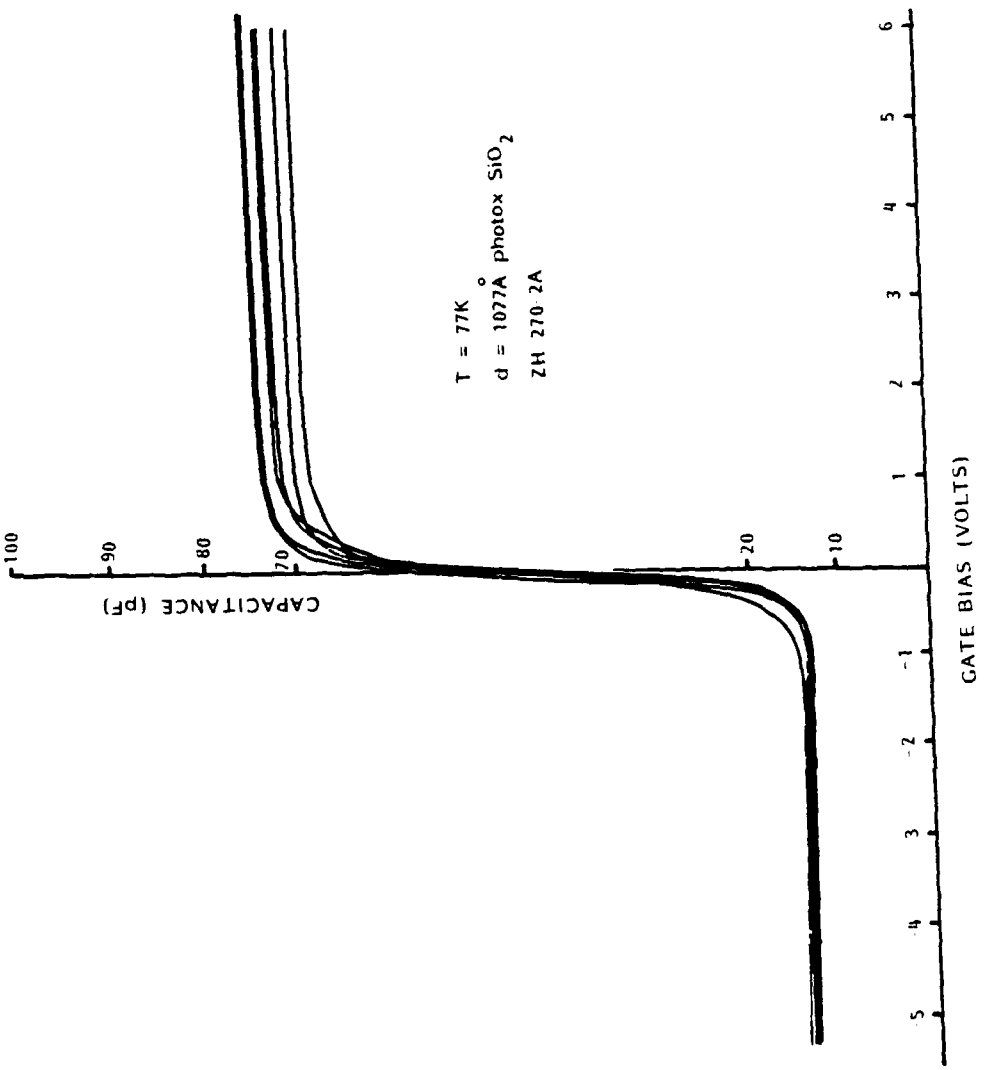

Figure 5. High Frequency (1 MHz) C-V Characteristics Showing Uniformity of Devices Used to Separate Q_{fixed} from W_{ms}

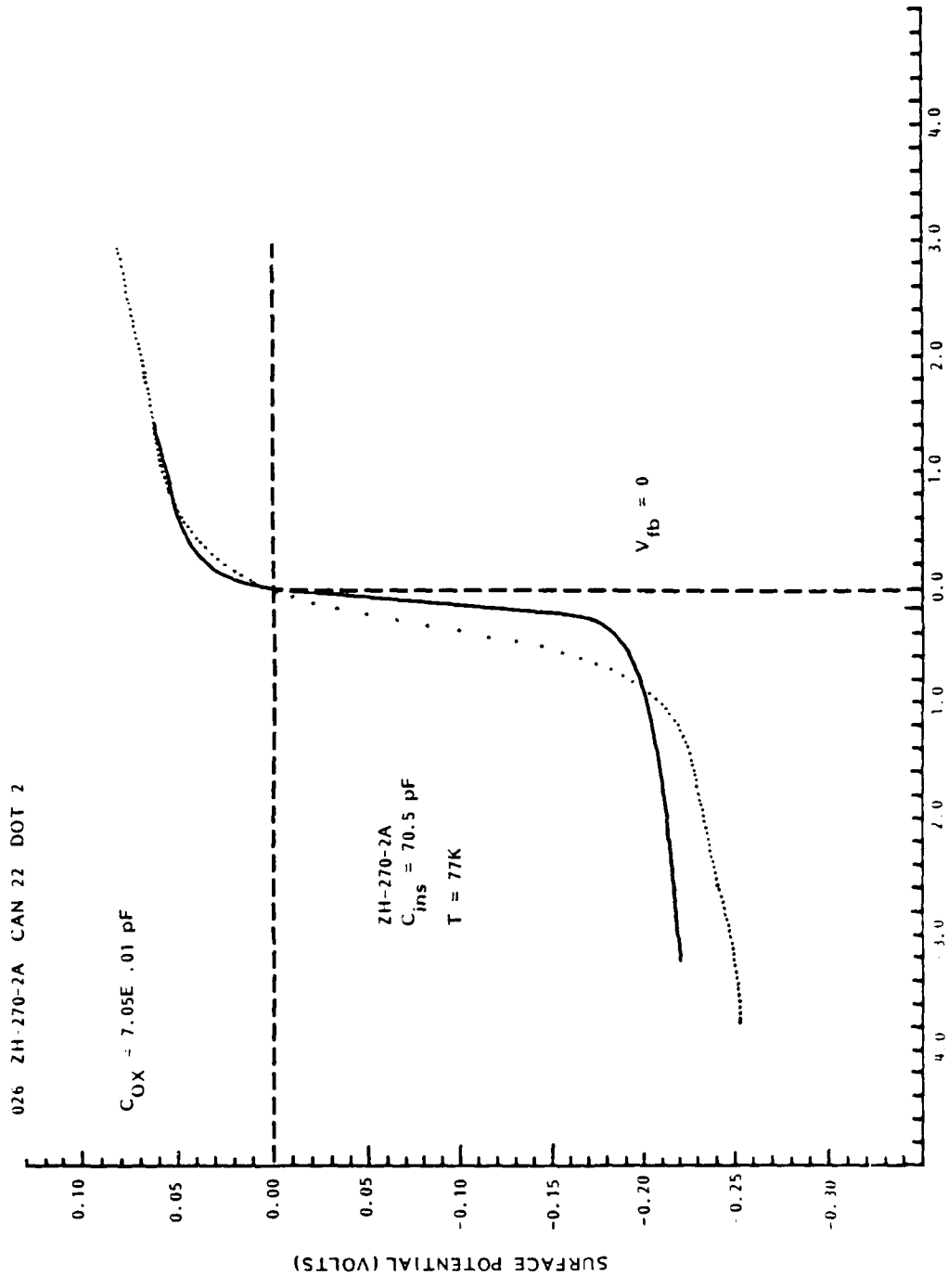

Figure 6. Dependence of Surface Potential on Gate Bias Obtained From Berglund Integration

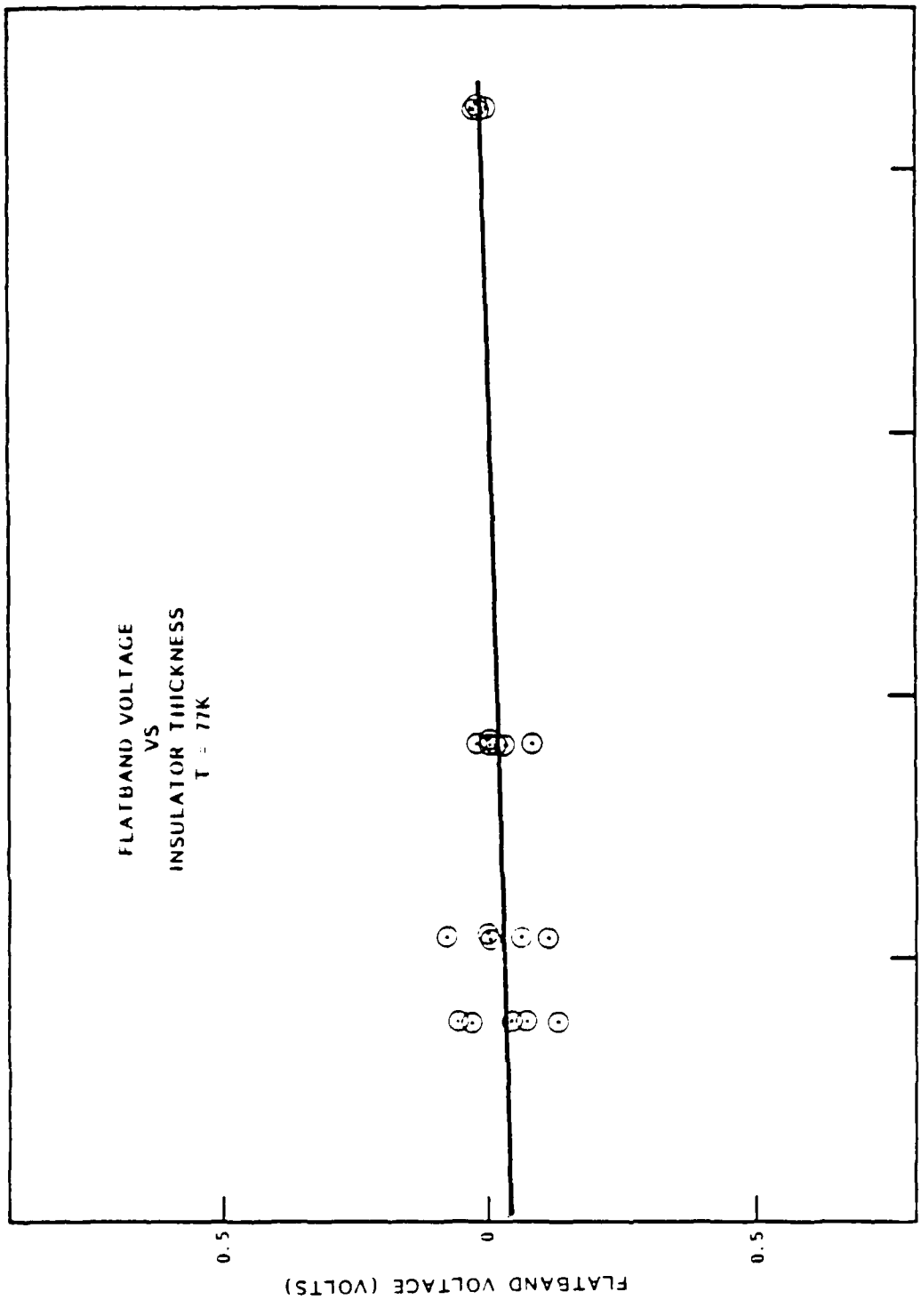

Figure 7. Flatband Bias versus Insulator (Photox™) Thickness

The net fixed charge for this interface is $-3.5 \pm 0.5 \times 10^9$ cm^{-2}. This is a surprising number both in how small it is, on the order of the surface component of the doping density, and its sign. Previous MIS devices using only a single layer of Photox™ (these samples used up to four stacked layers) show negative flatband biases of up to 0.5 volt at thicknesses of 1500Å. This obviously implies a larger and positive fixed charge. Preliminary data on one other set of multilayer and three sets of single layer stepped insulator samples confirm a difference in fixed charge depending on the method of deposition.

These multiplayer samples were prepared by depositing sequential steps of roughly 500 to 1000Å, the first covering the entire substrate and defining the common interface. Subsequent layers were made with increased masking of the sample. Before each Photox™ deposition the reaction chamber is evacuated to $\sim 1 \times 10^{-6}$ Torr for two ten-minute periods with a nitrogen purge between. The sample is at 100°C during this process. Thus all the layers of the multilayer samples except the top farthest from the interface have received a 20-minute vacuum bake. Single layer MIS devices do not. As discussed in the appendix, it is possible to remove enough water from Photox™ by vacuum baking to alter the net fixed charge. This strongly suggests that details of the manner of deposition and insulator formation can have a significant effect on insulator charge.

The intercept in Figure 7 represents the electrochemical potential difference across the device. In principle we could determine the electron affinity of HgCdTe from this work function difference and the work function of the Ti gate layer, provided we knew the bandgap of the surface region along with the Fermi energy. There is considerable evidence that surface treatments alter the composition by selectively removing one or the other cation, leaving a nonalloy composition. The types of surface treatments which have strong effects on the surface composition are etches, polishes,[4,9] and anodization.[10,11] Even cleaving has been shown to produce effects in the form of conversion to n type. It may be possible that different wafers will also respond to different degrees to the same treatments depending on the presence of defects, precipitates, or impurities, and therefore represent different distortions of nominally the same substrate. As a result, these surface regions can have vacancies in concentrations amounting to several atomic percent, so that it is essentially a fourth constituent.

Thus the surface region is likely to have a significantly different bandgap from the bulk, and can be viewed as a heterojunction. To the extent the common anion rule is applicable, it will show bandgap differences principally in the form of a conduction band offset. This virtually guarantees a nonbulk value for the electron affinity of the surface region.

Similar experiments to determine the distribution of fixed charge in an anodic oxide layer have not turned out as well. As in the case of SiO_2, the anodic oxide is not amenable to sequential etch and device fabrication. However, in this case it is more difficult to fall back on making equivalent devices side by side with different thicknesses. The process of growing the oxide is itself a surface treatment, with the resulting interface moving deeper into the wafer and tending to concentrate dopants left over after the matrix is oxidized. This can change the surface Fermi energy, causing a nonlinear dependence of V_{fb} on thickness.

EFFECT OF GATE METAL AND WATER ON DEPOSITED SiO_2

The effects of gate metal composition on the resistivity and capacitance of the SiO_2 layer were also investigated in a series of similar samples. Various zone melt wafers (measuring approximately 1.0 × 0.5 inch) were coated with 1500Å of Photox™. MIS devices were made by deposition, through shadow masks, of different gate metals. Results of measurements of SiO_2 resistivity at room temperature are shown in Figure 8. The line connecting sets of points indicates these two were made on the same substrate (identified). From this data no fluctuations can be attributed to the substrate. All the changes can be attributed to gate composition or thickness. Composition of the gate used is shown along the horizontal axis. Where two metals are indicated, the gate is a bi-layer where the first one listed is the one in contact with the insulator. The Ti/Au contact is our nominal standard for this study. The thick Au is to aid bonding and probing while a thin Ti layer prevents Au from diffusing into the insulator and aids adhesion. These are deposited, as mentioned before, to thicknesses of 400 and 4000Å.

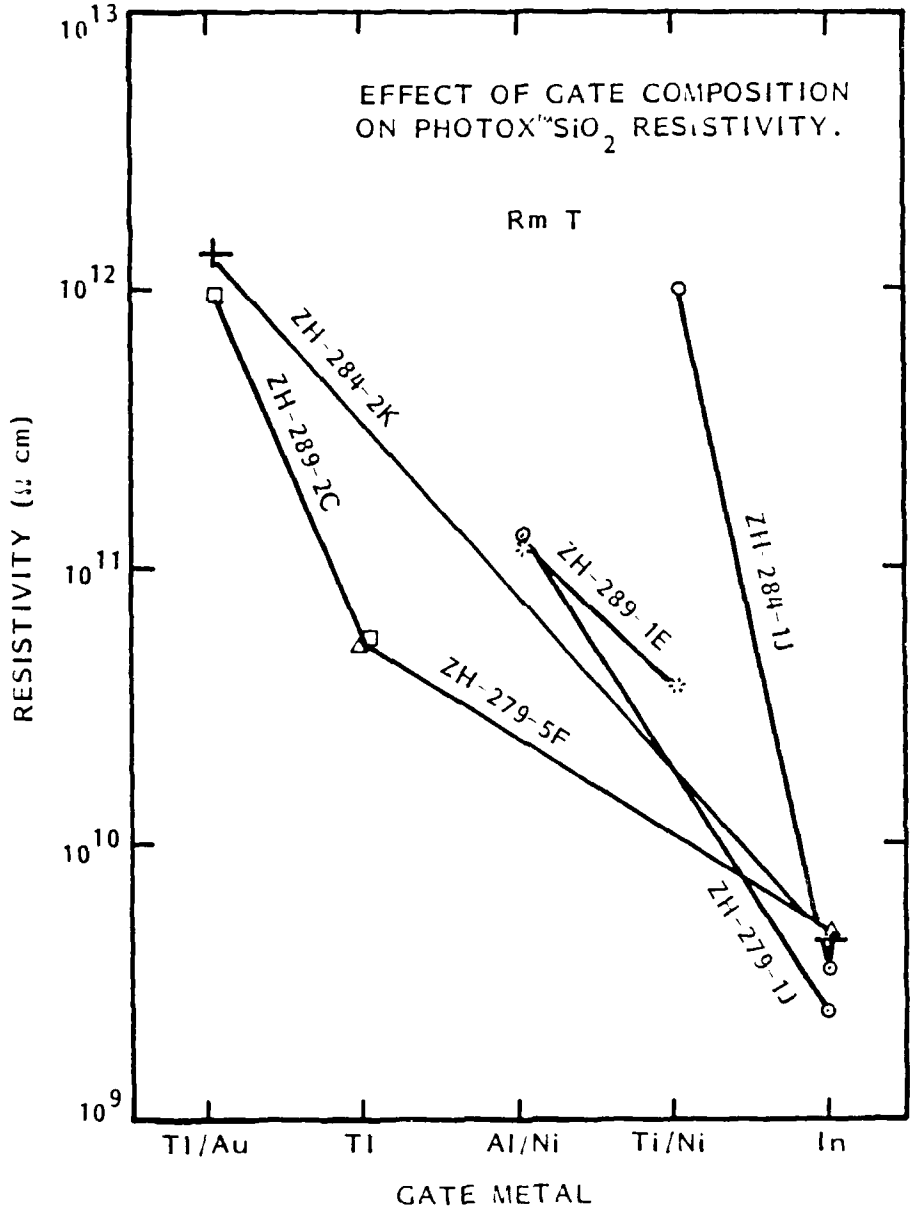

Figure 8. The Effect of Gate Metal Type on dc Resistivity of 1500Å of Photox™ SiO_2

The Ti-only gate was deposited to a thickness of 4000Å, and we note that the resistivity is down by over an order of magnitude. Apparently the larger mass of the thicker layer represents a large enough energy transferred to the SiO_2 surface to enhance diffusion of Ti into the natural porosity of the SiO_2. The Ti layers used with the Ni were deposited on the thinner side and show resistivities between the extremes established by the Ti/Au and Ti-only values. In the case of a single In layer resistivities are down by over two orders of magnitude from Ti/Au. This would be a poor choice for a gate metal on Photox™ SiO_2.

The obvious mechanism for lowering resistivity is diffusion into the natural porosity of the SiO_2 layer. As discussed in the appendix to this section, we can also see effects due to processing chemicals including water. The view that these gate metals can diffuse into the SiO_2 is supported by the observation that C_{ins} interface state structures are also altered by the specific gate metal. Generally, those with the strongest effect on resistivity also show the strongest effect on capacitance.

This is illustrated in Figure 9, which shows high-frequency (1 MHz) capacitance curves for MIS devices made with Ti/Ni and In on opposite ends of the same wafer. This is one of the samples shown in Figure 8. Note that two capacitance scales are shown, one for each gate metal. The value of C_{ins}, as measured in strong accumulation, is essentially that expected for 1500Å of Photox™ SiO_2 (~60 pF) only for the Ti/Ni gate. The In gate C_{ins} has dropped to nearly half that. This lowers the insulator effective dielectric constant to 2.5 $\times 10^{-13}$, 60% of that of clean Photox™. We can also readily see an increased hysteresis and lower slope through depletion which indicates increased density in traps at the interface and in the region of the SiO_2 near the interface.

Water incorporated in the layer during deposition as well as absorbed from the atmosphere after deposition can have similar though much less severe effects. These are discussed in detail in the following reprint.

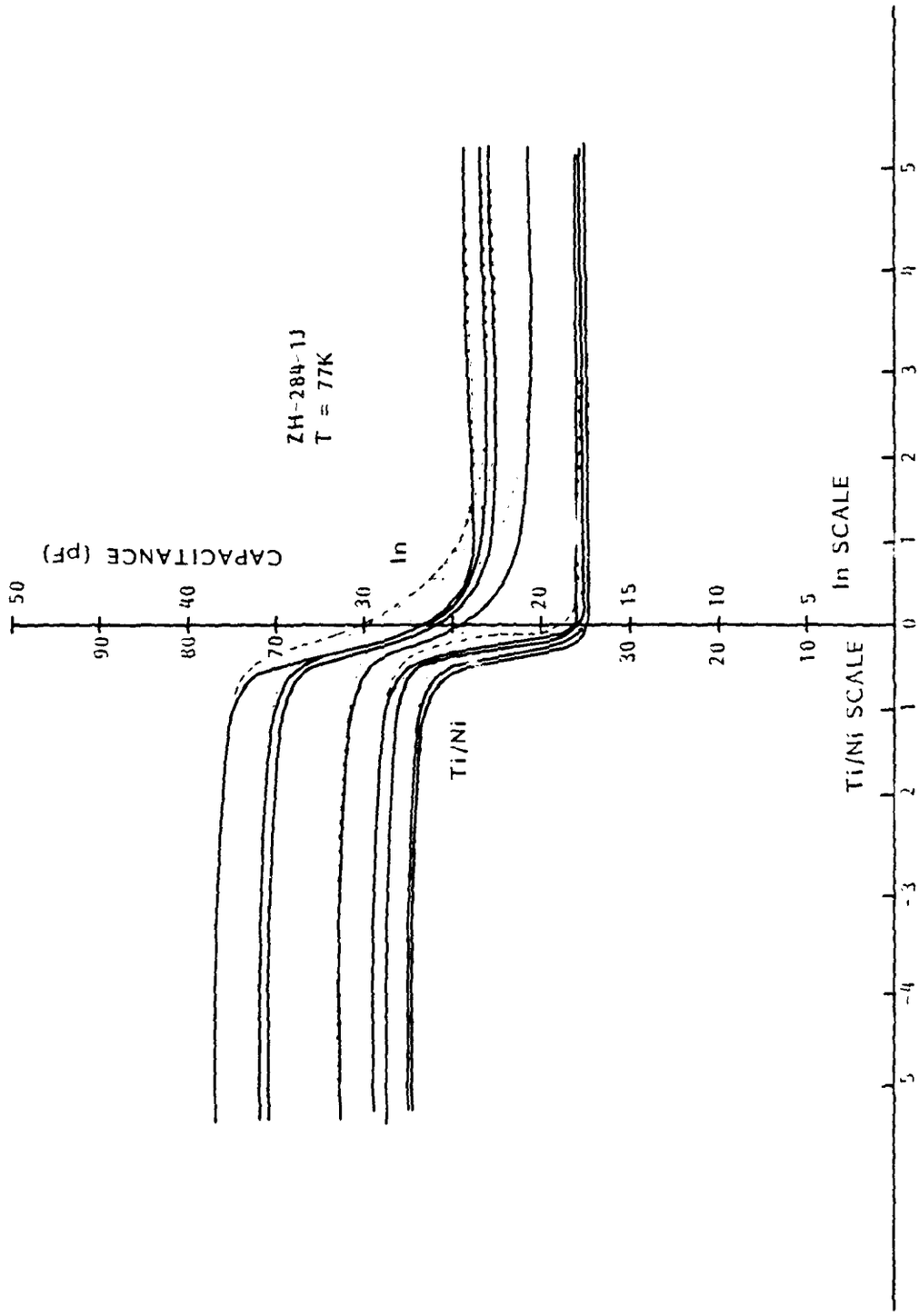

Figure 9. The Effect of Gate Metal Composition on Interface Electrical Properties Illustrated for Ti/Ni Versus In

SBRC

Effects of H_2O on the SiO_2-HgCdTe Interface

J.A. Wilson and V.A. Cotton
Santa Barbara Research Center
Goleta, CA 93117

ABSTRACT

The effects of water on the electrical and mechanical properties of the Photox™-HgCdTe interface were investigated using capacitance voltage techniques (1 MHz and quasi-static) and a simple scratch test, in conjunction with Fourier spectroscopy to monitor actual water content. The water which is available as a by-product of the deposition reaction becomes incorporated in the layer, with the amounts depending on deposition rate, as SiOH, H_2O and SiH•••O. The relative amounts are also dependent on deposition rate; SiH increases with rate while SiOH and H_2O decrease. After long periods (1 year) of atmospheric exposure, the SiH concentration goes to zero. In fact, layers deposited at higher rates in some ways come to spectrally resemble the lower deposition rate layers. The increased SiOH concentrations of the lower deposition rate layers result in better mechanical integrity of the interface. These rate-dependent concentrations do not affect interface electrical properties. However, it was seen that water absorbed after the layer was deposited strongly affected electronic structure, increasing interface state density between the valence band and midgap and increasing the insulator fixed charge by about $+1 \times 10^{11}$ cm^{-2}. These effects are reversible, with the initial interface structure recovered after a low-temperature vacuum bake.

INTRODUCTION

Among the materials finding use as a passivation for HgCdTe and other common infrared detector materials, one of the most promising is low-temperature chemical vapor deposited SiO_2 [1,2,3], in a version patented by Hughes Aircraft Company (Patent No. 4,371,587) called Photox™ [4]. In general, these types of SiO_2 have several distinct differences from SiO_2 grown on Si. These stem principally from the temperature tolerance of the substrate. SiO_2 grown on Si is inherently a high-temperature process which frequently incorporates an anneal in excess of 900°C [5]. For most IR detector materials these high-temperature steps are not tolerable. In the case of HgCdTe, even brief exposure to temperatures much in excess of 100°C are seen to alter device performance. The low-temperature CVD processes offer an attractive alternative. The SiO_2 itself is chemically inert, in contrast to native oxides of many of the IR materials including HgCdTe, and possesses a much higher resistivity [6]. The effects of water (H_2O, OH and H compounds) on these films and interfaces is an important consideration for two reasons: it can be absorbed from the atmosphere and retained in the porosity; also, it is available during deposition as a by-product of the deposition reaction [7].

We report here the results of an investigation of the role played by water in the interface properties of Photox™ on HgCdTe. The amount of water present has been monitored using IR transmission spectroscopy on layers deposited under different conditions and also after exposure to atmospheric water. Measurements of interface electrical results are made on MIS devices using high-frequency (1 MHz) and quasi-static capacitance voltage techniques. An indication of the mechanical integrity of the interface was obtained by scratch testing followed by exposing the interface to an acid etch which weakens the bonding to the substrate, causing separation in response to interface stress. We have found that water can play two roles: incorporated into the structure of the SiO_2 Ar SiOH during deposition, it affects the mechanical stability of the interface; absorbed into the natural porosity of the layer after deposition Ar H_2O, it reversibly affects interface electrical properties. These two cases show separate spectral behavior as measured by absorption spectroscopy.

SAMPLE PREPARATION AND MEASUREMENT

Capacitance measurements were performed on MIS devices made with 1500Å of Photox™ on $Hg_{1-x}Cd_xTe$ ($x \approx 0.30$) wafers prepared by a two-step process. This

process consists of a Br_2 in dimethylformamide polish plus a Br_2 in ethylene glycol etch [8]. The HgCdTe was grown by the horizontal zone melt technique, with the material cut into wafers parallel to the long axis of the boule. This results in wafers of random orientation. It is also very frequently polycrystalline. We have seen no systematic change of results attributable to any particular grain orientation. Wafers are annealed isothermally in Hg vapor to lower the acceptor level (due to cation vacancies produced at the high growth temperature) below that of the donor level due to background impurities. These are typically in the range 1 to 5×10^{14} cm^{-3}. Midwavelength material ($x \approx 0.30$) was used to avoid interpreting C-V curves complicated by tunneling effects seen in very narrow bandgap materials.

The metal gate is made by depositing 400Å of Ti followed by 4000Å of Au. Both layers are deposited by e-beam evaporation through a shadow mask. The gate area is 2.04×10^{-3} cm^2, resulting in MIS devices with insulator capacitance of about 60 pF.

Capacitance measurements are made at 1 MHz using a PAR 410 capacitance meter and at quasi-static using an electrometer (ramp rate is ~10 mV/sec). Typical current levels are 10^{-11}A. Measurements are made in a dewar cooled with LN_2 and with zero field of view.

The amount and form of H_2O retained in the SiO_2 was measured by IR absorption spectroscopy using a Nicolet Model 7000 Fourier spectrometer operating at room temperature. Measurements were done in an atmosphere of dry nitrogen to remove atmospheric water from the light path. Samples were prepared by deposition of Photox™ at a temperature of 100°C (which is an effective upper limit for use with HgCdTe) on Irtran II to a thickness of 1 μm in order to provide sufficient absorption to see the features of interest. These are due to H_2O, SiOH and SiH at wavenumbers of 3330, 3650 [9] and 2280 cm^{-1} [10]. Deposition rates from 20Å/min to 85Å/min were used and effectively varied the amount of "incorporated" water.

The mechanical strength of the interface was tested by exposing the interface region to nitric acid which dissolves the oxide layer bonding the SiO_2 to the HgCdTe. Depending on the amount of stress in the layer, it can lift off locally or involve regions beyond the area directly affected by the etch, even to catastrophic failure of the entire layer. The interface was exposed by scratching through the SiO_2 with a carbide tip. Layers used for these tests were 1500Å thick on HgCdTe. The HgCdTe surface was prepared as for MIS fabrication.

The capacitance measurements, spectroscopy and scratch tests were made on layers produced under nominally identical conditions. Measurements were made immediately after fabrication (6 to 24 hours), after exposure to ambient atmosphere or water vapor for periods of several days (in one case one year) and after vacuum baking (60°C) for periods of several days.

RESULTS

As shown in Figure 1, we found the deposition rate to be a monotonically increasing function of chamber pressure in agreement with the results obtained for thermal CVD SiO_2 by Maeda and Nakamura [11]. In that work the reaction rate dependence on pressure was explained in terms of a true surface reaction to produce the SiO_2 layer; i.e., SiH_4 and O are adsorbed and then react to produce SiO_2 plus by-products. We believe the Photox™ reaction to also be a surface reaction which proceeds along similar lines. This is principally by observation that SiO_2 is 'deposited' on vertical and hidden surfaces in amounts difficult to explain by a gravity directed precipitation. The leveling off of deposition rates for 1 μm thick layers between 1.0 and 1.2 Torr in Figure 1 (short dashed line) was seen to correspond to a buildup of deposited SiO_2 on the underside of the quartz window during the very long run. This blocks the UV and slows the deposition rate.

Also shown in Figure 1 is the index of refraction. For the thinner (nominally 1500Å) layers the index increases smoothly with pressure as expected. The refractive index for the thicker layers, used for transmission spectroscopy, are seen not to fit the same curve as the thinner ones. As pressure increases, the index rises, then drops sharply between 0.6 and 0.8 Torr, then resumes an upward trend. This may represent an alteration in layer structure at a critical thickness for a given deposition rate due to a deposition rate dependent buildup of internal stress. The critical thickness is exceeded for 1 μm layers deposited above 0.6 Torr. This would indicate that internal stress is deposition rate dependent, increasing for higher rates. The fluctuation is less likely to result from an unmonitored change of deposition conditions due to, for example, the blockage of UV as mentioned above, except in the case of pressures above 1 Torr.

Another important consideration to understand the nature of the SiO_2 studied here is the Si:O ratio. Samples prepared at 0.6 and 0.9 Torr were measured using Rutherford backscattering. The derived ratios were 1:2.27 ± 0.03 and 1:2:37 ± 0.03 [12]. Extrapolating this trend over the range of pressures studied here (0.4 to 1.2 Torr) indicates all layers are oxygen-rich as compared to SiO_2. A small concentration of Hg was seen at the detection limit estimated at 10^{-3}. The Hg is undoubtedly incorporated during growth from the Hg vapor used to catalyze the $N_2O \rightarrow O$ step.

The spectral characteristics of Photox™ SiO_2 are typical of low temperature CVD SiO_2 in general [13]. We see SiO stretch and bend modes at 1065 and 810 cm^{-1}, as shown in Figure 2. Also present are bands due to hydrogen bonded hydrogenated oxide SiH•••O at 2280 as well as SiH modes at 875 and 650 cm^{-1}. Structure due to OH bonding is seen at 3650 and 3330 cm^{-1} representing SiOH and H_2O. These OH structures are common to low temperature CVD SiO_2 [10]. The curving background of these spectra is due to interference in the 1 μm thick layers. Spectral examination of the 1 mm thick Irtran II substrate showed the transmittance to be flat at about 80 percent out to 650 cm^{-1} as expected. A comparison of spectra of layers grown at different deposition rates shows that the strength of the SiOH, H_2O and SiH•••O structures can be strongly affected. This is illustrated in Table 1 where the area under each structure was measured and normalized to a standard 1 μm thickness. The entries represent concentration changes relative to the layer deposited at the lowest rate (0.4 Torr). The strength of the SiH•••O feature is seen to be strongly proportional to the deposition rate, while that of H_2O and SiOH is inversely proportional. For thick layers deposited above 1 Torr, all three abundances depart from the trends shown by the lower pressure layers. We note that this is the region where the deposition rate was strongly lowered by opaquing the UV source. Thus it appears in general that the amount of OH type bonding relative to SiH is adjustable through the deposition rate.

Table 1. Relative H_2O, SiOH and SiH Concentration versus Pressure (Normalized to 0.4 Torr)

PRESSURE	H_2O	SiOH	SiH
0.4	1	1	1
0.6	0.89	0.91	1.3
0.8	0.76	0.64	2.1
1.0	0.38	0.46	3.2
1.2	0.47	0.35	3.3

Spectra taken of a layer deposited at 70Å/min (0.9 torr) and exposed to atmosphere for one year showed alteration of some of these features as shown in Figure 2. The SiOH band was essentially unchanged; however, the SiH features at 2280 and 875 cm^{-1} have disappeared, while the H_2O has increased in amplitude. This represents a slow alteration of the SiH to SiO_2 and incorporated H_2O. Vacuum baking of these layers (60°C for 5 days) has had no discernible effect on any of these features. Thus we see that layers deposited at the higher deposition rates and showing larger SiH•••O features change their internal structure after prolonged atmospheric storage to resemble the water-rich and SiH-poor layers deposited at the lower rates.

The water incorporated in the film during deposition is that produced by the reaction itself. The deposition is a surface reaction with SiH_4 and O(3p) being adsorbed before reacting to produce SiO_2 with a possible intermediate step being the production of disilyle ether $(H_3Si)_2O$ (liberating gaseous H_2) which then breaks down to SiO_2 plus various OH groups including H_2O [11]. The complete reaction in the case of Photox™ depends on Hg and UV (2537Å) to produce atomic oxygen from N_2O. The amount of residual atmospheric water vapor in the reaction chamber is estimated at less than 1×10^{-6} Torr and is thus not a candidate source. This low residual pressure is a result of pumping the reaction chamber to 1×10^{-6} Torr and baking at 100°C for two 10-minute periods with a dry nitrogen flush between, prior to depositing SiO_2.

The effects of exposing freshly deposited layers to water vapor is shown in Figure 3. This shows spectra of the same layer as deposited after exposure to water vapor (90% humidity, 32°C for 24 hours) and after a vacuum bake (60°C for 44 hours). The H_2O band area strongly increases after exposure by 30%. Baking reduces this to within 6% of the as deposited amount. Also we see the SiH feature decreases after water exposure but is not recovered after baking. The SiOH band is essentially unaltered by exposure to water or baking.

It is clear from these results that there are two mechanisms of water retention in Photox™ SiO_2. These are distinguished by the response of the H_2O and SiOH bands to vacuum baking. In the case of H_2O which is removable, the likely mechanism is retention on the inner surfaces of the natural porosity of the layer. The amount of SiOH is not altered by baking and is incorporated in the bonding structure of the layer itself.

The effect of these species on the interface electrical structure has been studied by monitoring changes in capacitance characteristics. Measurement of layers deposited at different deposition rates, and showing different SiOH concentrations, showed no discernible variation in electrical properties. Results on layers made over the complete range of pressures shown in Figure 1, shws differences in insulator capacitance (C_{ins} measured in strong accumulation), flatband bias (estimated at 90% of C_{ins}), hysteresis and surface state density (the slope through depletion) which are all within the range of normal sample-to-sample fluctuations at a given deposition rate. This is in sharp contrast to effects on surface state density seen by exposure of MIS devices to water vapor Ar shown in Figure 4. High frequency capacitance curves are shown of an MIS device made with Photox™ deposited at 0.6 Torr, after exposure to the atmosphere for two months, and after a 16 hour vacuum bake at 60°C. The curves indicate a strong increase in surface state density between the valence band and midgap.

The surface state distribution calculated by taking the difference between the high and low frequency capacitance is shown in Figure 5 for these interfaces before and after vacuum baking. The difference of these curves reflects changes in those surface states which can follow the bias at quasi-static (~0.1 Hz) but not at high frequency (1 MHz). Very fast states and very slow states will not be detected. The latter is in all likelihood a more serious shortcoming for this interface system, especially as these devices show storage times on the order of 3 ms. The region of the energy gap calculated for the bulk alloy is shown as E_v and E_c. The presence of removable water has caused an increase in states about 0.06 eV and 0.13 eV above the valence band edge. Baking recovers the smooth U-shaped distribution of the fresh interface. The other structure seen near the extremes of each curve is frequently seen in C-V analysis and is attributed to nonuniformities in surface potential [14]. We also note that the flatband bias, approximately indicated as 90% of accumulation, is shifted more negative by 0.8V. This is an increase in positive fixed charge of 1×10^{11} cm^{-2}. These effects on capacitance are completely reversible as indicated by the recovery of the initial C-V curve after a vacuum bake.

This indicates that surface state density and fixed charge are altered by the presence of absorbed water which is held in the porosity of the SiO_2 and can be driven off by baking. A portion of the absorbed water is also held in

the layer in a manner where it is not possible to remove it by baking, but does not affect interface electrical properties. This latter is likely incorporated into the bonding of the SiO_2.

We have also investigated some effects of water content on the mechanical integrity of the interface. Layers deposited at different rates were scratched and exposed to nitric acid which dissolves the oxides bonding the interface. The results were observed using a scanning electron microscope. In Figure 6 we compare the types of scratch damage seen in layers deposited at high and low deposition rates and therefore with small and large relative amounts of incorporated water. The layer deposited with the greater water content shows removal only in the immediate vicinity of the scratch, while the edge of the damaged region is characterized by smaller scale structure. The lower water content layer is removed in larger flakes and separates a greater distance from the scratch. This represents an interface more prone to mechanical damage. When these types of layers are exposed to the acid etch for a short time (1 minute) the high water content layers generally show only a slight lifting at the edge of the SiO_2. Those with low water, on the other hand, frequently separate in relatively large areas and, on occasion, we see catastrophic separation of the entire SiO_2 layer.

These results are in agreement with a model for the integrity of the interface being governed by the existence of interface stress due to a difference of the coefficient of thermal expansions (α) of the substrate and deposited layer. For SiO_2 on Si, this causes a compression on cooling after deposition [5]. Increasing the residual Hydroxyl concentration has been proposed as a mechanism to increase the thermal expansion of the SiO_2 and reduce this effect [15]. Since the coefficient for HgCdTe ($\approx 5 \times 10^{-6}$ K^{-1}) is over double that of Si ($\approx 2 \times 10^{-6}$ K^{-1}) between 100 and 400K, the interface stress can be expected to be higher for our samples [16]. It is suggested that the integrity of these interfaces is governed by a balance between the stress in the layer due to expansion coefficient mismatch and the strength of adhesion of the SiO_2.

CONCLUSION

Water has been shown capable of affecting both electrical and mechanical properties of the Photox™-HgCdTe interface. This is introduced either during

the deposition or adsorbed after deposition. The amount adsorbed during deposition is controlled by the deposition rate with the lower rate layers showing more H_2O and SiOH but lower amounts of SiH. This water is incorporated in the SiO_2 bonding and can affect the integrity of the interface, but has no direct effect on electrical properties as measured by C-V. Layers deposited with low water content having a correspondingly high SiH content will, over a period of months, change to a high water content layer with the disappearance of SiH. This may benefit the mechanical stability of the interface with HgCdTe.

Water absorbed after deposition is held in the layer on the extensive inner surface of the layer's inherent porosity. This water, which is not incorporated in the bonding, penetrates all the way to the interface and alters the detailed bonding, increasing the surface state density between midgap and the valence band maximum. Interface fixed charge is increased by about 1×10^{11} cm^{-2}. These effects are completely reversible with the as-deposited properties recovered after a low temperature vacuum bake.

ACKNOWLEDGMENTS

We gratefully acknowledge J.F. Santarosa and E.A. Cady for assistance in taking the capacitance and spectral data, and to C.E. Jones, C.A. Merilainen, R.E. Kvaas, and D.R. Rhiger for many helpful discussions. Finally, to M. Ray and M. Langell for their assistance in sample preparation. This work was supported in part by DARPA Contract No. MDA 903-83-C-0108. The technical monitor is Dr. B. Sumner of NV&EOL and the sponsor is Dr. R.A. Reynolds of DARPA.

REFERENCES

1. W.E. Spicer, J. Silberman, I. Lindau, J. Wilson, A. Sher, and A.-B. Chen. J Vac Sci Tech 1A, 1735 (1983).

2. B.K. Jonousek, R.C. Carscallen, and P.A. Bertrand. J Vac Sci Tech 1A, 1723 (1983).

3. N. Byer. "Insulator Interfaces with (Hg,Cd)Te," Proceedings of INFOS 83. The Netherlands (11-13 April 1983).

4. J.W. Peters, H.N. Rogers, J.T. Hall, E.M. Yee and D.R. Rhiger. Paper No. 202, Electrochemical Society Meeting, 9-14 May 1982, Montreal, Quebec, Canada.

5. M.V. Whelan, A.H. Goemans, and L.M.C. Goosens. Appl Phys Lett 10, 262 (1967).

6. D.R. Rhiger and J.A. Wilson. IRIS Specialty Group on Infrared Detectors, San Diego, CA (1982)

7. J.W. Peters, Tech Digest IEDM, IEEE Proc, 7-9 Dec 1981, p. 240.

8. J.A. Wilson, V.A. Cotton, J.A. Silberman, D. Laser, W.E. Spicer, and P. Morgen. J Vac Sci Tech 1A, 3, 1719 (1983)

9. W.A. Pliskin and H.S. Lehman. J Electrochem Soc 112, 1012 (1965).

10. W.A. Pliskin, J Vac Sci Tech 14, 1064 (1977).

11. M. Maeda and H. Nakamura. J Appl Phys 52, 11 (1981).

12. D.K. Dunlap, Hughes Resarch Laboratories, Internal Report.

13. R.J. Bell, N.F. Bird, and P. Dean. J Phys C1, 299 (1968).

14. R. Castagne and A. Vapaille, Surface Science 28, 157 (1971).

15. G. Hetherington and K.H. Jack. Phys and Chem of Glasses 3, 129 (1962).

16. O. Caporaletti and G.M. Graham. Appl Phys Lett 39, 338 (1981).

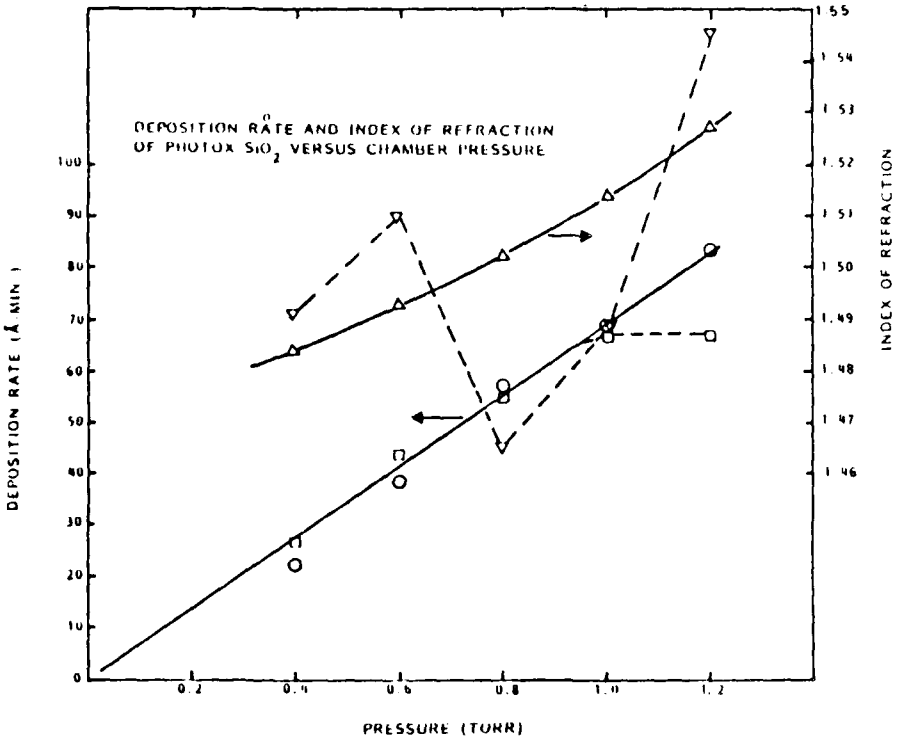

Figure 1. Deposition Rate and Index of Refraction for Photox™ SiO_2 versus Deposition Chamber Pressure at 100°C. Results for Layers 1500Å and 10,000Å Nominal Thicknesses are Shown

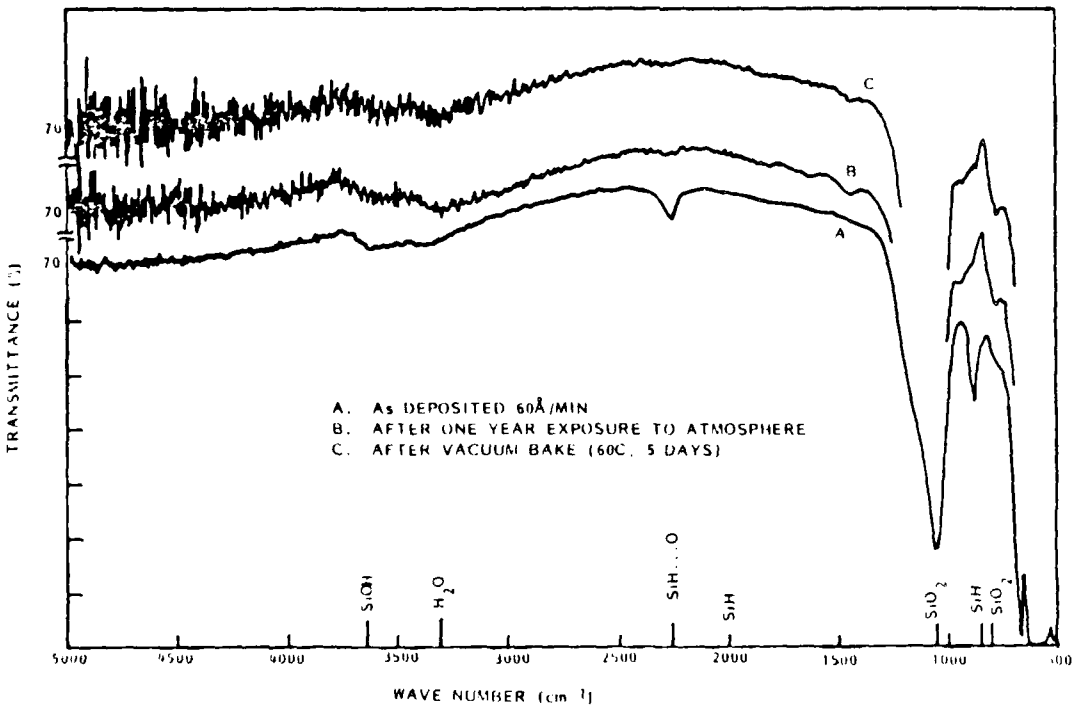

Figure 2. IR Transmission Spectra of 1 μm Thick Photox™ SiO_2 on IRTRAN II. Spectra are Shown for As-Deposited, after One Year Exposure to Ambient Atmosphere and after Vacuum Bake

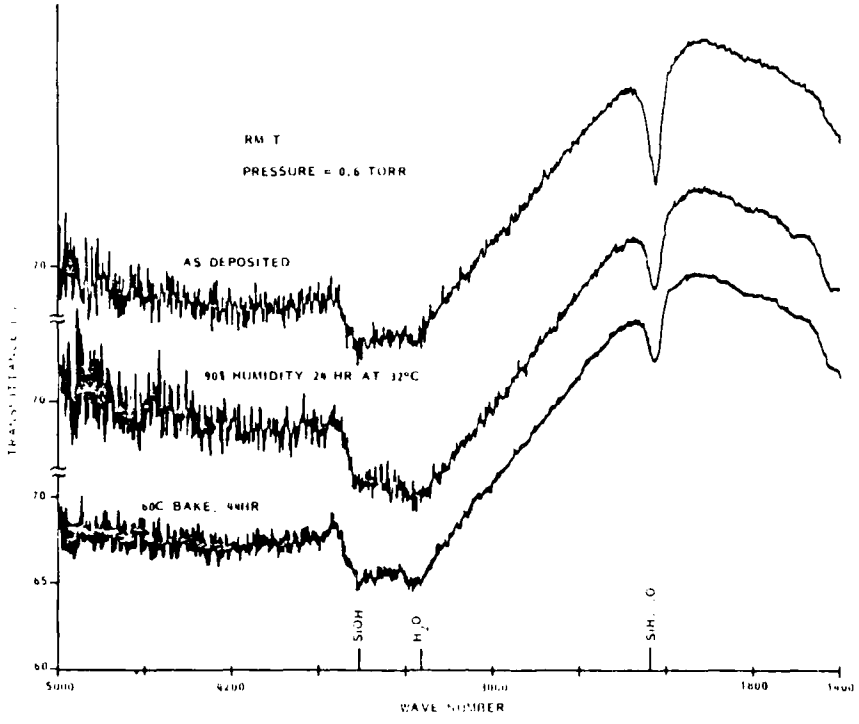

Figure 3. High Resolution Spectra of SiOH and H_2O Features. Spectra are Shown for As-Grown, after Short Exposure to Water Vapor and after Vacuum Bake

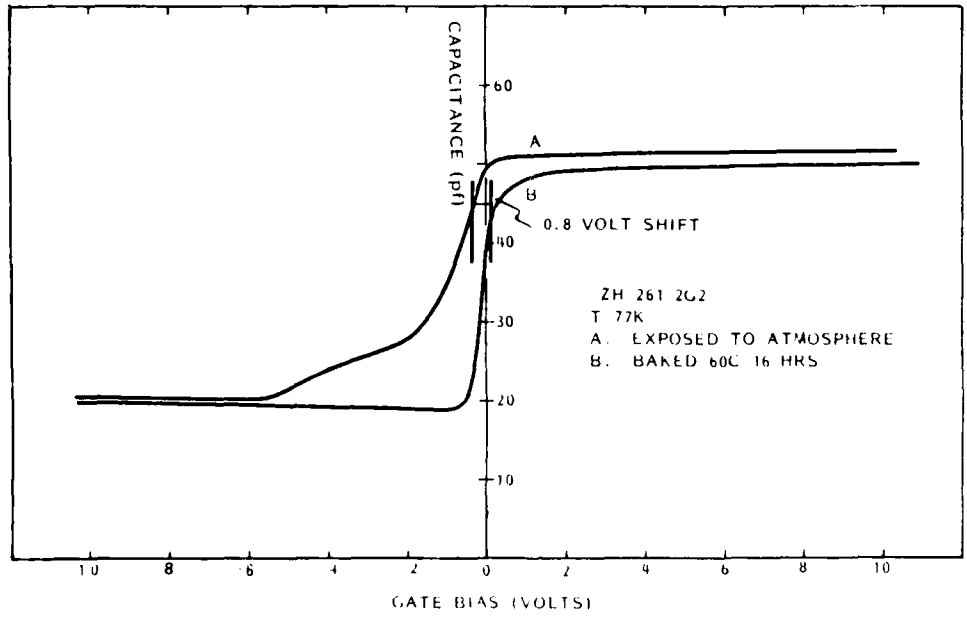

Figure 4. Effect of Absorption and Baking Renoval of H_2O on C-V Characteristics

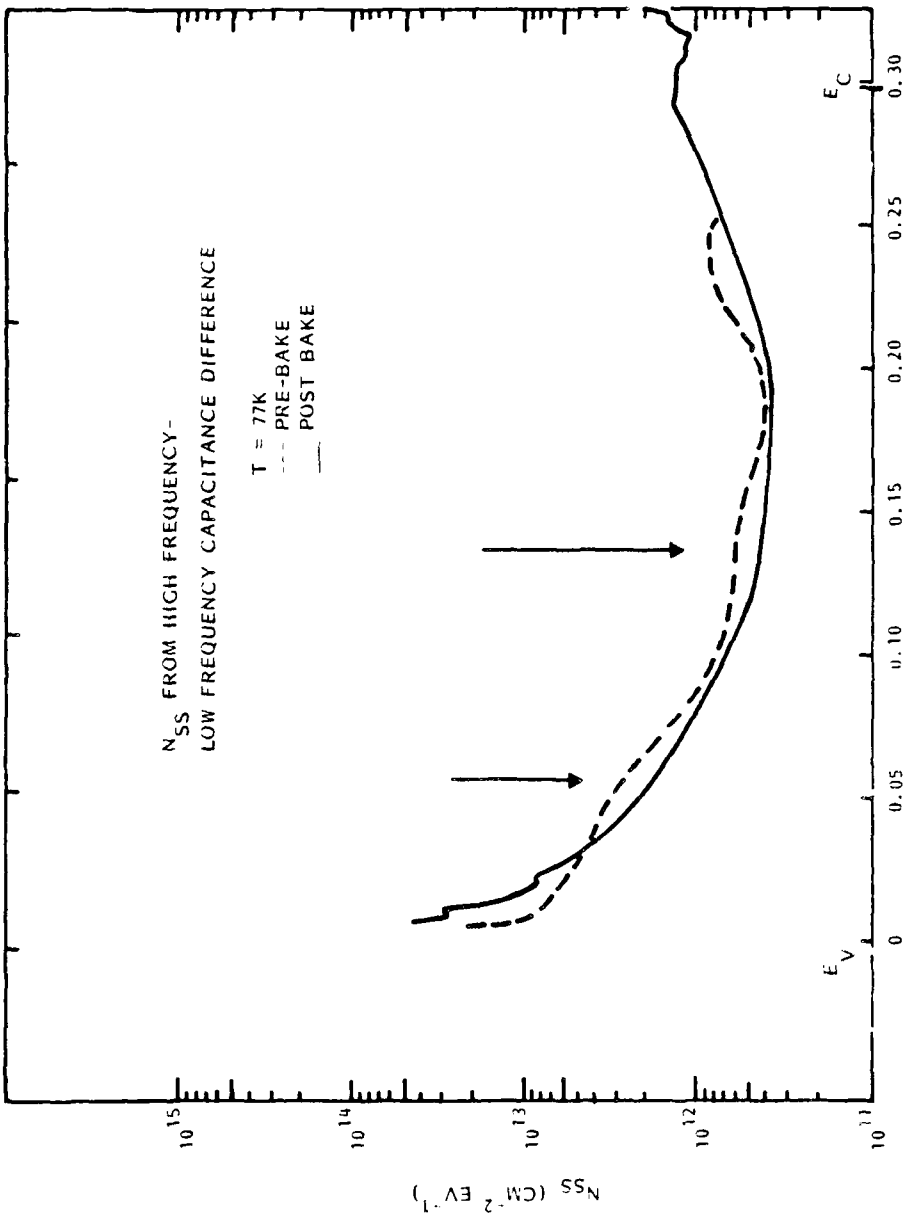

Figure 5. Change in N_{SS} Due to Presence of Absorbed H_2O

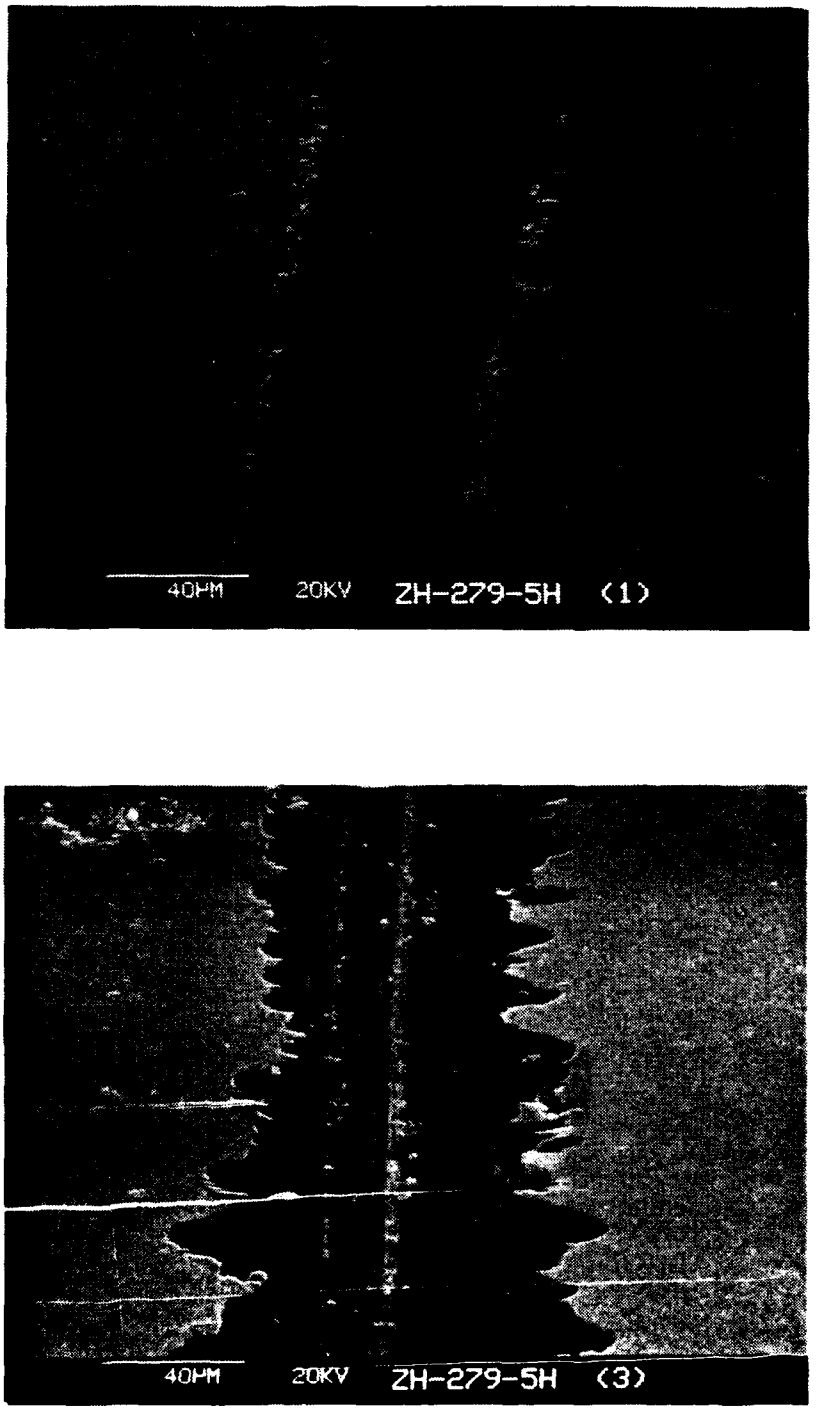

Figure 6. Effect of Deposition Rate Change on Mechanical Integrity of Photox™ SiO_2-HgCdTe Interface. Layers Are Shown Deposited at 20 Å/min (Top) and 60 Å/min (Bottom)

Section 2

SURFACE STUDY

Section II-1

INTRODUCTION

HgCdTe is a promising system for the fabrication of advanced infrared detection and imaging systems. Difficulties in materials growth (high dislocation density, epitaxial layer uniformity) and processing (passivation, type conversion) remain and must be overcome to exploit the full potential of the alloy. Our approach has been to gain insight into these problem areas by studying in detail the fundamental interactions which underlie such macroscopic phenomena as Hg mobility in the lattice and the susceptibility of the alloy to mechanical damage. The original intent (and title) of this project emphasized the interface. Where appropriate, this is still being emphasized; however, it has become clear that the bulk and interface are so strongly coupled that we must address the bulk, as well as the interface, in the most fundamental phase of this program. The following three subsections give recent results obtained in this investigation.

Knowledge of the electronic structure of the alloy provides the means of understanding such diverse properties as the surface oxygen chemistry and bulk hardness. Photoemission studies of HgCdTe combined with theoretical analysis of the band structure[1,2] revealed the selective breakdown of the virtual crystal approximation (VCA) for the cation s-electron derived states which lie at the bottom of the highest valence bands in the alloys. The VCA supposed that the cation potential in HgCdTe can be approximated by a compositionally weighted average of the potentials of Cd and Hg, thereby rendering Hg-Te and Cd-Te bonds indistinguishable. As reflected by the 1.4 eV increase in binding energy of the Hg 6s electrons compared to the Cd 5s levels, the cation potentials are quite different, and the description of the alloy electronic structure must treat the cation potentials individually to be correct. As a consequence of the 1.4 eV shift in valence electron energy from Cd to Hg, the bonding of the metal atom to Te depends on the identity of the cation. Recent

---

[1] W.E. Spicer, J.A. Silberman, P. Morgen, I. Lindau, J.A. Wilson, A.-B. Chen, and A. Sher, Phys. Rev. Lett. 49 (1982) 948.

[2] An-Ban Chen and A. Sher, J. Vac. Sci. Technol. 21 (1982) 138; also K.C. Hass, H. Ehrenreich, and B. Velicky, Phys. Rev. B 27 (1983) 1088.

theoretical studies[3] show that the Hg-Te bond differs from that of Cd by the greater metallic coupling, which served to reduce the strength of this bond. The second subsection discusses the electronic structure of the alloy in greater detail and emphasizes the relationship between this fundamental aspect and the materials problems particular to HgCdTe.

One implication of the difference in Hg-Te and Cd-Te bond strength not discussed in subsection 2 relates to the factors which affect the epitaxial layer-substrate interface. For epitaxial layers grown from the liquid phase, the interface is characterized by a region in which the composition varies from that of the CdTe substrate to the nominal value of the HgCdTe layer and by an extended zone of high dislocation density. (Transmission electron micrographs of this high dislocation density region are presented and discussed further in subsection 3.) The graded composition region typically exceeds 1 μm in width, and the dislocation density of the interface is much greater than predicted on the basis of the close lattice match between HgCdTe and the CdTe substrate. An explanation of the slow composition grading and dislocation formation lies again in the bonding of Hg and Cd. Because of the weakness of the Hg-Te bond, substitution by Cd is favored whenever possible (consistent with the requirements of entropy). The lattice mismatch induced dislocations, which one would expect even at an abrupt interface, may enhance interdiffusion of components, broadening the interface. While these ideas require extensive investigation for substantiation, they suggest the chemistry of the alloy system plays a more direct role in the epitaxial interface formation than does the structural ideal of lattice matching.

The remaining two subsections deal in detail with the subjects of defect structure in HgCdTe as revealed by transmission electron microscopy (subsection 2) and the alloy oxygen chemistry studied by photoemission spectroscopy (subsection 3). In addition to characterization of the defect structure of the epitaxial interface and the cleavage surface, the TEM work investigated the microstructure associated with etch pits on p-type solid state recrystallized material. A correlation was found between pit formation and the presence of Te precipitates. Precipitation of Te and possibly Hg may be another manifestation of the weakness of the Hg-Te bond. Becuase of the ease of creating defects, as well as the high mobility of these defects (including interstitial Hg) in the

---

[3]W.A. Harrison, to appear in J. Vac. Sci. Technol., Proceedings of the 1983 U.S. Workshop on the Physics and Chemistry of HgCdTe, Dallas, TX, Feb 8-10, 1983.

lattice, TEM work and theoretical analysis of dislocation formation remain an important aspect of our continuing effort.

The study of the initial stages of activated oxygen uptake indicates many features of importance to passivation and MIS technology. The oxide film formed upon exposure to oxygen activated by an operating ion gauge in line of sight of the sample (uptake does not occur without such stimulation) grows with the release of Hg. Evidence was obtained that more than one type of oxide forms, with at least one component exhibiting modification with time, although the exact nature of this instability is not clearly known.

Deposition of SiO_2 on HgCdTe has proved to be a high quality passivation technique, and the success of this approach has been attributed to the presence of a thin native oxide film formed by spray etching the sample prior to application of the SiO_2.[4] Current efforts have been aimed at producing the native oxide film in the SiO_2 reactor. Thus, the surface spectroscopic studies of activated oxygen uptake on HgCdTe will begin to give direct insight into the passivation process in addition to yielding more general information on the alloy oxygen chemistry.

---

[4] J.A. Wilson, V.A. Cotton, J.A. Silberman, D. Laser, W.E. Spicer, and P. Morgen, ibid.; also B.K. Janousek, R.C. Carscallen, and P.A. Bertrand, ibid.

(This Page Intentionally Left Blank)

Section II-2

BAND GAP VARIATIONS AND LATTICE, SURFACE AND INTERFACE "INSTABILITIES" in $Hg_{1-x}Cd_xTe$ AND RELATED COMPOUNDS+

W. E. Spicer, J. A. Silberman*, I. Lindau
Department of Electrical Engineering, Stanford University
Stanford, CA 94305

A.-B. Chen, Department of Physics, Auburn University
Auburn, AL 36489

A. Sher, SRI International, Menlo Park, CA 94025

J. Wilson, Santa Barbara Research Center, Santa Barbara, CA 943017

ABSTRACT

This paper brings into focus the differences between $Hg_{1-x}Cd_xTe$ (MCT) and "ordinary" semiconductors such as Column 4, 3-5, and most 2-6 compounds. The key characteristic of MCT which makes it both different and of practical interest is the variation of band gap with composition (zero to 1.5 eV). This paper shows that this benefit is not without its difficulties. In particular, the same unusual characteristic of the Hg atomic states which lead to the advantageous movement of band gap with composition weakens the bonding of Hg in the lattice. This bonding weakness exhibits itself in many ways in the characteristics of MCT, both at surfaces and interfaces and in the bulk. Because of this there is a potential instability associated with the surface or interface; however, this instability depends critically on the crystalline perfection of the MCT to depths far below the surface. The reason for this is that defects move from the bulk to the surface (or in the opposite direction) with surprising ease--even at room temperature. As will be discussed in this paper, this is another result of the weakness of the Hg bonding in bulk MCT. In this matter of movement of defects from bulk to surface and vice versa, MCT differs greatly from the other 3-5 and elemental semiconductor studied in detail to date. This difference will

be discussed in more detail in this paper. The extreme susceptibility of MCT to mechanical damage is also related to the weakness of the Hg bonding. One object of this paper is to make a first attempt at showing how the Hg bonding affects the electronic structure, lattice bonding, and defect structure of MCT. A key phenomena in the electronic structure is the breakdown of the virtual crystal approximation which has worked to a good approximation in all other covalent semiconductors studied to date. This breakdown is selective and involves only those valence states near zone boundaries containing large cation s wavefunction admixtures. This again reflects the unusual character of the Hg atomic 6 s^2 valence state. Thus, a focal point for understanding the wide range of unusual phenomena in MCT developed in this paper is understanding of the Hg atomic structure and its effect on MCT electronic structure, bonding defect formation and related phenomena. This characteristic of Hg is common to elements with high atomic number and similar or related characteristics can be expected from semiconductor compound alloys containing such heavy atoms.

+ Work supported by DARPA contract 800989-B8 and by AFOSR Contract F49620-81-K0012
† Stanford Ascherman Professor on Engineering
* Fannie and John Hertz Foundation Fellow
# Mailing Address: Stanford Electronics Laboratory, Stanford, CA 94305

Introduction

We will attempt to correlate a number of phenomena in $Hg_{1-x}Cd_xTe$. To gain perspective, comparisons between $Hg_{1-x}Cd_xTe$ and other semiconductors will also be important. There will be an emphasis on surface and interface properties; however, in order to give the necessary perspective, bulk properties will also be considered.

While some of the things about which we will write are well established, others are in a much more speculative stage. An attempt will be made to indicate the speculative conclusions. A unifying theme is the strength of Cd-Te and Hg-Te bonds in the crystal. We will suggest possible correlations between this bond strength and a number of properties of interest in $Hg_{1-x}Cd_xTe$ (MCT).

Surface states on MCT and other covalent semiconductors

As in the 3-5 compounds [1,2], it has been established that there are no intrinsic surface states within the band gap on the (110) face of $Hg_{1-x}Cd_xTe$, and there seems no reason to expect them on other crystal faces of MCT [2]. Here the word "intrinsic" has the same meaning as in the bulk of the semiconductor, i.e. it denotes the states associated with a perfect sample having no defects or impurities; if "dangling" bond states occurred in the band gap, one would expect one filled intrinsic surface state per surface atom. As in the 3-5's, the surface chemistry favors electronic and lattice reconstruction so that the intrinsic surface states are swept out of the band gap. (The filled surface states are moved below the valence band maximum (VBM) and the empty surface states above the conduction band minimum (CBM).) In terms of the older picture of "dangling bonds" at the semiconductor surface, this means that the electronic and lattice reconstruction at the surface "satisfies" the

dangling bonds to the extent that it is easier to remove an electron from the valence band maximum than from the intrinsic surface ("dangling bond") states.

Thus, the perfect surface will not have states within the band gap. However, perfection is an ideal never achieved. There will be lattice defects and/or impurities associated with the surface. For a clean surface, it is only the lattice defects (vacancies, anti-site defects, etc.) which can be present in sufficient numbers to be important. For example, 10^{12} - $10^{13}/cm^2$ acceptor defect levels can "pin" the Fermi level at the surface on an n-type sample and thus deplete or invert the surface of an n-type crystal. In the 3-5's, extrinsic defect levels play a key role for the MIS, MOS and Schottky barrier semiconductor interfaces and the same situation would be expected for MCT.

Unique Behavior on the MCT Surfaces and Interfaces

In the wide range of semiconductor surfaces studied before MCT, it was possible to make a very critical approximation. It was assumed the surface defects are permanently localized at or very near the surface. One does not worry, to first order, about defects moving from the surface region into the bulk or vice versa. The situation is quite different in MCT. Recent work discussed below reports that movement of defects over hundreds of angstroms plays a critical role. (Here mobile Hg is considered a defect since it would be associated with vacancies or with Hg atoms either in interstitual positions or moving along dislocations, sub-grain boundaries, etc.) As will be shown, the details of such movement depend on the history of the particular MCT cyrstal being studied. It is essential that the MCT worker understand and differentiate between these two facets of the problem: first, the ease of movement of defects between the

surface (this may be the free surface or the MCT surface beneath a passivating layer) and the bulk which can occur at room temperature; and, second, that the degree of such movement will depend critically on the history of the MCT sample. We are told by those accustomed to handling MCT crystals in device fabrication that the surface can be easily transformed from p- to n-type by mechanical deformation of the surface; based on the studies we will describe below, we would attribute this to creation and transport of appropriate defects to the surface. To support this, we should review the more detailed "well controlled" studies which have lead to the conclusions stated above. These involve the vacuum MCT interface. We will concentrate on two sets of studies centered at the University of Munster in West Germany [3], and Stanford University [4], respectively. These studies are very striking because they involve the vacuum MCT surface and thus the sophisticated tools of surface science could be brought to bear. Moreover, the Stanford work was extended in a very valuable way by electroreflection work done at the University of Illinois--Chicago [5,6] (not done under vacuum).

Table 1 indicates the salient results obtained by surface science methods in the U.S. and Germany. The conversion of p- to n-type on cleaving also is reported in these Proceedings by Davis et al. [7]. The first key result from Munster is that there was enormous Hg loss from the surface in their samples and that this loss results in defects relatively deep (on the order of microns) into the material. Comparison of the Munster and Stanford results give (see Table I) the second key result--the details of the changes depend on the history of the crystal prior to its long term examination in ultra-high vacuum (UHV). The Munster samples were annealed in Hg to convert them from p-type to n-type. Schaake, et al. [8] give, in these Proceedings, evidence that such a procedure can intro-

duce dislocations. These in turn may be significant for the long term out diffusion of Hg observed in University of Munster [3] but not in the Stanford results [4]. Defects associated with the original crystal rather than Hg anneal may have also contributed to the strong Hg outdiffusion observed at Munster.

It must be emphasized that the Hg loss observed at Munster (~ 50%) was greater than the amount introduced to convert the sample from p- to n-type (of order 10^{-4}%) by a large factor (almost 10^{6}). Thus, the outdiffusion of Hg in the University of Munster samples cannot be explained in terms of the loss of the extra Hg introduced during annealing to convert the sample from p- to n-type. In fact Hg was still being lost from this crystal when it was highly (10's of %) deficient in Hg. Therefore, it can not be explained by the sample lying on the Hg rich side of the phase diagram unless the starting samples contained enormous quantities of Hg in Hg inclusions and it was the Hg from these inclusions which was lost from the surface. However, this seems unlikely since the Munster group found the Cd content to rise as the Hg content decreased--a result most easily explained by metal atoms hopping through cation vacancies.

There is a further complication in interpreting the Munster data. Is a MCT sample which has lost 10's of % of Hg in the near surface region still crystalline? To what extent do Te atoms move into the cation vacancies. We intend to pursue these questions using LEED and other tools to study samples in which controlled amounts of Hg have been removed by heating in vacuum.

As Table I indicates there is no corresponding loss of Hg from the Stanford sample after cleavage--despite the fact that the Munster sample still loses Hg when it is many orders of magnitude more deficient in Hg than

the Stanford sample. Based on this we argue that imperfections such as dislocations, inclusions, etc, must be playing the key role. For the Munster sample these may be due to some combination of the original crystal growth, the Hg anneal to transform the solid state recrystallized crystal from p- to n- and the "spinning razor" method of surface cleaning. On the other hand, the Stanford sample did not undergo a Hg anneal, was grown by solid-state recrystallization by an entirely different crystal growth group, and had a surface prepared by cleaving. We should add that the difference in surface preparation may not be as important as it first appeared [2]. This idea is based on the fact that the Stanford samples were found not to change their surface composition with time even when microns of material were removed by a diamond disk [9].

The Munster work gives clear evidence of how easily the Hg can move though and out of some MCT crystals at room temperature. Further evidence of this at higher temperature is given by the studies of Farrow *et al.*[10]. Whereas the Stanford work illustratesthat these depends on the crystal since they found no such long term high level Hg outflow at room temperature from crystals grown at Santa Barbara Research Center.

We would like to discuss the results quoted above and include perhaps a naive discussion of diffusion. Brown and Willoughby [12] have recently reviewed the MCT diffusion literature and emphasized both the complexity of the processes involved and the difficulty of rigorous theoretical analysis. For our purposes the diffusion coefficients obtained by the Munster group in studying out diffusion of Hg are of particular interest [3]. It is interesting to note that the measured diffusion coefficients for Hg and Cd deduced by them from the composition versus depth after large Hg loss are similar [3]. (As will be discussed in the next paragraph we believe

that the large Cd diffusion coefficient is related to the enormous number of Hg vacancy sites into which they can hop.) Due to this large Cd diffusion coefficient the Cd builds up at the surface whereas the Hg is depleted. Thus, it does not appear that the long term preferential loss of Hg can be explained in terms of differences in diffusion. It may be due to the bonding of Hg in the lattice and heat of evaporation of free Hg both being lower than for Cd. As will be discussed in detail later in this paper, the difference in bonding is related to the large difference (1.4 eV) in the binding energy of the valence electrons on Cd and Hg atoms. Harrison shows in these proceedings [1] the difference in binding energy of the Hg and Cd valence electrons can not only lead to a change in bond energy of the Hg atom but also to a change in the nature of the Hg-Te bond (from covalent toward "metallic").

It seems appropriate to examine the question of diffusion in more detail. We would like to bring up the possibility that the large diffusion coefficients measured for Hg [3,13,14] and Cd [3] in MCT (on the order of 10^{-12} - 10^{-13} cm^2/sec at room temperature) are characteristic of MCT with a very significant number of cation vacancies present and/or that the activaction energy for forming Hg vacancy is insignificant compared to the activation energy for vacancy motion. It should be noted, for example, that the diffusion coefficients reported earlier for Cd in MCT [3] are approximately 10^{20} greater than those characteristic of self-diffusion Cd in CdTe [12]. As pointed out by Brown and Willoughby, the values for Cd in CdTe are true self-diffusion coefficients, i.e. they are measured under isoconcentration conditions. This is not the case for the diffusion coefficients obtained, for example, in the Munster studies.

We tentatively attributed the lower value of "self-diffusion" in MCT to the

fact that only the activation energy for vacancy motion is important and that the higher value in CdTe includes the activation energy for creation of Cd vacancies in CdTe. An alternative is that both the Cd and Hg atoms move on dislocations; however, we find this unattractive since the activation energy for breaking Cd-Te bonds and moving a Cd atom from a lattice site to a dislocation or other high mobility site will be considerably greater than the corresponding energy for Hg. We base this suggestion (not only) on such macroscopic quantities as the difference in heat of formation of CdTe and HgTe, and the loss of mechanical strength in HgTe and Hg rich MCT as described by Cole in these Proceedings [15] but on an argument on the "atomic" level of the difference of the Hg-Te and Cd-Te bonds as discussed in this paper and that of Harrison [11] in these Proceedings. However, it is emphasized that the conclusions drawn here about the Hg-Te bond and Hg movement in MCT must be treated as very tentative in nature and require much more evidence before they can be accepted as established. In particular the structure of highly Hg depleted MCT must be determined.

To return to the very high diffusion coefficients of Hg and Cd in MCT at room temperature, (within the limitations placed above) we would like to suggest that the presence of large densities of dislocations or other "line" defects along which Hg can diffuse results in a loss of Hg from the lattice with a corresponding number of cation vacancies in the lattice. Once this condition has been reached, diffusion of both Hg and Cd occurs with relative ease via the vacancy mechanism. Thus, the high diffusion coefficient found, for example, in the Munster work [3] would be a result of this "two step" process. Note that the first step depends on the presence of dislocations or other "line" defects and, thus, will depend strongly

on the crystal history.

The n-type conversion and other changes on cleaving found at Stanford are even harder to understand than the Munster result. This is due to the fact that it is a transient effect which takes place completely during the moment of cleaving. It was not possible to measure any outflow of Hg after the cleavage was completed using photoemission spectroscopy (PS) [4]. This method is capable of measuring a change of one or two percent in composition and no change was measured over a period of 20 hours [4].

Before going forward in the discussion of the type conversion on cleaving, we should mention three other experimental results. First, the p- to n-type conversion was not observed in two cleaves (approximately 10 % of the cleaves made). Second, no measureable changes in the conversion have been found to date (i.e. the conversion is stable over a period of at least many months). Removing the crystal from vacuum into the atmosphere did not effect the type conversion [5,6]. Third, PS samples only a few atomic layers [16]; however, electroreflectance (ER) measurements, which sample several hundred angstroms [5,6], also found the type conversion down to the probing depth in ER. The upper limit, set by the amount of material removed by chemical etching is several microns [5,6].

Because of the "instantaneous" nature of the type conversion on cleaving, it is probably best understood in terms of a shock wave being produced at the surface at the instant of cleavage--this is proprogated into the crystal--being attenuated with depth and time. Using the arguments given above it is attractive to suggest that the "shock wave" allows Hg to be released from lattice sites and that the strain gradient associated with the shock wave induces their movement toward the surface. Te anti-site defects may then form, leaving Te vacancies which pair with Hg vacancies and

move to the surface where they disappear. Since a Te anti-site defect forms a donor, the n-type conversion occurs. Alternately, one could assume that enough Hg vacancies were removed to allow n-type impurities to convert the material to n-type; however, this is not as attractive a model since there is no evidence that all the crystals we studied had a sufficiently high density of n-type impurities. The lack of conversion in 10% of the samples might be explained in terms of a combination of almost ideal cleaves producing minimal shock waves, perfection of the crystal in the vicinity of the cleave and/or lack of n-type impurities at the point of cleave. It is hoped that TEM and other studies now underway can establish the mechanism of conversion much more precisely.

Correlations Between Electronic structure, the Hg-Te Bond and Mechanical Properties of HCT

A key objective in science is to unify. It is our purpose in this section to outline a unifying theme tying together the features of the fundamental electronic structure of MCT (which makes it a premier infrared detector) and its mechanical and chemical properties which make it a most difficult material from which to form devices.

One must look at the atomic structure of Hg and compare this to that of Cd and the other metals which make up tetrahedrally bonded compound semiconductors (See the article by Harrison [1] in these Proceedings for a more detailed discussion of this). The key is to recognize: 1) that the valence electrons of the column II metals have s^2 character and 2) that there is a singular change in the binding energy of s^2 electrons in going from lighter metals to Hg (or any other metals of the 6th row of the periodic table). To be more specific, the ionization (i.e. binding) energy of the Hg $6s^2$ valence electrons is 1.4 eV greater than that of the Cd $5s^2$ valence electrons. In contrast, the energy of the 6p and 5p

levels of Hg and Cd respectfully change less as one goes from Cd to Hg. In order to understand this behavior, two factors must be considered. First the s valence electrons penetrate the core levels and have appreciable probability to be found near the nucleus. This is not the case for the p-valence orbitals. Second, the change in nuclear charge in going from Cd(Z = 48) to Hg(Z = 80) is so large that relativistic effects become important for Hg which are not significant for Cd. This leads to the singular 1.4 eV increase in binding energy of the $6s^2$ Hg valence electrons.

Let us first look at the effect of this shift on key features of the MCT electronic structure. These are illustrated schematically in Fig. 1 and must be understood in the context of band theory. More detailed discussion of these points will be given in the paper of Chen et al. [18] in these proceedings.

Although the effect of the difference in binding energy of Cd and Hg s^2 valence levels on the $Hg_{1-x}Cd_xTe$ conduction band minimum has been recognized for some years [19], it was the experimental detection of a breakdown in an approximation, the Virtual Crystal Approximation (VCA), in the course of our photoemission studies [17,20] combined with Coherent Potential Approximation (CPA) calculations [17,21] which led to an appreciation of the much more general effects produced by the increase in binding energy of the Hg $6s^2$ valence states.

In order to explain the phenomena outlined above and in Fig. 1, it will be useful to explain the critical differences in VCA and CPA and to relate these to salient features of E vs k diagrams such as those presented in Fig. 1. In VCA, the individual potentials which characterize the Cd and Hg atoms are not taken into account. Rather, a weighted average of the two potentials is assigned to each cation site in the crystal lattice. In

contrast, CPA takes into account the fact that the potential is different on the Cd and Hg sites. As Chen et al [18] show in these Proceedings, the difference between CPA and VCA is not important for the conduction band minimum (CBM). As they explain in more detail, this is due to the character of the quantum states near CBM. Since the CBM occurs at the center of the Brilluion Zone (Γ point), the electron wavenumber is zero. That is, the wavelength ($\lambda = 2\pi/k$) is infinite. For electrons in the low density of states region near the CBM the λ is very long since k is changed by very little from that at the CBM. The very long electron wavelength near the CBM allow these electrons to average over many lattice sites and thus the VCA approximation works well despite the fact that the wave functions are made up principally of Cd 5s and Hg 6s states. As a result, the CBM just moves down toward the valence band maximum (VBM) monotonically as the Hg content is increased and the electrons feel increasingly the stronger Hg potential [18].

In contrast, the VBM is not directly affected by the difference in cation potential for the valence electrons. This is because the quantum states near the VBM are made up primarily from the Te p-states and thus are insensitive to the potential for the cation states.

A third type of behavior was first reported at the first MCT workshop [20,21] and has been reported on in more detail [17] prior to this meeting. This is the behavior of quantum states near the bottom of the highest lying valence band. These are located 4 to 6 eV below the valence band maximum and occur not near the center of the Brillioun zone where the electron wavelength is very long but near the zone boundary, where the wavelength is close to the crystal unit cell dimension. The short wavelength combined with the heavy mass of the electrons in these states and the narrow band width

of the "s-derived" states combine to give the electrons the capability of sensing the potential at individual atomic sites. This would not be important were it not for the fact that these quantum states have a high admixture (approximately one-half) of cation valence s character. Thus, their energy will be affected by local interactions with individual Cd or Hg atoms. To be more specific, this portion of the band structure will move by as much as one eV depending whether the wavefunction "sees" a Cd or Hg site. As Fig. 2-4 show this has a profound effect on the band structure as seen by photoemission spectroscopy (PS) [17,20]. Thus, VCA breaks down for these states and CPA must be used [18,21,22]. This is shown dramatically by Fig. 4.

Fig. 4 gives PS data covering not only the valence band of MCT but the Hg $5d^{10}$ and Cd $4d^{10}$ core-like states. Data for five samples with indicated composition are included in Fig. 4. Fig. 2 shows only the valence band states so that the difference in behavior of the upper (p-like) valence band lying within -3.5 eV of the VBM can be compared with that of the feature lying between -4 and -6 eV which contains the strong cation s admixture in its wavefunction--the solid lines in Fig. 2 indicate the center of this band in pure CdTe (-4.6 eV) and HgTe (-5.4 eV). Note that, while the changes for the p-derived band are relatively minor in going from CdTe to $Hg_{.71}Cd_{.39}Te$, there is a first order effect in this change of composition for the s-derived band. This illustrates the difference in structure in these two parts of the valence bands, i.e. the p-like band follows VCA; whereas, it breaks down for the s-derived valence states. This is further illustrated by Fig. 3 which compares the VCA and CPA calculations with experiment for the s-derived bands. As can been seen, VCA behaves quite differently from experiment; whereas, reasonable agreement is found between CPA and experiment. This agreement is

particularly striking when it is realized that no broadening has been put into theoretical results while the experimental results are broadened by both lifetime and instrumental effects [10].

The behavior in the s-like valence states is directly related to the bonding. Consider the nearest neighbor bond, i.e. the Cd-Te or Hg-Te bond. As mentioned above, because of the short wavelength, large effective mass and small band width of s-derived valence states shown in Fig. 2 and 3, these are also localized and show a difference of almost 1 eV for the s-derived valence states on Hg and Cd sties. The "localized" nature of the s-derived valence states deep in the valence bands is indicated by the states 4 to 6 eV below the VBM in Fig. 1. This large difference will have a major effect on the covalent bond since one s state per atom must be emptied to form the covalent bond characterized by the tetrahedral bonding of MCT. As Harrison illustrates in his paper [11] and Chen et al.[18] are beginning to investigate using CPA, this leads not only to weakening of the Hg-Te bond as compared to the Cd-Te bond but changes the nature of the bond. This in turn can lead to the ease of plastic deformation in MCT as reported by Cole [15] in these Proceedings.

Much more must be done before the bonds in MCT, their connection with such microscope quantities as dislocation formation, epitaxial growth, and mechanical and chemical stability can be fully understood. It is hoped that the work and concepts reported here will help stimulate the necessary work. There is additional information in Figure 4 which may help in this process. This is the "chemical" shift in the Hg and Cd d-core levels on going from either HgTe or CdTe into the alloy. Note that the Cd 4d drops to greater binding energy and the Hg 5d rises to lower binding energy. This suggests that the Hg is less strongly bonded on going from HgTe to MCT;

whereas, the Cd-Te bond may become stronger. This can be crudely understood in terms of the "desire" of the Te for additional electrons which it can obtain more easily from the Cd than the Hg because of the less tightly bound Cd valence s-electrons. Thus, the Cd atoms surrounding a given Te may become more positive as the number of Hg atoms surrounding the same Te increases from zero. This may help explain the greater materials difficulties with high x $Hg_{1-x}Cd_xTe$. However, more quantative work must be done for a comprehensive understanding of the chemical binding and core shifts in MCT.

Surface, Interfaces, the Cation-Te bond, Defects, Dislocations, Etc.

In the third section of this paper (Unique Behavior of MCT Surfaces and Interfaces), we emphasized the unique ease with which defects can move from the bulk into the surface and vice versa. In the preceding section, we connected the electronic structure, the nature of the Hg-Te bond, and the mechanical properties of MCT. Conceptually it takes but a small step to connect these phenomena and realize that the ease of formation and movement of electrically active defects is intimately connected with the special character of the Hg-Te bond discussed in the last section. It is also important to realize in developing passivating processes for MCT surfaces that, as Cole has reported [15], the mechanical properties of MCT at room temperature are similar to those of Si at over 1000° K; thus, one must be much more sensitive to the possibility of "mechanical" damage in the MCT surface region and the effect of this on the properties of devices "surfaces".

Another consideration is the extreme resistance of MCT to oxidation as reported by Silberman et al. in these Proceedings [23] and elsewhere [4]. It is interesting to note that these workers also have evidence [4,23]

that oxidation is initiated by removal of Hg from the surface thus forming Hg vacancies. It is likely that some of these or other defects produced in this process move into the region beneath the oxide thus causing type conversion or other changes in the electronic characteristics at or near the oxide: MCT interface.

It should also be noted that there is a great difference in the strength of the bonding of Hg, Cd, and Te with oxygen. Thus stochiometric oxides may not be the most profitable passivating layers to pursue. This problem has been studied in much more detail previously with the 3-5 native oxides [24]. Rhiger and Kvass present important work of this type for MCT in these Proceedings [25]. Relatively early (1977), we suggested [24] that a more profitable approach than native oxides to passivating 3-5 materials would be the deposition of "foreign insulators" such as SiO_2 and Al_2O_3 and this has appeared to be the case [26]. As Wilson et al. [27] and Janoucek et al. [28] report in these Proceedings, interesting results are being obtained using this approach in MCT.

To summarize this section, one must be particularly careful in forming passivating layers on MCT not to introduce defects in the MCT. One also must consider the possible chemical reactions between the passivating layer and MCT. For example, if the passivating layer contains Hg oxides, these will be thermodynamically unstable in the presence of MCT with the equilibrium reaction involving reduction of Hg oxides and oxidation of the Te and, perhaps Cd from the MCT [25]. Such a process can clearly lead to electrically active defects in the region of the interface.

In the third section of this paper, we emphasized the importance of the history of the sample in determining the character of the surface. Clearly the same considerations apply to the interface with a passivating overlayer.

Detailed considerations will not be reexamined here. Rather the reader is referred to the third section of this paper.

There is another consideration in terms of placing a passivating layer on MCT. This is adherence of the foreign layer to the MCT surface. This is at variance with the other considerations we have outlined above for forming a passivating overlayer. According to the criteria above, one would want to minimize the interactions between the overlayer and the MCT; however, how can this be done and adherence obtained? We will comment on this problem in the next section which treats the passivating layers most used to date.

Practical Passivating Layers

Our purpose in this section is three fold. First, to set up criteria for acceptable passivation layers. Second, to briefly review the principle types of overlayers used to date and results from these. The last objective is to suggest ways in which the result to date may tie in with the preceding discussions in this article.

For both photoconductive and photovoltaic devices the passivating layers must satisfy the following criteria (the criteria, in some cases, may differ significantly for specific devices). The passivating layer must be:

1) A good insulator
2) Adhere sufficiently well to the MCT
3) Be time stable
4) Be stable against the atmosphere (unless it is hermetically sealed)
5) Not be attacked by chemicals necessary for making the device
6) Be sufficiently nonporous that atmospheric gases cannot move through it and attack the MCT.

7) Produce an interface which is sufficiently inert electrically so that it does not degrade the operation of the photodetector in an unacceptable way.

Three widely used passivating materials are listed in Table II with some of their most important properties. For photoconductive devices anodic oxides (see articles by Kaiser et al. [29] and Seelmann-Eggebert et al. [30] in these proceedings) have proved satisfactory and have been successfully used for device production. However, they have high fixed charge at the interface which usually prevented their application to photvoltic devices. SiO_2 deposited at low temperatures (see the paper by Wilson, et al in these Proceedings [27]) and ZnS have provided passivating layers for photovoltic devices. Their advantages and disadvantages are listed in Table II.

In attempting to explain key results given in Table II in terms of the criteria set up in this paper we will start with the anodic oxides. Because of the different chemical activities of the three elements which make up MCT and the relative stabilities of those oxides discussed in the last section, it is not surprising that the fixed charge is a problem at the interface. We suggest that this is due to charged defects near the interface in the MCT and/or oxide. Due to the difference in activity of Hg, Cd, and Te mentioned above, it would be surprising if the anodic oxide could be grown without creating such defects. However, even if this were achieved, the inherent chemical instability of Hg in oxide (discussed in the preceding section) would probably prevent anodized photovoltaic devices from having sufficient long term stability. The "built in interface charge" which has characterized anodized interfaces to date presents a further difficulty with anodization.

In placing foreign layers such as ZnS and SiO_2 on the surface of MCT,

one problem is the creation of electrically active defects at the interface due to Hg being freed by the "impact" of deposition. We know of no evidence that this is a critical problem with ZnS. If the MCT must be raised to elevated temperatures in order for the deposition to take place, as for SiO_2, there can be additional problesm of Hg outdiffusion from the MCT. As with the vacuum surface, the severity of the problem will depend on the complete history of the MCT. With SiO_2, the problem is reduced by reducing the deposition temperature and by using special techniques such as ultraviolet irradiation or plasma excitation. If depositions at elevated temperatures can be successfully done, it is likely that such devices will be stable against temperature cycling. The instability of ZnS to temperature cycling is probably associated with the lack of deposition at elevated temperatures.

The facts that fixed charge can be produced by blue or UV light in ZnS but that this does not appear to be a problem with SiO_2 is probably just a reflection of the factor of 2 difference in band gap of the two materials (SiO_2--about 8 eV as opposed to about 4 eV for ZnS). The same is probably true of the difference in insulating properties of the two ad-layers. The adherence problems found with SiO_2 but not ZnS probably reflect a greater difference in lattice parameter and chemistry between MCT and SiO_2 than between MCT and ZnS.

It is interesting that Wilson et al. [27] report that the best results are obtained with SiO_2 when a few layers of "natural" oxide are present on the MCT before the SiO_2 deposition. It is suggested that this will be helpful in protecting the MCT during the SiO_2 deposition (and hindering any Hg outflow at the elevated temperature.) It also may help in adherence. The fact that the "native" oxide can be detected before SiO_2 deposition but not afterward may indicate that the oxide tends to be removed or incorporated

into the SiO_2 during the deposition process.

Conclusion

$Hg_{1-x}Cd_xTe$ has important advantageous for infrared photodetection; however it has the most serious material problems of any semiconductor in mass production. A general objective of this paper has been to establish that the band gap tunability which makes it so attractive as an IR photodetector, is due to the difference in binding energy of Hg $6s^2$ and Cd $5s^2$ atomic valence levels and that this difference in turn contributes to the weakness of the Hg bonds in the lattice. The Hg bond weakening contributes strongly to the materials problems associated with fabricating devices from this material and to the high susceptibility of the material to mechanical damage. On a more microscopic scale, the weakness of the Hg bonding in the lattice should lead to the ease of formation of Hg vacancies and, we suggest, various types of dislocations and other defects such as inclusion of Hg or Te. The combination of these can lead to relatively easy motion of Hg through the lattice and to other non-equilibrium phenomena not easily described by phase diagrams. Of particular importance for surfaces and interfaces is the ease of movement of defects into (or from) the surface or interface at room temperature. $Hg_{1-x}Cd_xTe$ is distinguished from all other covalent semiconductors studied intensively to date by this transport of defects between the surface and the bulk. Data reviewed in this paper suggests that the degree and type of this transport depends strongly on the past history of the $Hg_{1-x}Cd_xTe$ crystal, i.e. the defect structure not only at or near the surface but many microns into the semiconductor.

In placing or growing passivating layers on the $Hg_{1-x}Cd_xTe$ surfaces, all of the considerations outlined above must be taken into account. In

addition other issues arise. Perhaps dominant among these are the problems of inducing additional defects by producing the passivating layer. Defects may be induced due to the mechanical "shock" associated with addition of the passivation layer (particularly when a foreign layer is deposited) or the complex chemistry involving, for example, the anodic oxidation of $Hg_{1-x}Cd_xTe$, which may produce defects. In the latter case, not only must one be concerned with defects produced at the time of oxide growth but with the stability of the oxides produced (Hg oxides may not be stable in the presence of $Hg_{1-x}Cd_xTe$). Another fundamental problem is that of adhesion of deposited films. How is this to be achieved without intermixing of the deposited film and the $Hg_{1-x}Cd_xTe$? The practical work to form passivating layers is reviewed in this paper and advancements in solving these problems briefly indicated.

Acknowledgement:

We would like to express our appreciation to Roger A. Cole at SBRC for crystal growth and to Stanford University High Vacuum Apparatus Lab for essential help in the Stanford portion of this work. We are grateful for stimulating conversations with Tom Casselman, Paul Raccah, and Dick Reynolds.

TABLE I

	University of Munster and Telefunken	Stanford, SBRC, and University of Illinois - Chicago
Type of Crystal	Wafer - Annealed to Make n-type	0.5 x 0.5 x 1.5cm; Solid State Recrystallized p-type as grown
Surface Preparation	Surface Cleaned With "Spinning Razor"	Cleaved (but similar results obtained when material in UHV removed with "diamond wheel")
Character of urface After Preparation	Hg Outdiffuses; Surface ~ 50% depleted of Hg after 50 hr; Cd 20% enhanced; Hg depletion to depth of several microns.	No Hg outdiffusion after cleave; cleave usually converts surface to n-type to depth 100's of Å or more, cleave may increase x - from, e.g. 0.20 to 0.22

TABLE II

Principal Present Passivation Layers For MCT and some of their characteristics

Anodic Oxide:

- Easy to grow
- Adequate insulator
- High fixed charge (usually) - can invent HCT surface -
  - Prevents use on PV devices
  - Attacked by some processing chemicals.

ZnS:

- Easy To Apply
- Attacked by air - water soluble (o.k. if vacuum sealed)
- Difficult to handle in lab environment
- Some instability to temperature cycling
- Fixed charge can be produced by exposure to blue or UV light (annealed away in dark)
- Poor insulator compared to SiO_2

Low Temperature CVD:SiO_2 (Photochemical, Plasma Excited etc.):

- Excellent Insulator
- More porous than thermally grown SiO_2 - can absorb H_2O
- Excellent interface electrically
- Some adherence problems

(Best when deposited on HCT covered with a few layers of "natural oxide" - protection against damage? adherence?)

REFERENCES

1. W. E. Spicer, P. Skeath, C. Y. Su, and P. Chye, Phys. Rev. Lett. 44, 420 (1980) and references therein.
2. W. E. Spicer, J. A. Silberman, P. Morgen, I. Lindau, J. A. Wilson, J. Vac. Sci. Technol., 21, 149 (1982).
3. H. M. Nitz, O. Ganschow, U. Kaiser, L. Wiedmann and A. Benninghoven, Surf. Sci. 104, 365 (1981).
4. J. A. Silberman, P. Morgen, I. Lindau, W. E. Spicer and J. A. Wilson, J. Vac. Sci. Technol. 21, 154 (1982) and references therein.
5. P. M. Raccah, U. Lee, J. A. Silberman, W. E. Spicer and J. A. Wilson J. Appl. Phys. in press.
6. P. M. Raccah, these proceedings, J. Vac. Sci. and Technol. in press.
7. G. D. Davis, N. E. Byer, R. R. Daniels, and G. Margaritondo, these proceedings, J. Vac. Sci. and Technol. in press.
8. H. F. Schaake, J. H. Tregilgas, A. J. Lewis, and P. M. Everet, these proceedings, J. Vac. Sci. Technol. in press.
9. J. A. Silberman, D. Laser, I. Lindau, J. Wilson, and W. E. Spicer, to be published.
10. R. F. C. Farrow, G. R. Jones, G. M. Williams, P. W. Sullivan, W. J. O Boyle and J. T. M. Wotherspoon, J. Phys. D 12, L117 (1979).
11. W. A. Harrison, these proceedings, J. Vac. Sci. Technol., in press.
12. M. Brown and A. F. W. Willoughby, J. Crystal Growth 59, 27 (1982) and reference therein.
13. G. Nimtz and B. Schlicht and R. Dornhaus, Appl Phys. Lett. 34, 490 (1979).
14. W. F. H. Micklethwaite and R. F. Redden, Apl. Phys. Lett. 36, 379 (1980).

15. S. Cole, these proceedings, J. Vac. Sci. and Tehnol., in press.

16. W. E. Spicer, Chap. 7 in Nondestructive Evaluation of Materials and Devices, Ed. by J. N. Zemel, NATO Advanced Study Institute Series B: Phys. Vol. 46, Plenum Press, N. Y., (1979).

17. W. E. Spicer, J. A. Silberman, P. Morgen, I. Lindau, J. A. Wilson, A.-B. Chen and A. Sher, Phys. Rev. Lett. 49, 948 (1982).

18. A.-B. Chen, A. Sher, and W. E. Spicer, these proceedings, J. Vac. Sci. Technol. in press.

19. A. Kisiel and P. M. Lee, J. Phys. Metal Phys 2, 395 (1972) and references therein.

20. W. E. Spicer, J. A. Silberman, P. Morgen, I. Lindau, and J. A. Wilson, J. Vac. Sci. Technol. 21, 142 (1981).

21. A.-Ban Chen and Arden Sher, J. Vac. Sci. Technol. 21, 138 (1982).

22. H. Ehrenreich and K. C. Hass, J. Vac. Sci. Technol. 21, 133 (1982); K. C. Hass, H. Ehrenreich and B. Velicky, Phys. Rev. B 27, 1088 (1983). K. C. Hass and H. Ehreneich, this proceedings, J. Vac. Sci. Technol. in press.

23. J. A. Silberman, D. Laser, P. Morgen, I. Lindau, and W. E. Spicer, these proceedings., J. Vac. Sci. and Technol in press.

24. W. E. Spicer, P. Pianetta, I. Lindau, and P. W. Chye, J. Vac. Sci. Technol. 14, 884 (1977); G. P. Schwartz, C. D. Thurmond, G. W. Kammlott and B. Schwartz, J. Vac. Sci. Technol. 17, 958 (1980 and ref. therein).

25. D. R. Rhiger and R. E. Kvass, these proceedings, J. Vac. Sci. Technol. in press.

26. H. H. Weider, J. Vac. Sci. Technol. 17, 1009 (1980); L. J. Messick and D. L. Lile, Internation Elec. Devices Meeting, 1981, Technical Digest IEEE, (1981). pa. 108 and ref. therein.

27. J. A. Wilson, V. A. Cotton, J. A. Silberman, D. Laser, W. E. Spicer and P. Morgen, these proceedings, J. Vac. Sci. Technol. in press

28. B. K. Janousek, R. C. Carscallen and P. A. Bertrand, these proceedings J. Vac. Sci. Technol. in press.

29. U. Kaiser, P. Sander, O. Ganschow, L. Wiedmann, A. Benninghoven, H. Maier and J. Ziegler, these proceedings, J. Vac. Sci. and Technol. in press.

30. M. Seelman-Eggebert, G. Brant, and H. J. Richter, these proceedings, J. Vac. Sci. and Technol.

Figure Captions

Figure 1 Schematic density of states and E vs k diagrams for $Hg_{1-x}Cd_xTe$. The density of states diagrams show the downward movement of the conduction band minimum (CBM) with increased Hg content. This is due to the increasing admixture of Hg 6s wavefunction to this band. (The atomic Hg $6s^2$ state lies 1.4 eV lower than the Cd $5s^2$ valence state.) The band moves monatonically because of the low m*, the long electron wavelength, and the large width of this part of the band. The situation is just the opposite for the portion of the valence band lying 4-6 eV below the valence band maximum (VBM) which also contains a large cation valence s state admixture. This portion of the valence band is characterized by short wavelength, high mass and narrow width. As a result, rather than moving monotonically as the composition is changed, it tends to break into distinct Cd 5s and Hg 6s derived peaks.

Figure 2 Photoemission spectra from $Hg_{1-x}Cd_xTe$ crystals with four different compositions. The vertical lines show the approximate positions of the Cd and Hg s-derived states (see Fig. 1). Note that, whereas, the p-derived valence band is not strongly affected by the alloy compositions the "s-derived" valence band states changes strikingly.

Figure 3 Comparison of two theoretical calculations with experiment for the "cation s-derived" valence band states (-4 to -6 eV in Fig 1 and 2). The Virtual Crystal Approximation which used an average potential disagrees strongly with experiment; whereas, the coherent potential approximation, which takes the potential

on each atom into account, gives good agreement.

Figure 4 The valence band (VBM to -6 eV) and cation d bands (-6 to -12 eV) for $Hg_{1-x}Cd_xTe$ for five values of x. Note the abrupt upward shift of the Hg 5d levels as one goes from HgTe to the alloy; likewise, notice the downward shift of the Cd 5d's in going from CdTe to the alloy.

TABLE CAPTIONS

TABLE I. Studies of Hg outflow from $Hg_{1-x}Cd_xTe$ into UHV by two groups

TABLE II. Important Characteristics of Passivation Layers Presently in Use

SCHEMATIC $Hg_{1-x}Cd_xTe$ BAND STRUCTURE

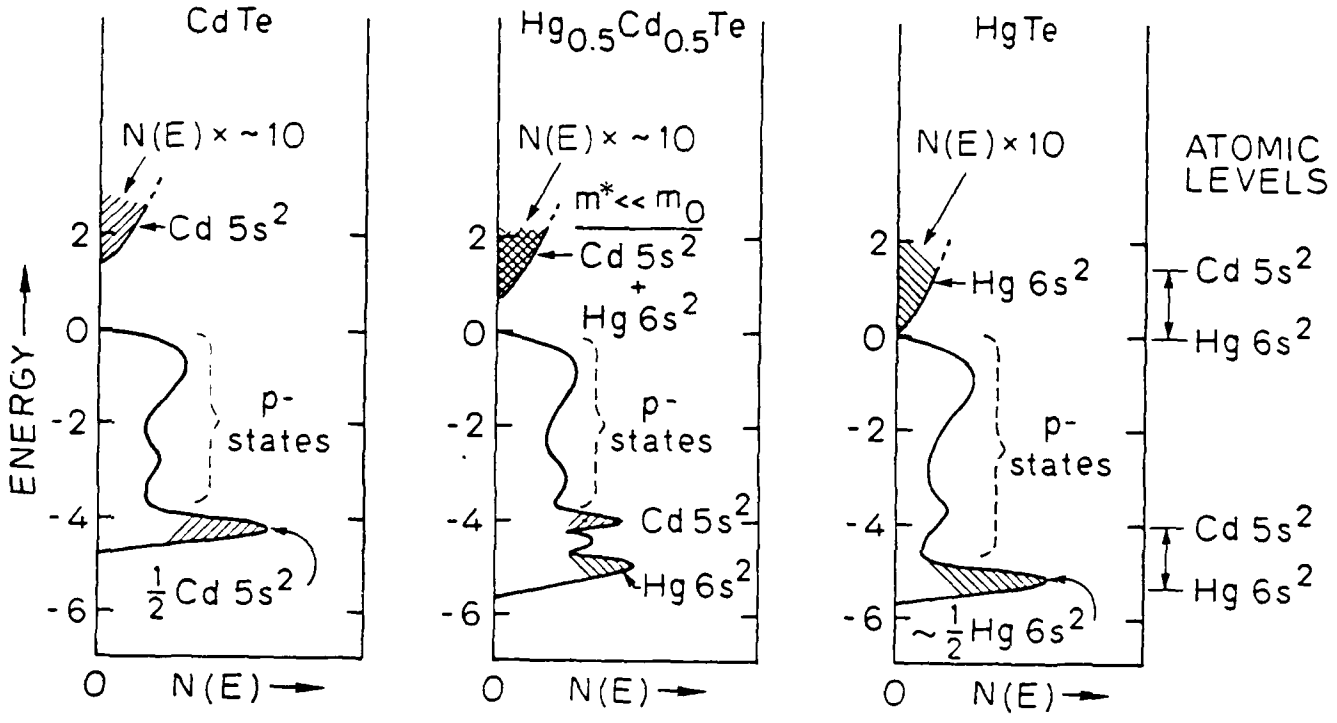

DENSITY OF STATES

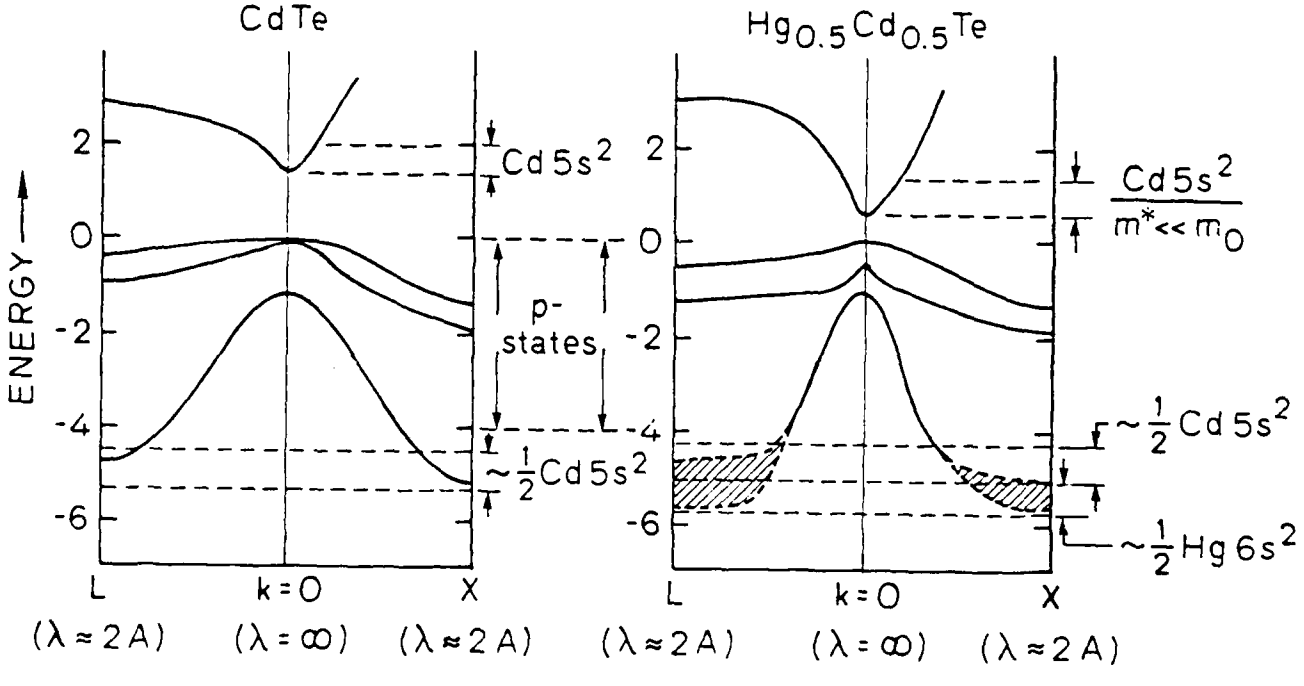

Figure 1

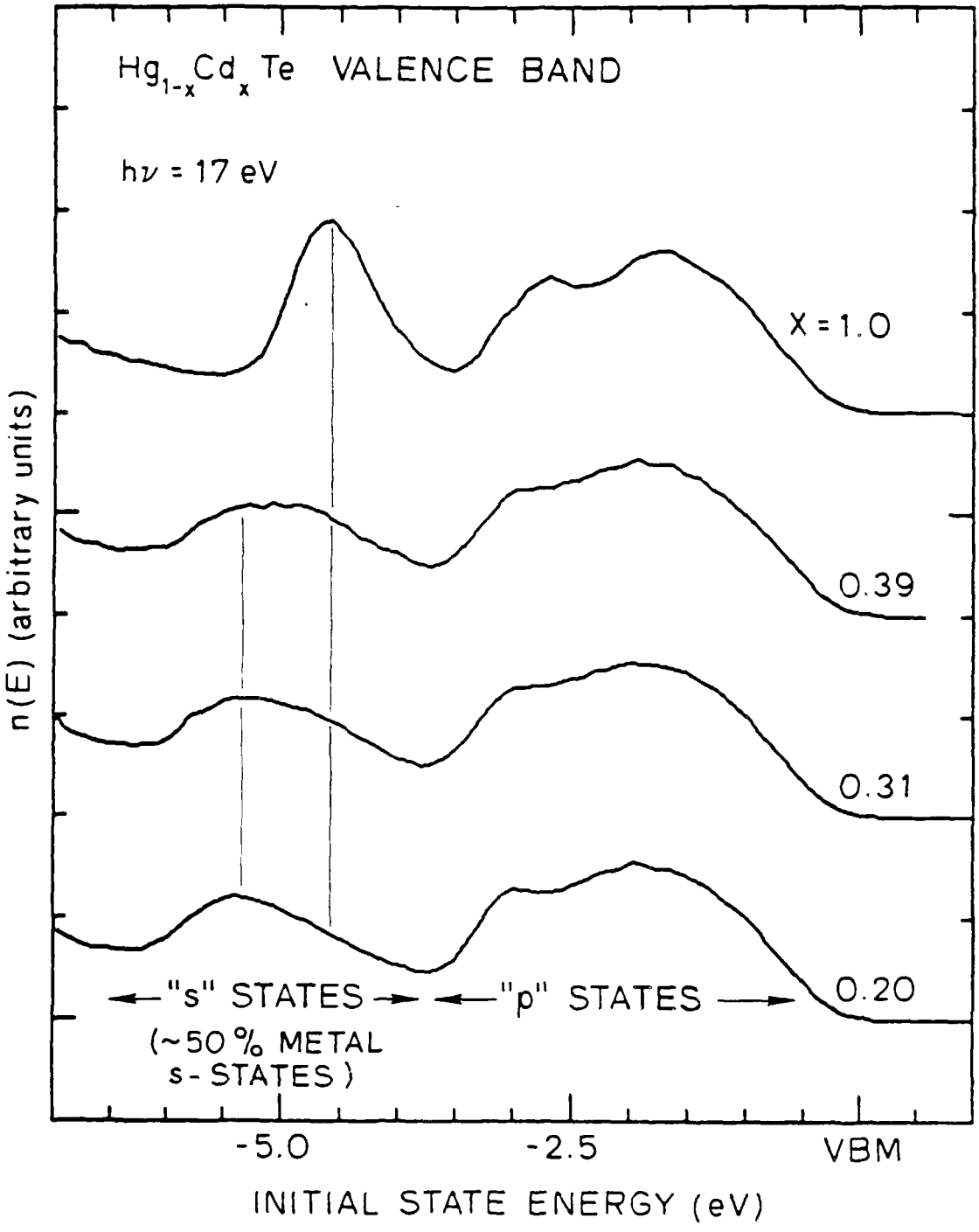
Hg1-xCdxTe VALENCE BAND
hν = 17 eV
X = 1.0
0.39
0.31
0.20
n(E) (arbitrary units)
"s" STATES
"p" STATES
(~50% METAL
s-STATES)
-5.0
-2.5
VBM
INITIAL STATE ENERGY (eV)

Figure 2

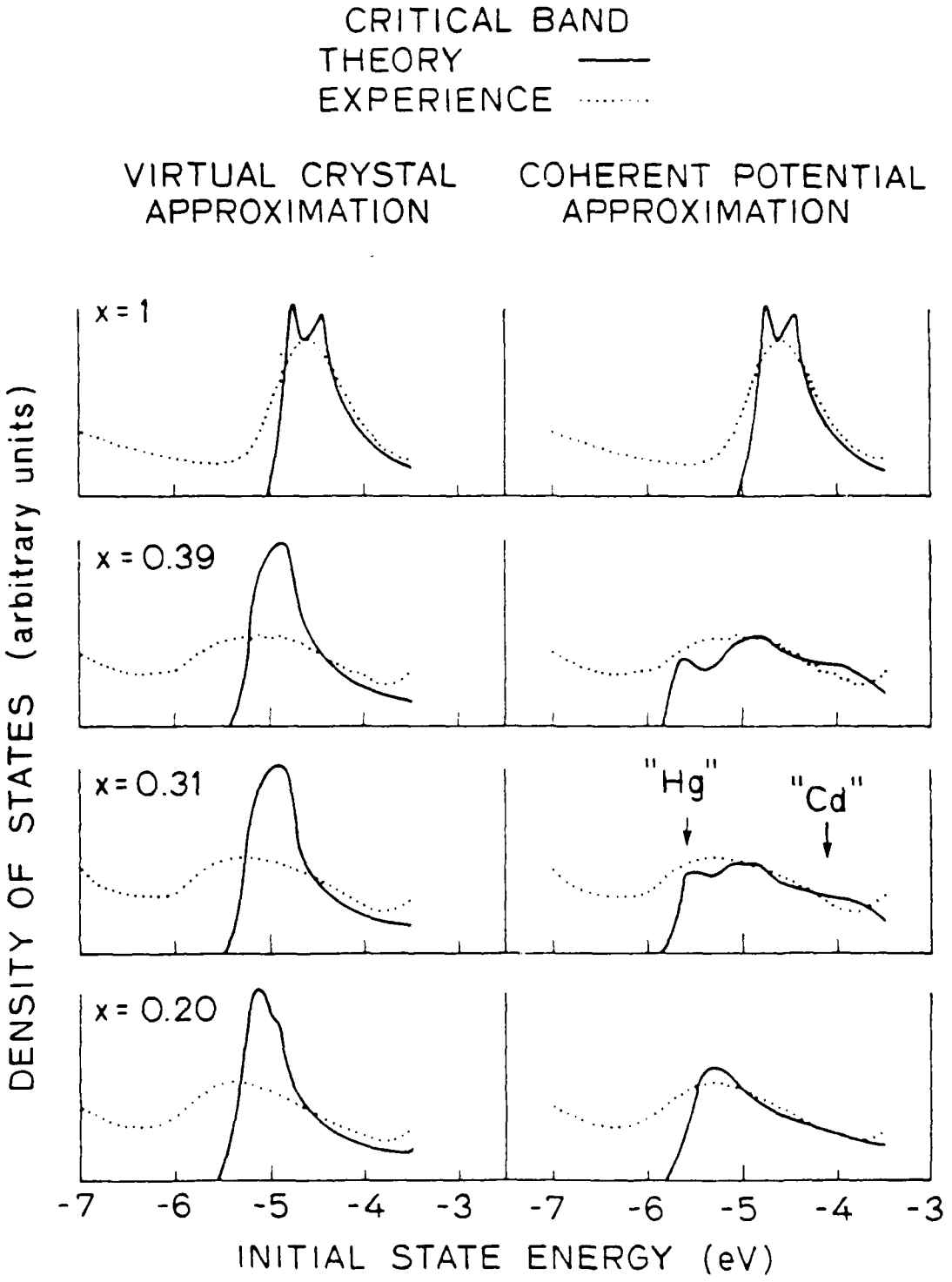
CRITICAL BAND
THEORY
EXPERIENCE
VIRTUAL CRYSTAL APPROXIMATION
COHERENT POTENTIAL APPROXIMATION
x = 1
x = 0.39
x = 0.31
x = 0.20
"Hg"
"Cd"
DENSITY OF STATES (arbitrary units)
-7
-6
-5
-4
-3
INITIAL STATE ENERGY (eV)

Figure 3

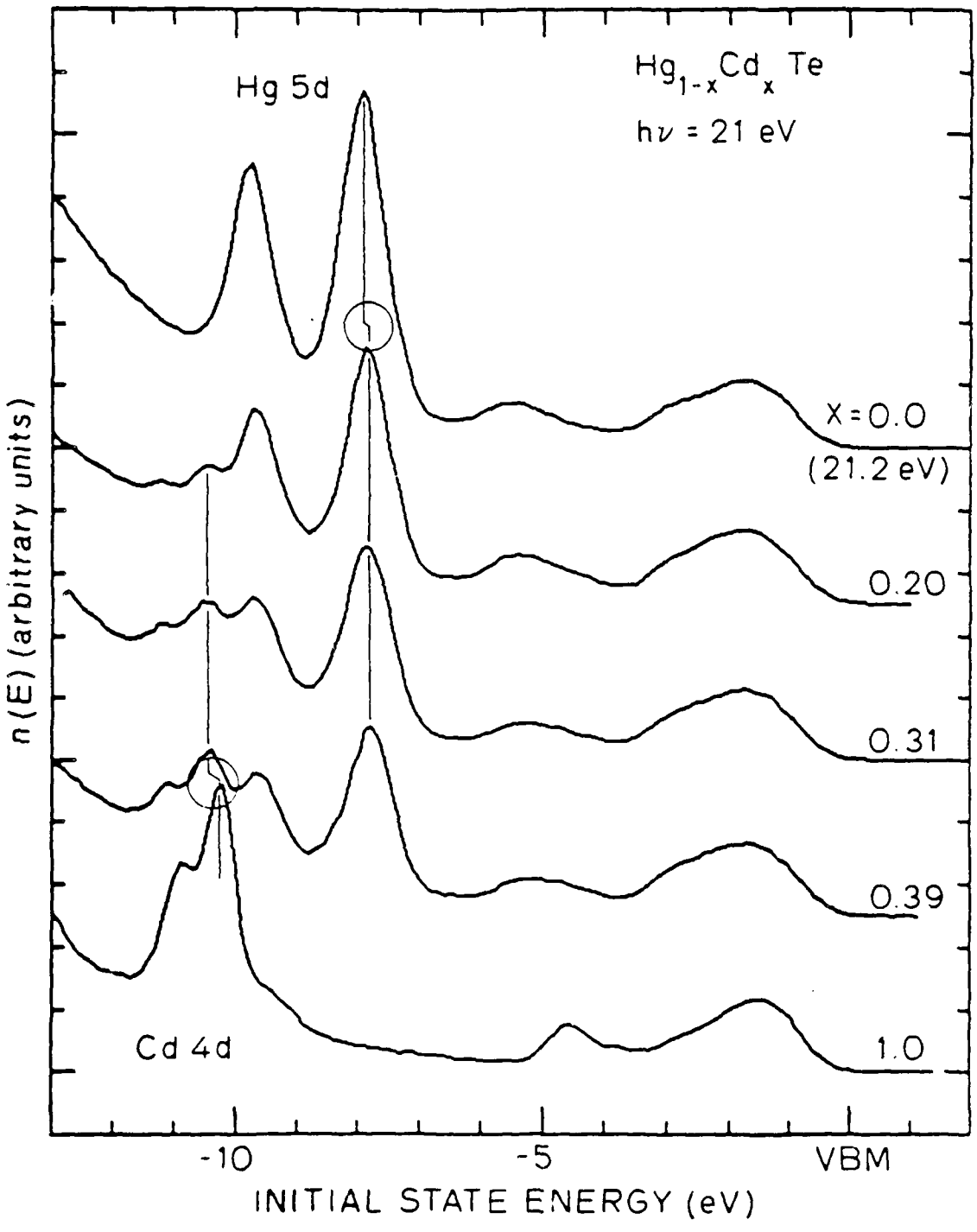
Hg 5d
$Hg_{1-x}Cd_x$ Te
hν = 21 eV
X = 0.0
(21.2 eV)
0.20
0.31
0.39
1.0
Cd 4d
n(E) (arbitrary units)
-10
-5
VBM
INITIAL STATE ENERGY (eV)

Figure 4

Section II-3

Structural and Defect Studies of Mercury Cadmium Telluride

I. Introduction

Recently it has become evident that detailed structural characterization of MCT materials is an essential prerequisite to future improvements in devices. Of particular importance are dislocations, which can move easily in MCT even at room temperature (Cole et al [1]) and are present in large numbers in the as-grown crystals.

Transmission electron microscopy (TEM) is probably the most useful technique for direct visualization of the defect structure of crystalline solids. However, the extreme fragility and ease of deformation of MCT makes such studies extremely difficult. For this reason, only relatively few TEM experiments on MCT have been reported. In this project the feasibility of the technique has been investigated.

The present experiments have addressed a number of areas of considerable current importance. These include characterization of the defects associated with etch pits produced by a defect etchant, examination of the structure of an MCT layer grown on CdTe by LPE, and investigation of the microstructure of a cleaved surface. This last topic is of considerable importance to the photoemission studies of the group.

Sample Preparation

Much effort has been devoted to the development of a reliable sample preparation technique. In view of the fragility of MCT, it was considered desirable to make samples in the form of 3mm. diameter discs, wherein the thin area (~ several hundred Angstroms for electron transmission) is produced at the center and is protected by the surrounding

relatively thick (~ 150 μm) material. The methods considered were chemical jet thinning and ion beam milling, both of which have been employed with success on other semiconductors. However, as described in the next section, ion milling was found to produce damage in the form of small point defect clusters (dislocation loops.) Chemical thinning was, therefore, adopted as the standard technique, ion milling being avoided wherever possible. In certain cases, brief periods of ion milling have been employed to remove residual surface contamination from chemically thinned samples.

The procedure used is designed to avoid the introduction of damage into the crystal. As-cut slices are reduced to the required 150 μm thickness by chemical polishing on a pad soaked in 5% Br_2/1:1 methanol: propylene glycol, which leaves a defect-free surface. 3mm. discs are obtained by masking appropriate regions with a lacquer and dissolving away the unmasked material. Final thinning is achieved by means of a 0.5mm. diameter jet of 2% Br_2:18% methanol: 80% ethylene glycol, which impinges on one face of the sample, producing a shallow dish, eventually perforating near the center. During this stage, the sample is embedded in wax which supports the thin area.

Effects of ion milling and electron beam heating

A number of slices of MCT ($x \approx 0.3$) cut from an ingot grown by the cast recrystallize (CR) process were provided by SBRC. TEM samples were prepared from these by the jet thinning process described earlier. Examination in the electron microscope revealed in general a low density of randomly distributed dislocations ($<10^5 cm^{-2}$). In a few areas, dislocation networks were observed, which were probably sub-grain boundaries. Figure 1 shows one such network.

These samples were then ion milled for 50 minutes using 4 keV. Ar+ ions at an incident angle of 18° and an estimated beam current density of 14 μ A. mm^{-2}. During this procedure, they were cooled to ~ 100 K to minimize heating effects. A typical micrograph obtained after ion milling is shown in Figure 2. The network of dislocations is similar both in frequency of occurrence and detailed arrangement to those observed prior to ion milling and was probably present initially. Also in evidence, however, are a large number of dislocation loops (up to 500 Å diameter) which are clearly a result of the ion bombardment. Similar experiments on CdTe revealed ion milling damage in this material too, although under identical conditions of ion energy and beam current the size of the loops produced in CdTe is smaller than that in MCT.

That ion bombardment produces damage of this sort in many crystalline materials is well known. What is surprising is the extent of the damage observed under such relatively gentle milling conditions. Although there is no comparable work on MCT, other workers have observed damage in CdTe. Yoshiie et al. [2] reported large densities of loops in CdTe irradiated with 1 M eV electrons in situ in the high voltage TEM. They found these loops to be interstitial in character. Yamashita [3] observes large numbers of very small extrinsic stacking faults in high resolution TEM on CdTe samples prepared by ion milling. He attributes these to very small interstitial dislocation loops.

The nature of the loops (vacancy or interstitial) in MCT has yet to be established. It seems probable that the situation would be more complex than in CdTe, since the formation of an extrinsic stacking fault in the sphalerite structure requires the presence, in equal proportions, of both the metal and Te (Figure 3). In MCT, the preferential sputtering

of Hg (Nitz et al [4]) would complicate the issue, and the nature of the resulting defects is a matter for speculation. The excess Te could appear as interstitials, antisite defects, or as fine Te precipitation on the newly formed stacking faults in the loops.

To investigate the influence of the conditions of ion energy, beam current, sample temperature, and milling time on the extent of the damage, a number of samples were milled under different conditions. Unfortunately, the results are confused by the fact that it is difficult to obtain reproducible milling conditions. The overall trends, however, are, not surprisingly, that damage is minimized by a low sample temperature, low ion energy, low beam current, and short milling times. Of course, this also minimizes the rate of removal of material. In subsequent experiments, ion milling has been used only to remove contamination from chemically thinned samples. For MCT having $x \approx 0.3$, cooled to 100K, milling at an ion energy (Ar^+) of 2 k eV and a beam current density of $3.5\mu Amm^{-2}$ for 20 minutes at an incident angle of 15° is effective in removing contamination without introducing damage. For longer times, defect clusters may be observed.

These results have important consequences for the preparation of cross-sectional samples of MCT materials, as are desirable for many applications, particularly the examination of surfaces and interfaces. The preparation technique for such samples necessitates ion milling as the primary thinning process, and this will clearly introduce large volumes of damage. This could be most confusing in the interpretation of micrographs from, for example, ion implanted material, where the dislocation loops produced by the implanted ions may be the object of study.

A further consideration is the effect of the electron beam on the sample. While no radiation damage is expected, nor has any been observed, using 120 keV electrons, the effect of heating of the sample can be important. That this is the case is illustrated in Figure 4, which shows the same area of the MCT sample shown in Figure 1, after the electron beam was condensed to a spot ~ 2 μm in diameter on the sample to obtain a convergent beam diffraction pattern. A large area of the sample appears to have melted and recrystallized. Diffraction experiments revealed that the area is still monocrystalline, although EDAX showed that the Hg content is noticeably depleted with respect to the rest of the sample. For melting to have occurred, the temperature must have risen locally to at least 700-800°C. Yamashita [3] has observed a similar phenomenon in CdTe where the temperature must therefore have reached 1100°C. However, this effect is not a regular occurrence, and must depend on the details of the geometry of the irradiated area and its thermal contact with the specimen holder. In cases where melting did not occur, monitoring of the Hg content of the irradiated region over a period of 30 minutes using EDAX revealed no measurable depletion, so it seems that the stoichiometry of the material should not be affected by electron bombardment during conventional TEM experiments.

The effect of bulk plastic deformation on the electrical properties of MCT

Experiments have been conducted to investigate the effect of large quantities of fresh dislocations, introduced by bulk plastic deformation, on the electrical behavior of MCT crystals.

Samples of CR grown MCT ($x = 0.31$), about 3 mm square and 0.5 mm thick were polished in 5% Br_2 in methanol and gold ohmic contacts applied. The thermal probe technique* was used to test the carrier type,

* Performed by Mr. T. C. Anthony of the Materials Science and Engineering Dept. at Stanford.

which was found to be p-type as expected for the as-grown material. The samples were then deformed in compression along the thin direction in an Instron machine to about 10% plastic strain, which should result in the introduction of large densities of fresh dislocations [1]. The thermal probe technique* was again used to test the carrier type, employing the original contacts, and it was found to be unaltered, i.e. p-type.

While this experiment demonstrates that grossly damaging high p-type CR MCT does not change its carrier type, it does not of course rule out more subtle changes in the electrical characteristics to which the thermal probe technique is insensitive. Currently, experiments are being conducted jointly with SBRC to study this more fully, using device quality zone melted material annealed variously to high p-type, low p-type and n-type.

Investigation of the nature of the defects associated with etch pits in CR MCT.

The use of defect etchants to reveal defects in semiconductors by means of etch pits is well established. An etchant which has been used for this purpose on MCT is 'Polisar etch 2', originally developed by Polisar et al. [5] for HgTe. It is known (Brown and Willoughby [6], Cole et al. [7]) that this etchant (composition 12 cm^3 HNO_3, 5 cm^3 HCl, 1 cm^3 CH_3COOH, 18 cm^3 H_2O, 0.02 cm^3 Br_2) produces pits at dislocations introduced by deformation. The inference is made that the defects it reveals in undeformed material are also dislocations; however, until recently, the validity of this assumption has not been investigated. James and Harper [8] have developed an etchant (a modification of the Parker and Pinnell etchant for MCT [9]) having a similar composition to that of the Polisar etch 2, which reveals defects in MCT grown by LPE on CdTe. They used TEM to characterize the defects associated with the etch pits, and reported unequivocally that they were dislocations.

In the present work, the experimental approach of James and Harper has been used to examine the defects associated with etch pits produced by Polisar etch 2 on a bulk CR MCT crystal.

A {111} oriented slice of MCT (x = 0.31) grown by the CR process by SBRC, having been chemically polished on a pad soaked in 5% Br_2 in propylene glycol to remove surface damage, was etched in Polisar etch 2 for 60 seconds. The resulting etch pit distribution is shown in Figure 5. In the central region of the slice, extending to about half the radius from the centre, the pits are randomly distributed. However, nearer the edge of the ingot the pits tend to line up in an array reminiscent of the dendrite arms in the original cast structure. In this region also are larger features which appear to be pits about 5-30 μm across having a rounded triangular shape, which lie in the regions where the smaller etch pits occur. These features are not seen in the centre of the ingot. Throughout the slice there are holes, up to 100 μm across, which pass through the whole slice and appear in similar places in adjacent ones. These too seem to be aligned in crude boundaries. They presumably are voids.

TEM samples were made from the etched material by protecting the (111) A face where the pits formed (Fewster et al. [10]) and thinning from the opposite face. Hence the thin area contained the original etch pits, and could be examined for the defects giving rise to them. Ion milling at an energy of 2 keV, a beam current density of 3.5 μ A mm^{-2} and an incident angle of 18° for one hour was necessary to remove a surface film resulting from the dislocation etchant. As expected from our previous experiments with iron milling, very light ion damage was observed over most of the crystal.

At the etch pits, the material is thinner than the surrounding crystal, so that they appear bright in a bright field micrograph. In one sample,

every etch pit was examined for defects. However, at least 50% of the etch pits appeared to be associated with no obvious large defect. It is possible that in such pits the original defect had been completely etched away. Micrographs obtained at pits where defects were present are shown in figures 6 to 11. In only two cases (eg. figure 6) did the etch pit appear to be associated with a dislocation alone. In nine pits, precipitates were found (eg. figures 7 to 11), and in only two cases was a dislocation present in addition to the precipitate (figures 7 and 8). In these cases, the precipitates lay on the dislocation line. EDAX analysis in the electron microscope on these precipitates revealed that they are rich in Te with respect to the matrix (figure 12). This suggests that they may in fact be Te precipitates, which are buried in the matrix, so that the Cd and Hg signals are non zero. Similar isolated precipitates were also found in the matrix, not associated with pits (eg. figure 13). The morphology of the precipitates associated with the dislocations was less regular than that of the isolated precipitates, which had a tetrahedral shape (compare figures 7 and 13). Certainly, these results are not as clear cut as those of James and Harper described earlier, who observed only dislocations at the pits in LPE material. In this CR material, while some pits are developed at dislocations, many occur at isolated Te precipitates, which have formed in the matrix. A number of such precipitates have been observed which were not associated with pits suggests that the pits. This suggests that the pits formed only at precipitates lying in the vicinity of the surface.

Schaake et al. [11], in TEM work on CR MCT crystals, have reported Te precipitates, both isolated and nucleated on dislocation lines, as

observed in the present work. They suggested that the precipitates nucleate during the quench from the recrystallization anneal, with the first precipitation occurring on existing dislocations, followed by formation of isolated precipitates within the matrix. The present results are not inconsistent with this hypothesis. However, the correlation of etch pits with the original cast structure leads us to suggest that the final defect structure is strongly influenced by the casting stage. During this stage, solidification would have proceeded by growth of dendrites in the outer part of the ingot, where the melt cooled most rapidly, which spread towards the center as the temperature dropped until eventually the entire ingot was solid. The dendrites are CdTe rich at the core, and the interdendritic interstices would probably be Te rich since the material is high p-type as grown. Dislocations would form in these interstices as a result of misfit between impinging dendrite arms, and Te would precipitate out, partly on the dislocations and partly in the perfect crystal. The interesting result of this work is that the subsequent recrystallization stage, whereupon the ingot is held at a temperature just below the solidus for several days, (where the Te should re-dissolve) does not appear significantly to change this structure, as shown by the etching results, even though grain growth and compositional homogenization occurs during this stage. Further work is required to gain insight into these effects.

Close examination of figures 6 and 7 reveals that the dislocation in figure 7 exhibits unusual irregular contrast along its line compared with the regular fringes visible on the dislocation in figure 6. It is interesting that the area shown in figure 6 displays much less pronounced ion damage than does that in figure 7, probably because of some masking effect by the surrounding material. A possible explanation is that the irregular

contrast in figure 7 arises from dislocation loops, introduced by ion milling, which have nucleated preferentially in the elastic strain field of the dislocation. Currently experiments are under way to study this possibility.

Defects in a layer of MCT grown on CdTe by LPE

A sample of LPE grown MCT (x=0.317) doped with As on a {111} oriented CdTe substrate was obtained from Santa Barbara Research Center. The layer thickness was 12.1 μm.

By angle lapping on a pad soaked in 5% Br_2 in propylene glycol, the epitaxial layer was progessively removed, until the CdTe substrate was exposed over about one quarter of the area of the slice, while the surface remained free of damage. TEM samples were prepared from the substrate/layer interface region and from the epitaxial layer itself using the standard technique described previously.

Figure 14 shows a micrograph of the defects in the MCT epitaxial layer, several microns from the interface with the CdTe. (More precision than this is impossible with the present technique.) The electron beam is about 5° from <111>, the normal to the interface, and the sample is $\leq$ 1000 Å thick. The defects are believed to be dislocations lying perpendicular to the interface plane (i.e. along <111>). Also visible is a 'speckling' in the background which is a result of residual surface contamination from the sample preparation. The density of the dislocations in this region (which is a representative one) is of the order of 10^7 cm^{-2}, which is consistent with the results of James and Harper [8] obtained using chemical etching on a layer grown by SBRC on a high dislocation density ($\sim 10^7 cm^{-2}$) CdTe substrate.

The arrangement of defects close to (within 1-2 μm of) the interface region itself is shown in the micrograph in figure 15. The electron beam

direction is 3° from <111>, and again the sample is < 1000 Å thick. It consists of a dense array of dislocations arranged in a hexagonal network, their lines lying predominantly along [110] directions. These dislocations certainly arise as a result of the lattice mismatch between MCT (x = 0.317) and the CdTe substrate, which is 0.2% at this composition. The <110> direction is the lowest energy configuration of a dislocation in the sphalerite structure.

Similar observations have been reported by Woolhouse et al. [12]. They stated that the misfit dislocation networks extended into the MCT layer for several microns from the interface with the CdTe. In the ideal case, the mismatch should be accommodated within one unit cell, and all the dislocations should lie in a single plane at the interface. Woolhouse et al. attributed the broadening of the interface region in the MCT/CdTe system to interdiffusion, which creates a composition gradation, so that the mismatch is accommodated over an extended region. The present micrograph gives no information on the spatial arrangement of the defects. However, it is clear that, in several regions, the dislocations form a closed hexagonal network, implying that here they lie in a single plane. Other dislocations appear to run in different directions and it seems probable that they lie out of these planes. They may be continuous either with dislocations in the substrate or with those observed in the epitaxial layer. If a is the spacing between the <110> valleys in the substrate and b, is that in the layer, it is a simple matter to show that the expected spacing between the misfit disloctions is $d = ab/(a-b)$. In this case, $a = 3.969$ Å and $b = 3.966$ Å so $d \approx 5000$ Å or 0.5 μm. This is of a similar order to that observed in figure 15(0.2 - 1.0 μm). It also agrees approximately with the spacing observed by Woolhouse et al., for layers having compositions in the range $0.2 < x < 0.4$. In view of

their statement that the misfit dislocations extend for several microns into the layer, this approximate agreement with the theoretical spacing is rather surprising. If the interface were not abrupt, but graded, then the required density of dislocations in a given volume should be correspondingly diminished, and their mean spacing would therefore be larger than the theoretical value. That this apparently is not the case in the observations of Woolhouse et al. may imply that the composition of the layer fluctuates with distance from the substrate, rather than grading continuously.

Defects at the cleaved surface of an MCT crystal

Cleaving in situ in ultra-high vacuum is a convenient method of preparing a clean surface for subsequent study. In the sphalerite structure, the principal cleavage plane is {110}, and the III-V compounds such as GaAs cleave readily at room temperature to give a very flat surface. Experience with MCT has shown that this is not generally the case, the surface being very rough. In this study, TEM has been used to investigate the nature of the cleaved surface in MCT.

The experiments were performed on a CR MCT crystal ($x = 0.35$) which had been cleaved in ultra-high vacuum during a series of photoemission experiments. An optical micrograph of the surface is shown in figure 16. The roughness of the surface is evident. In general, the cleavage plane is {110}, however, the surface is covered in numerous steps, varying considerably in size up to about 30 μm, where the propagating crack appears to have changed to a different plane and then back to the original one again. In the central region, the surface is not planar, but rounded, and here it exhibits a rough texture reminiscent of ductile failure commonly seen in metals. There appear to be discontinuities in the surface which are believed to be associated with the

long linear voids previously observed in the etching experiments described in an earlier section.

The cleaved face was protected with wax and planar TEM samples were prepared from the crystal by jet thinning from the back face. The roughness of the cleaved surface made this procedure unpredictable, and only one sample was suitable for examination. This was taken from an area where the surface was covered in planar steps.

Figure 17 shows a micrograph obtained at a distinct step in the surface where the cleavage crack changed direction for about 2 μm then returned to its original plane. Along the boundaries of the step there are dense tangles of dislocations, which are shown more clearly in the higher magnification view in figure 18. On the step itself is a particle which was too thick to transmit electrons, thereby rendering identification difficult. A number of similar particles were observed in the thin area. It is not possible to say at the present stage whether they are some surface contamination, or were present in the bulk crystal. However, from the way the edges of the step curve toward the particle, it seems probable that it was initially present and played an active role in the formation of the step. It is possible that the crack propagated until it was stopped by interaction with the particle. Since the stress for deformation of MCT at room temperature is low [1] the high stress field at the tip of the stationary crack would nucleate large densities of dislocations, which are observed. It appears th , under the influence of the particle, propagation of the crack occurs on a new plane. The crack again arrests further on, nucleating further dis - cations, then leaves the region of the particle and continues on the original plane. Clearly, this mechanism can only be confirmed by further experiments. An important implication, however, is that the

surface of a sample of MCT cleaved at room temperature must contain a large number of dislocations with respect to the bulk. Further, since plastic deformation occurs less readily at lower temperatures, cleaving below room temperature might produce higher quality cleaves having a lower density of dislocations. This is currently under investigation.

Summary

1. MCT and CdTe are subject to considerable damage, in the form of point defect clusters during ion beam milling using 2 keV Ar+ ions at a beam current density of 3.5 μAmm^{-2} for times longer than 20 minutes.

2. Electron beam irradiation in the TEM using 120 keV electrons produced no detectable change in either structure or composition (Hg content) of MCT over periods up to one hour.

3. Preliminary experiments show that the introduction of large densities of dislocations by bulk plastic deformation does not affect the carrier type of p-type MCT grown by the CR process.

4. Etch pits produced by the defect etchant 'Polisar etch 2' on the (111) A face of MCT grown by the CR process are frequently associated with isolated Te precipitates. The proportion of pits associated with dislocations is much lower.

5. The interfacial region between an MCT layer grown by LPE and its CdTe substrate contains a high density of dislocations lying along <110> directions in a predominantly hexagonal network. Over a region less than 1000 Å in thickness their mean spacing is consistent with accomodation of the lattice parameter mismatch between the two materials. The fact that this interfacial defect structure extends into the layer for several microns from the substrate creates a dilemma concerning the origin of this large number of dislocations, and leads us to the suggestion that fluctuations in composition may be responsible.

In the MCT layer away from the interface the dislocation density is about 10^6 - 10^7 cm^{-2}, these lying along <111>. That this density is similar to that expected in the CdTe substrate suggests that these defects may have propagated through from the substrate.

6. The surface of an MCT crystal cleaved at room temperature is rough and covered in numerous steps. These steps appear to be associated with large densities of dislocations where the cleavage crack presumably momentarily stopped before changing direction. This suggests that the room temperature cleaved surface is highly defectuous with respect to the bulk crystal. Cleaving at low temperature should improve the quality of the surface by inhibiting plastic deformation.

References

1. S. Cole, A. F. W. Willoughby and M. Brown, J. Cryst. Growth, 59, (1982) 370.
2. T. Yoshiie, H. Iwanaga, N Shibata, K. Suzuki, M. Ichihara and S. Takeuchi, Philos. Mag. A. 47, (1983) 315.
3. T. Yamasn ta, private communication.
4. H. M. Nitz, O. Ganschow, U. Kaiser, L. Wiedman, and A. Benninghoven, Surf. Sci. 104, (1982) 365.
5. E. L. Polisar, N. M. Boinikh, G. V. Indenbaum, A. V. Vanyukov and V. P. Schastlivii, Izv. V. U. Z. Fizika, 6, (1968) 81
6. M. Brown and A. F. W. Willoughby, J. de Physique, Colloque C6, 40 (1979) 151.
7. S. Cole, A. F. W. Willoughby and M. Brown, J. Mater. Sci. (to be published).
8. T. W. James and V. B. Harper, private communication.
9. G. Parker and J. Pinnell, J. Electrochem. Soc. 118, (1971) 1868.

10. P. F. Fewster, S. Cole, A. F. W. Willoughby and M. Brown, J. Appl. Phys. 52, (1981) 4568.

11. H. F. Schaake, J. H. Tregilgas, A. J. Lewis and P. M. Everett, paper presented to the 1983 U. S. Workshop on Physics and Chemistry of MCT, Dallas, TX.

12. G. R. Woolhouse, H. Kawayoshi and T. J. Magee, paper presented at AACG, 6th Conference on Crystal Growth, Fallen Leaf Lake, 1982.

AD-A142 342 HGCDTE SURFACE AND DEFECT STUDY PROGRAM(U) SANTA BARBARA RESEARCH CENTER GOLETA CALIF J A WILSON ET AL. JUL 83 SBRC-40497 MDA903-83-C-0108 1/2

UNCLASSIFIED F/G 20/12 NL

END
DATE FILMED
8 84
DTIC

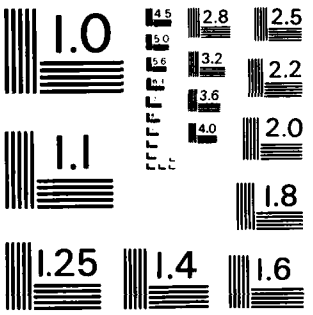

MICROCOPY RESOLUTION TEST CHART
NATIONAL BUREAU OF STANDARDS - 1963 - A

Figure Captions

Figure 1 Micrograph from a CR MCT sample prepared by chemical jet thinning, showing a subgrain boundary.

Figure 2 Micrograph from a CR MCT sample prepared by chemical jet thinning followed by ion beam milling (see text).

Figure 3 (110) projection of the sphalerite structure showing an extrinsic stacking fault.

Figure 4 Micrograph showing an area of an MCT crystal which was accidentally melted by electron bombardment in the TEM.

Figure 5 Etch pit distribution on the (111) A face of a CR MCT crystal etched in Polisar etch 2 for 60 seconds. Composite micrograph along radius of a circular slice.

Figure 6 Dislocation associated with etch pit in MCT.

Figure 7 Precipitate *nucleated* on dislocation associated with etch pit in MCT.

Figure 8 Precipitate nucleated on dislocation associated with etch pit in MCT.

Figure 9 Precipitate associated with etch pit in MCT.

Figure 10 Precipitate associated with etch pit in MCT.

Figure 11 Precipitate associated with etch pit in MCT.

Figure 12 EDAX spectra from (a) MCT matrix, (b) precipitate obtained in-situ in TEM.

Figure 13 Isolated precipitate in matrix of MCT crystal.

Figure 14 Defects in MCT epitaxial layer grown by LPE.

Figure 15 Defects in interfacial region between MCT epitaxial layer and CdTe substrate.

Figure 16 Nomarski interference contrast optical micrograph of cleaved surface of the MCT crystal. (Arrow shows direction of cleave.)

Figure 17 Micrograph of defects associated with a step in the cleaved surface of an MCT crystal.

Figure 18 Higher magnification view of Figure 17.


μm

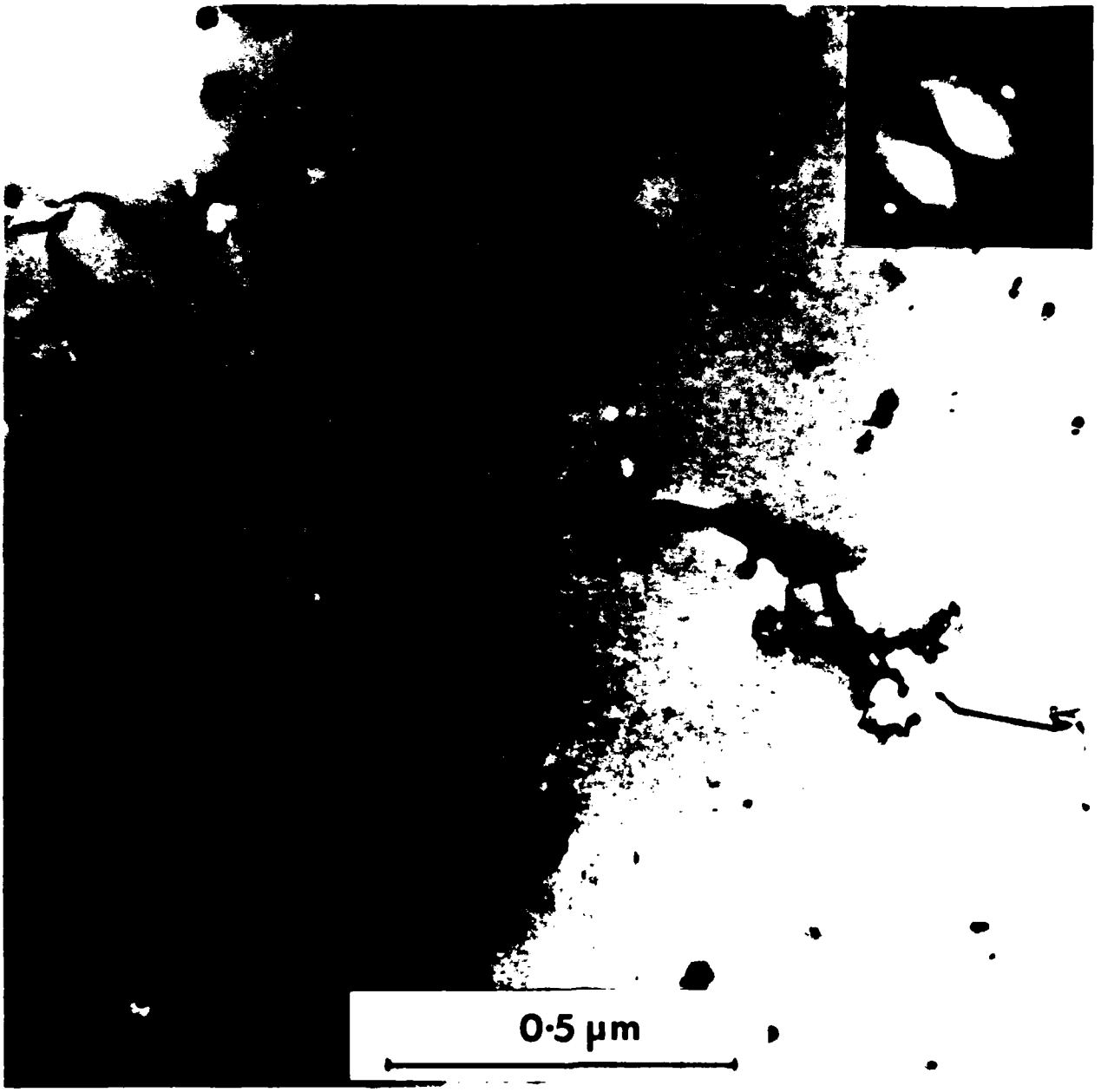
0·5 µm

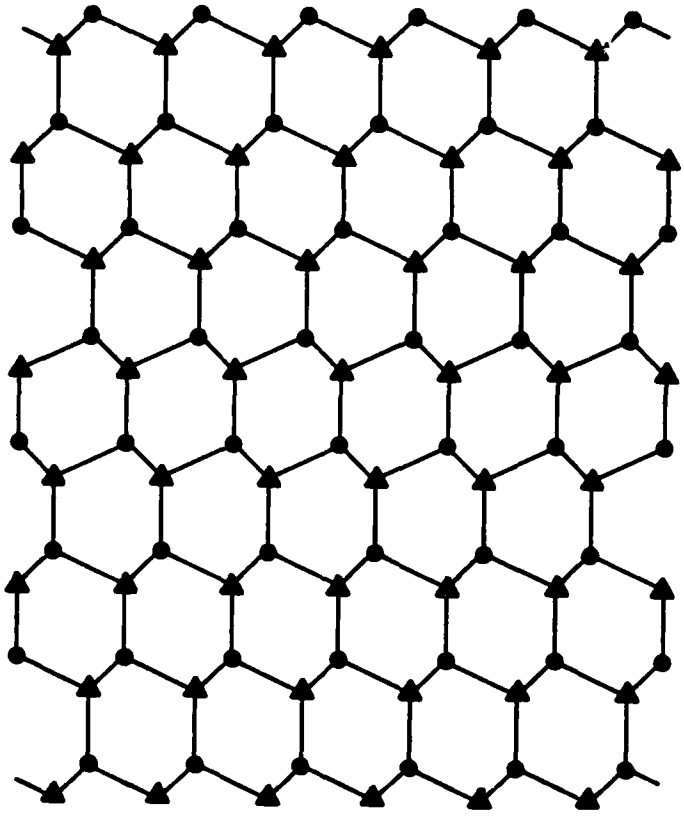

● Cd, Hg

▲ Te

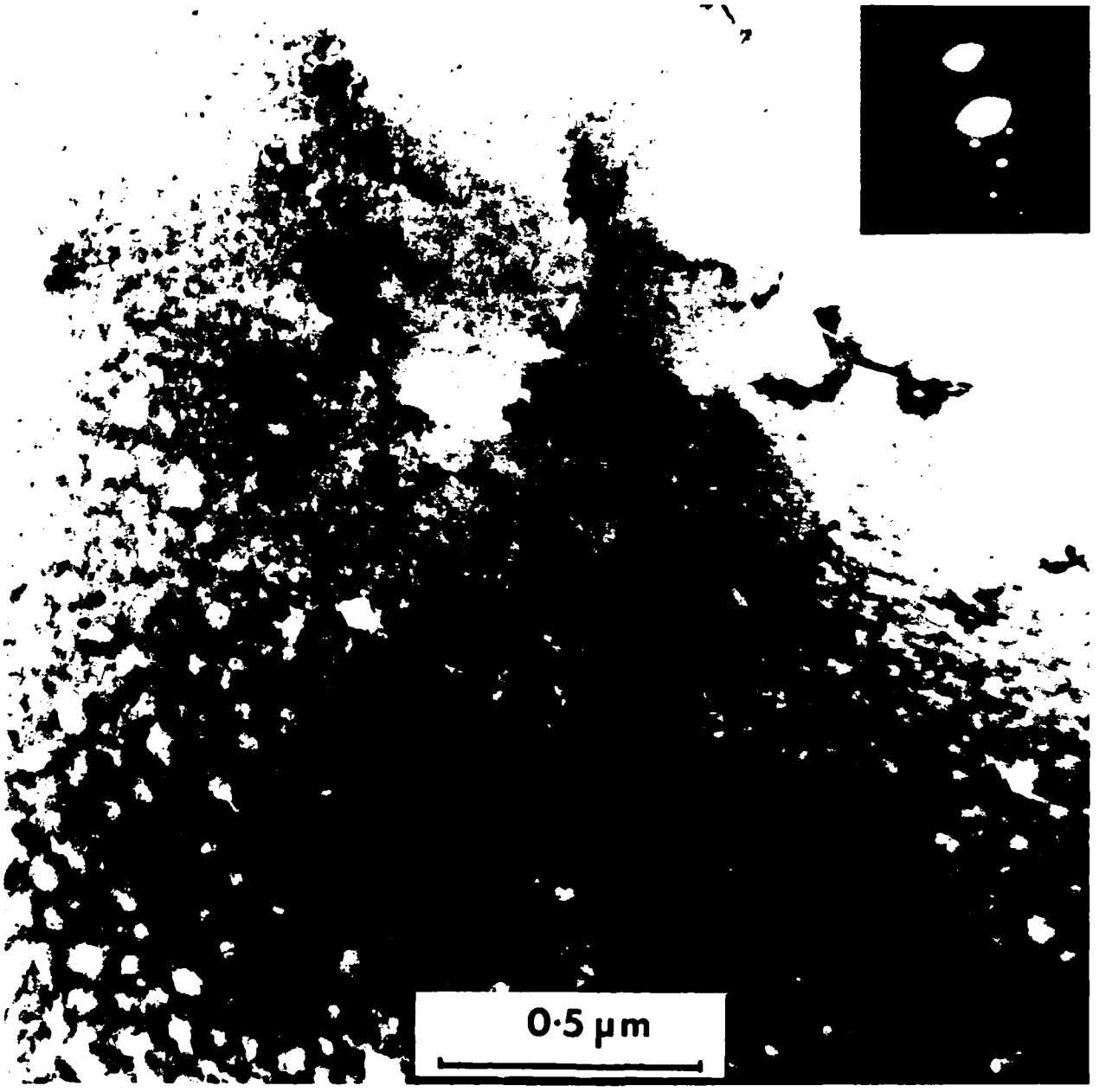
0·5 µm

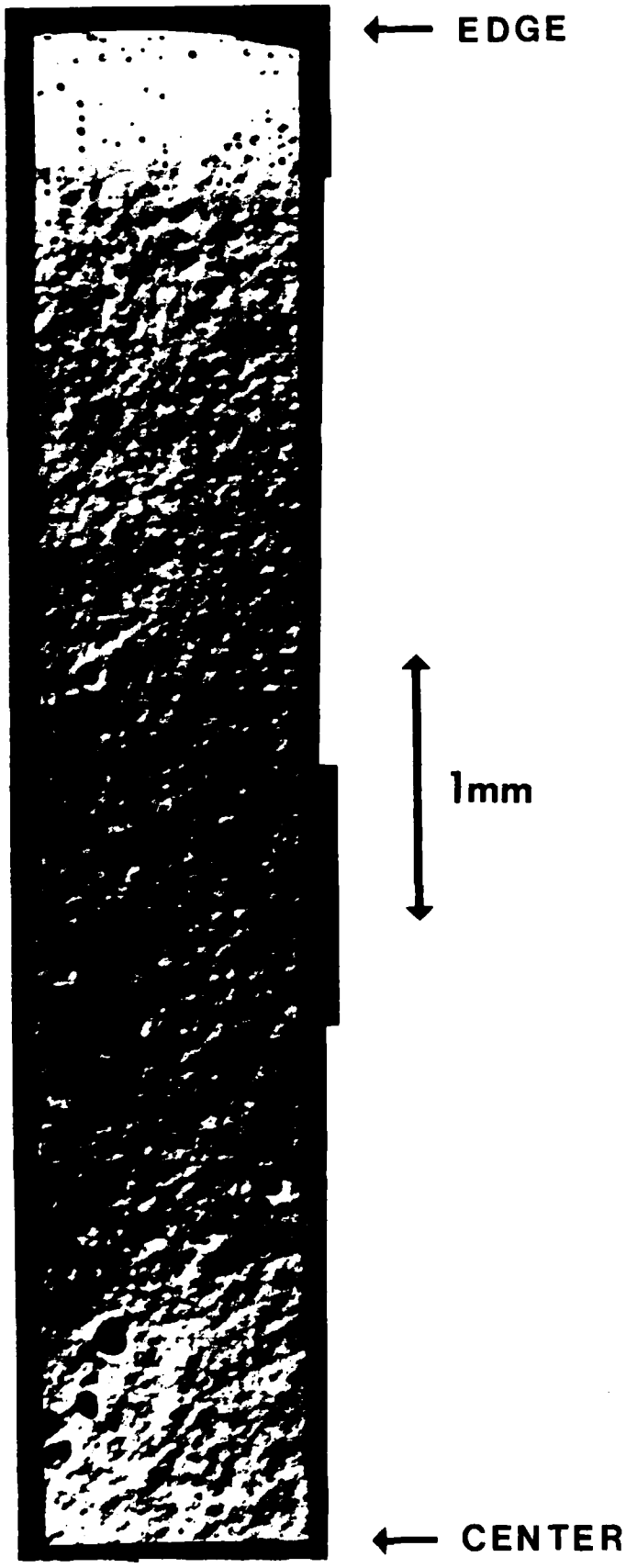
EDGE
1mm
CENTER

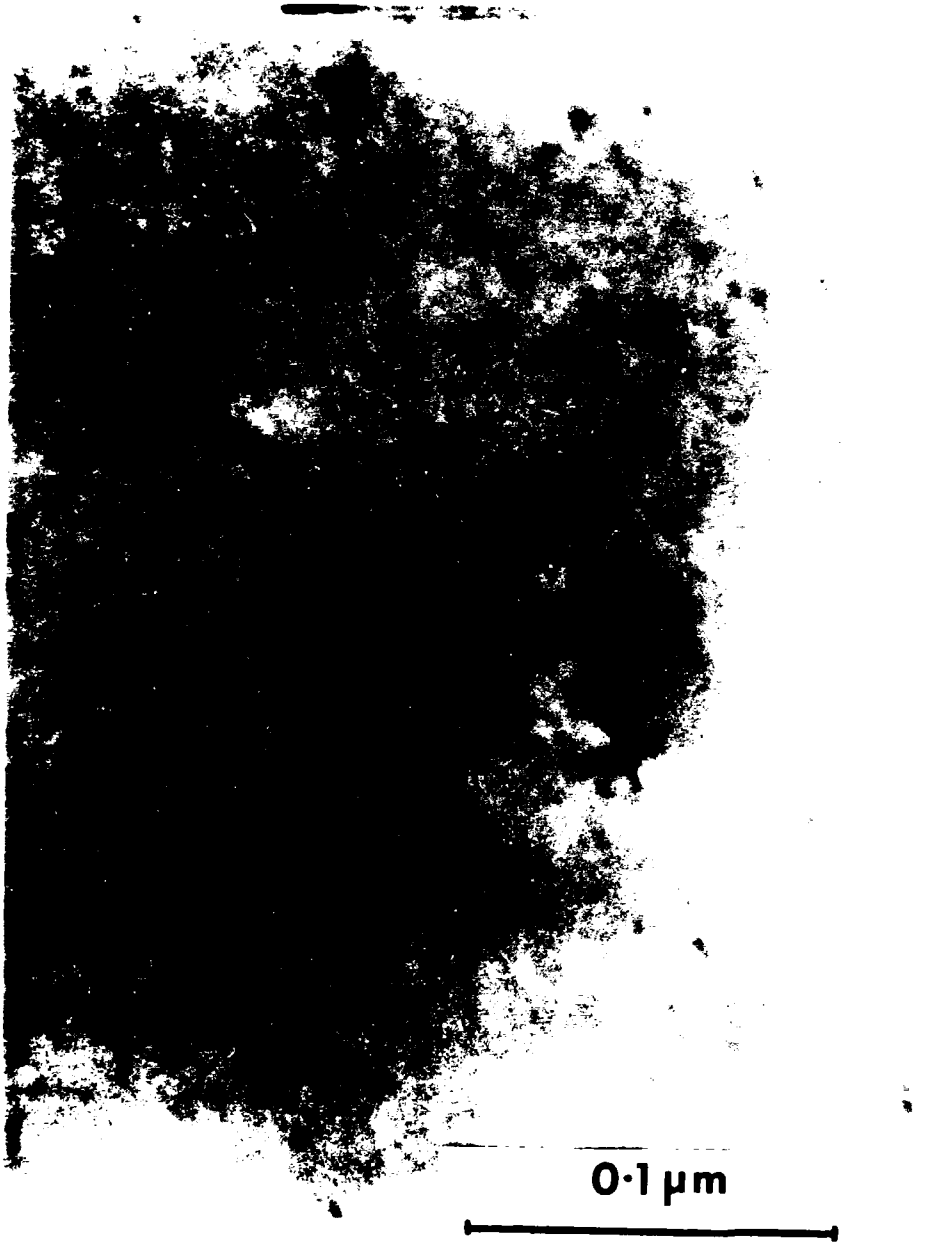
0·1 µm

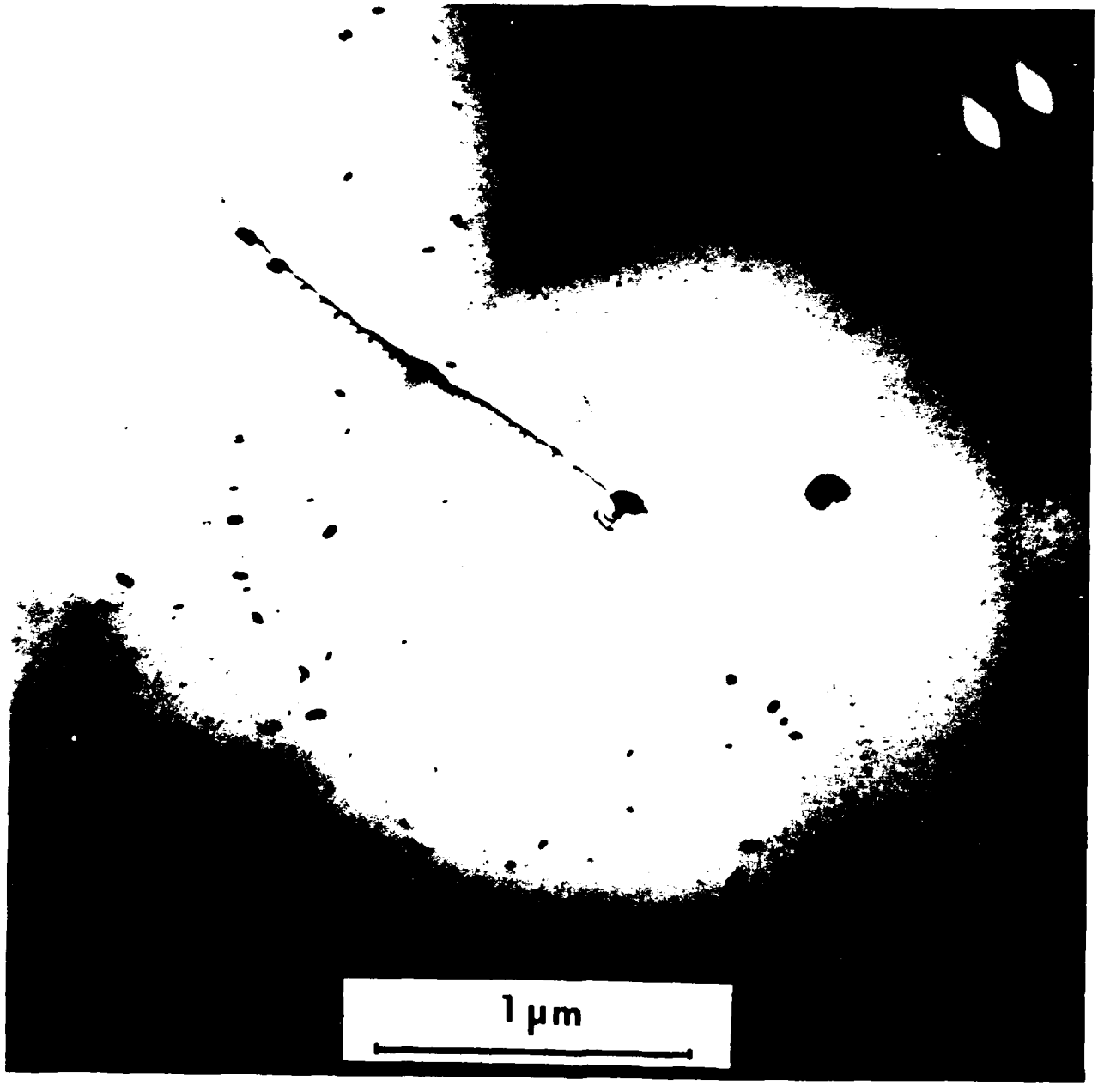
1 µm

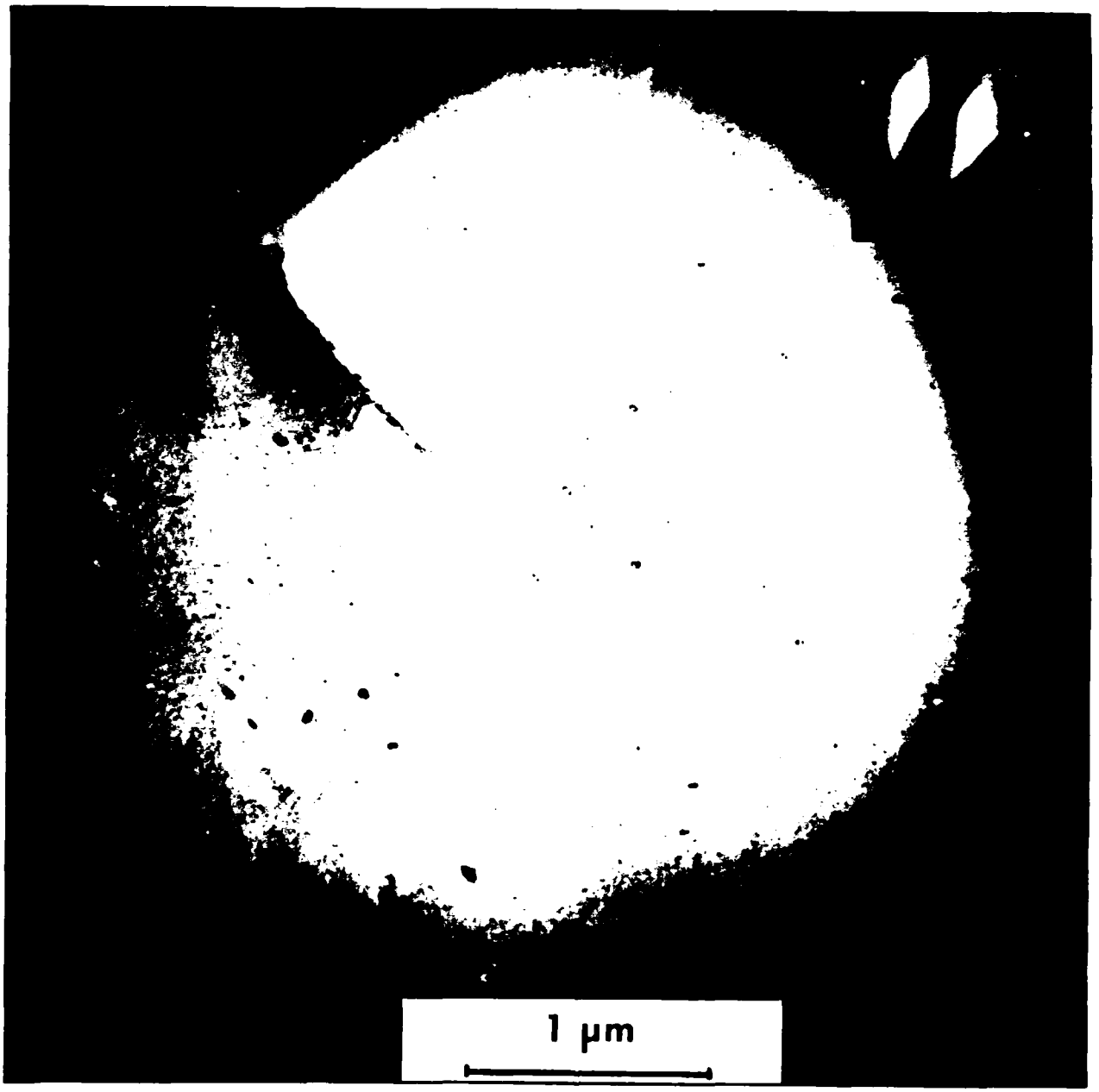
1 μm

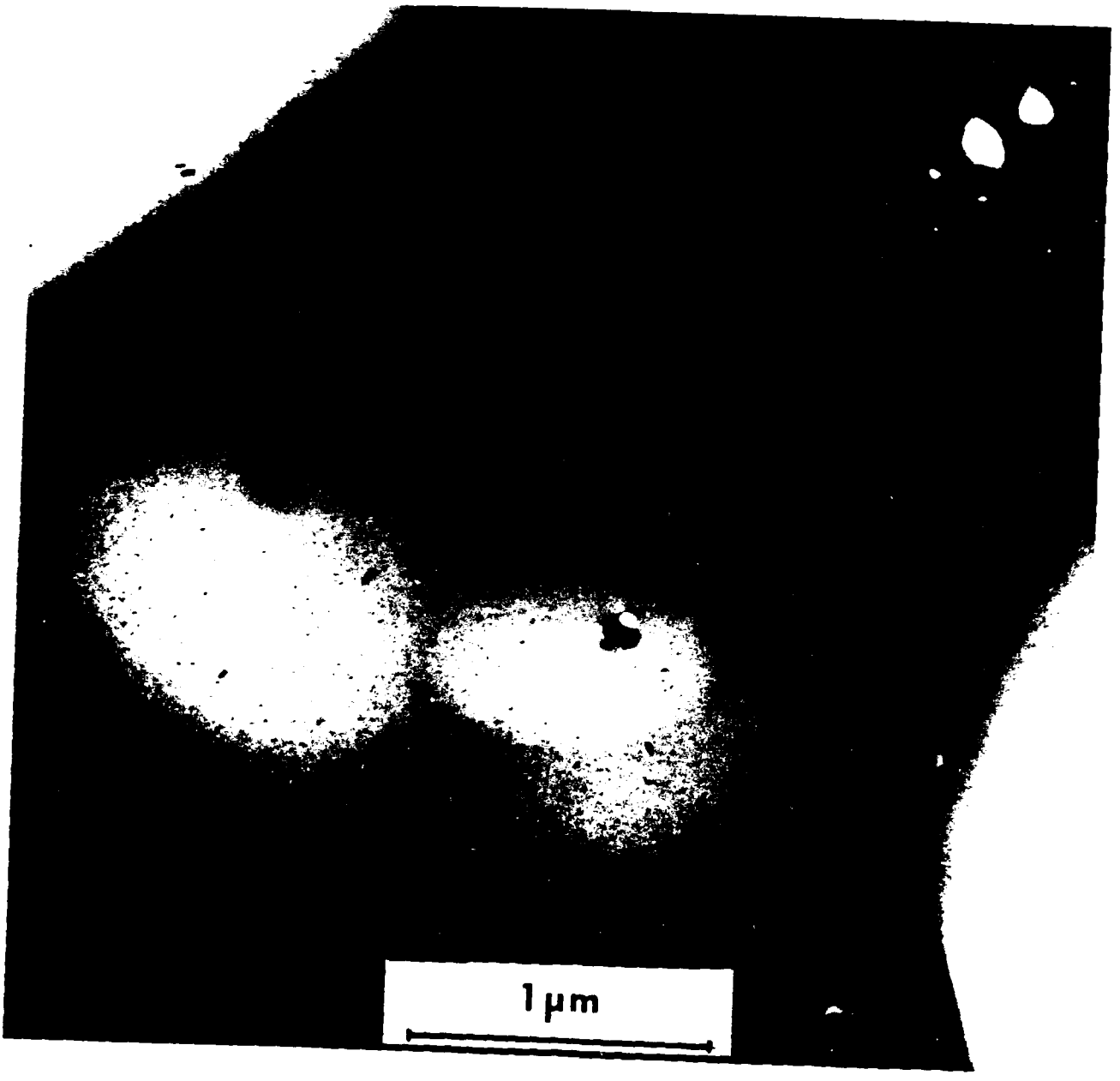
1μm

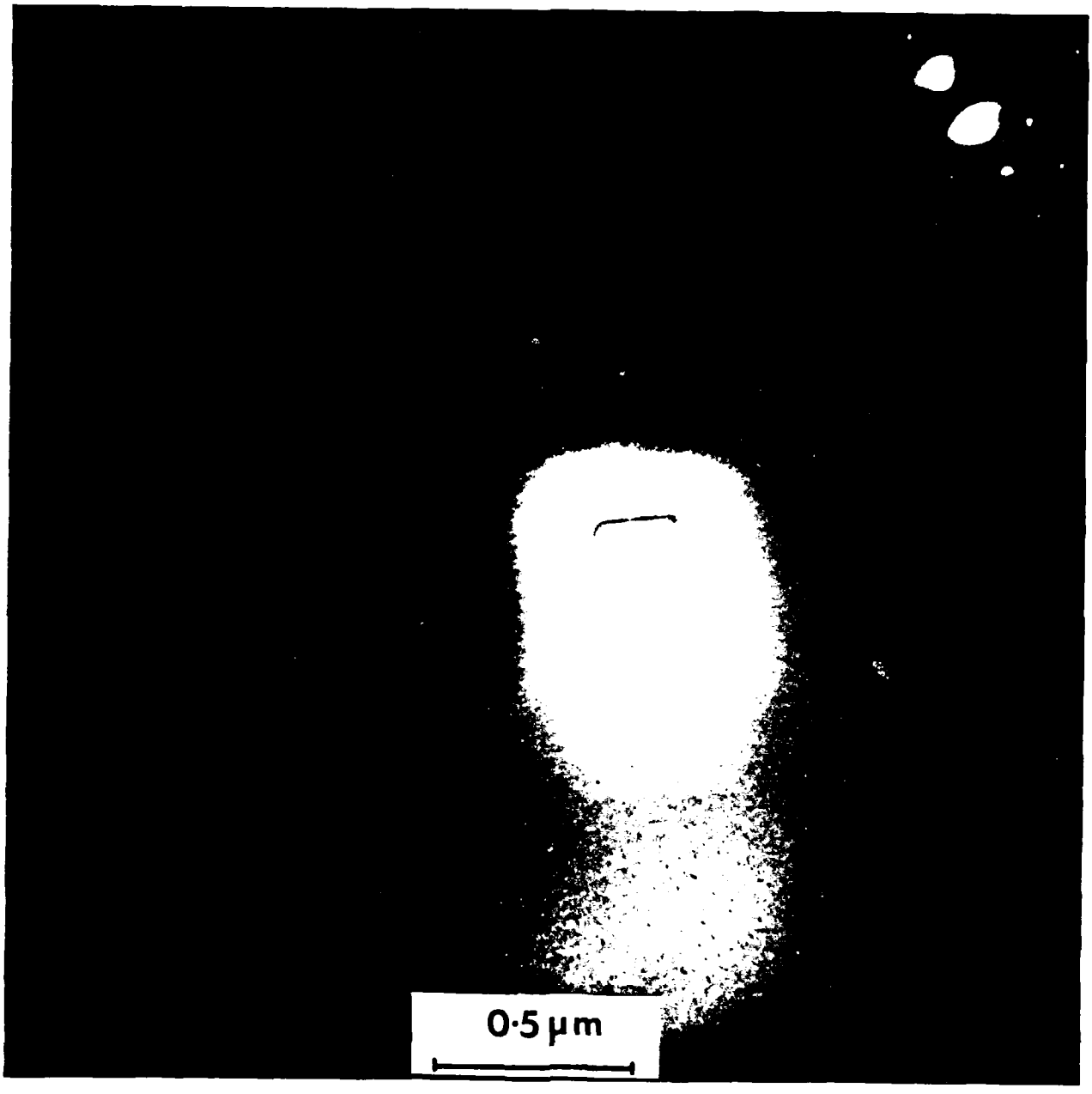
0·5 µm

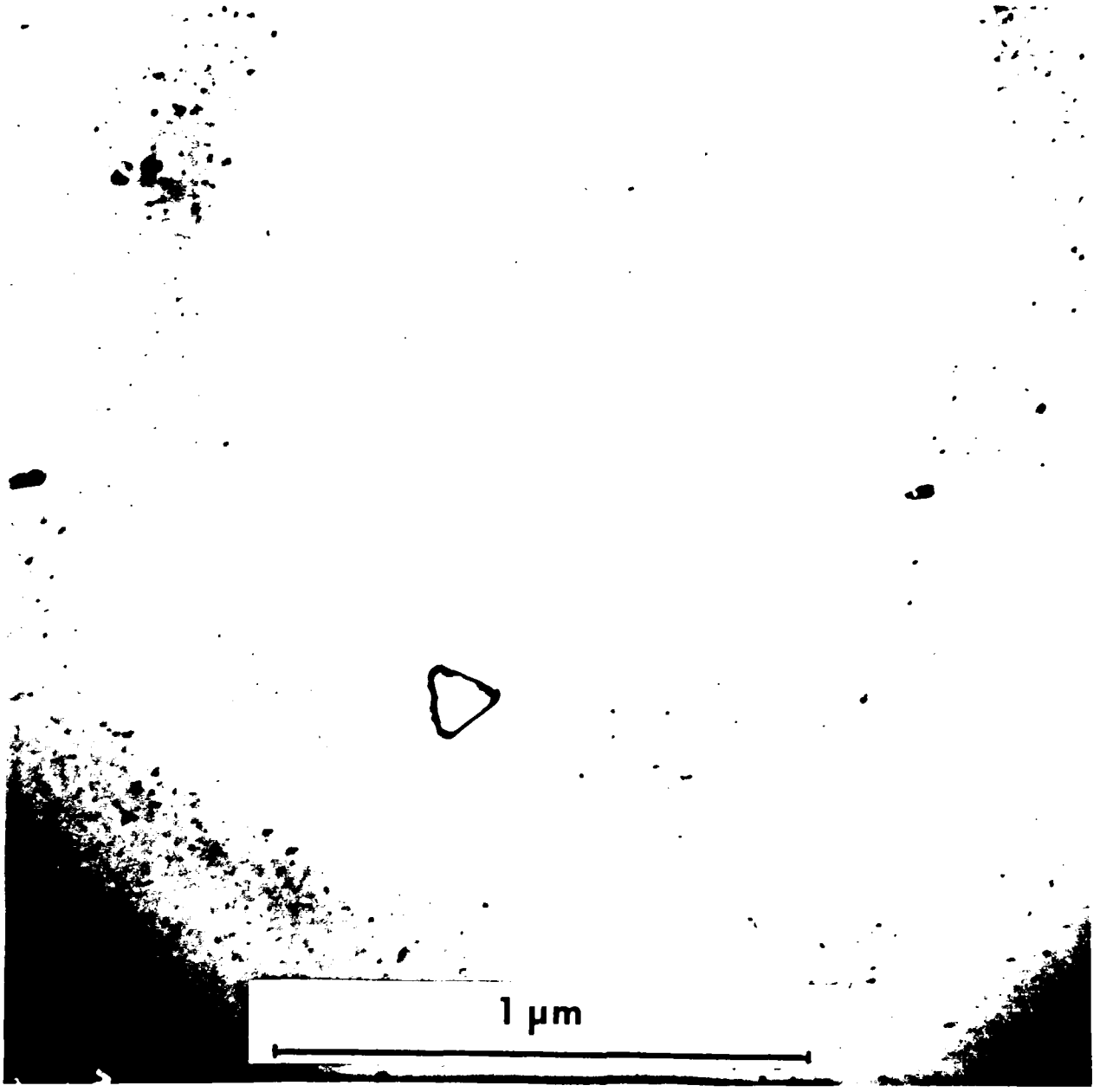
1 µm

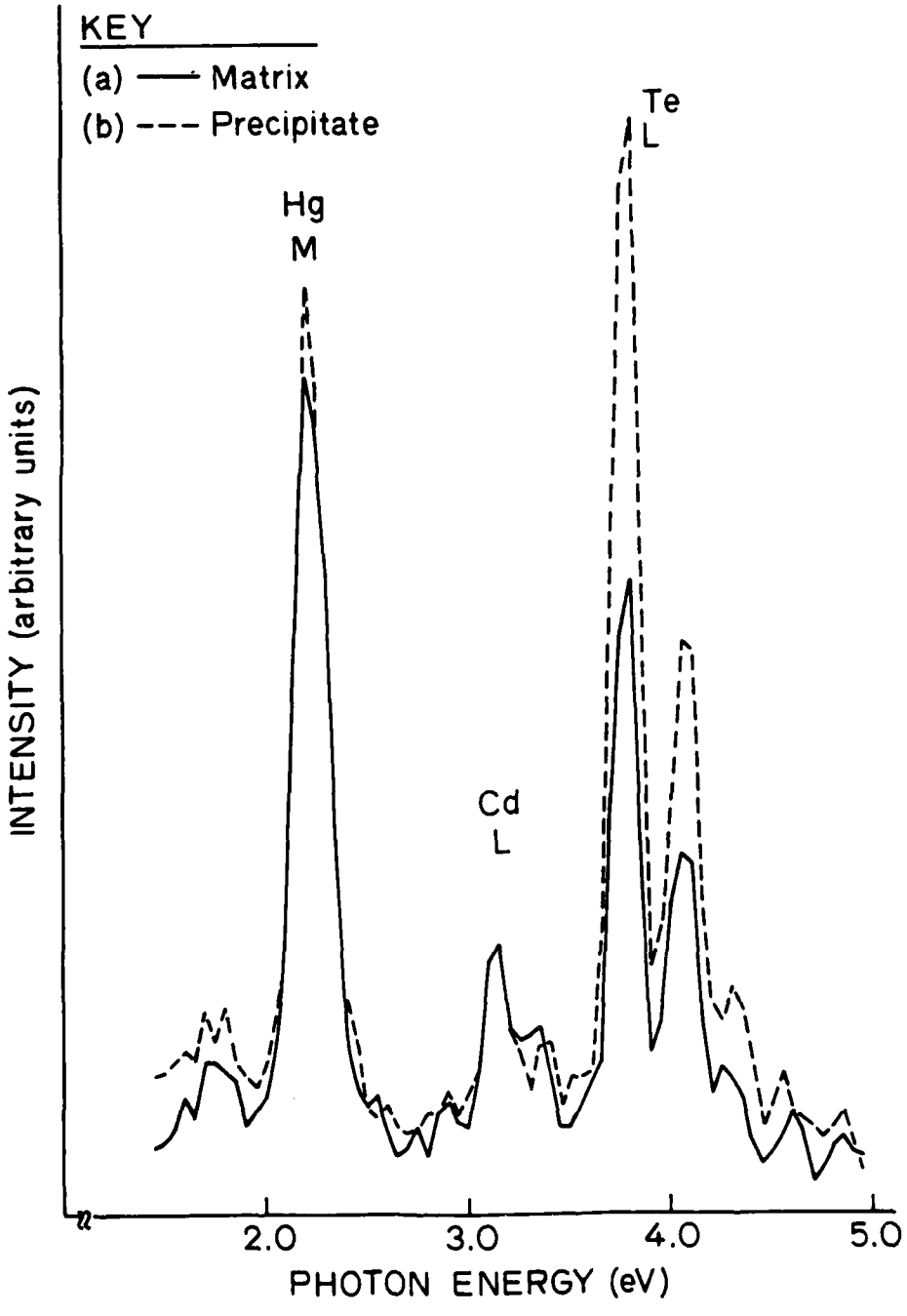
KEY
(a) —— Matrix
(b) --- Precipitate
Hg
M
Cd
L
Te
L
INTENSITY (arbitrary units)
0
2.0
3.0
4.0
5.0
PHOTON ENERGY (eV)

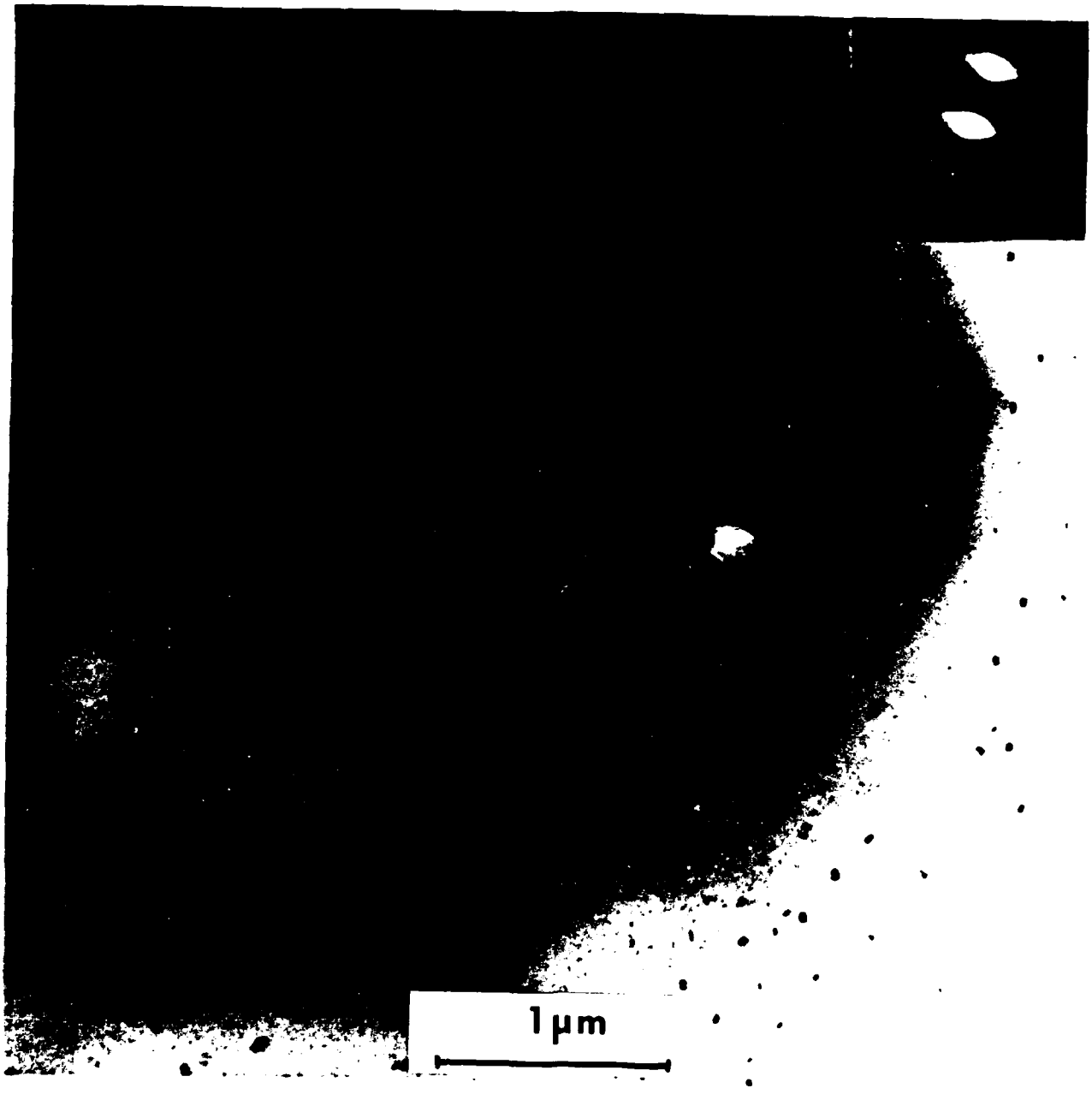
1 µm

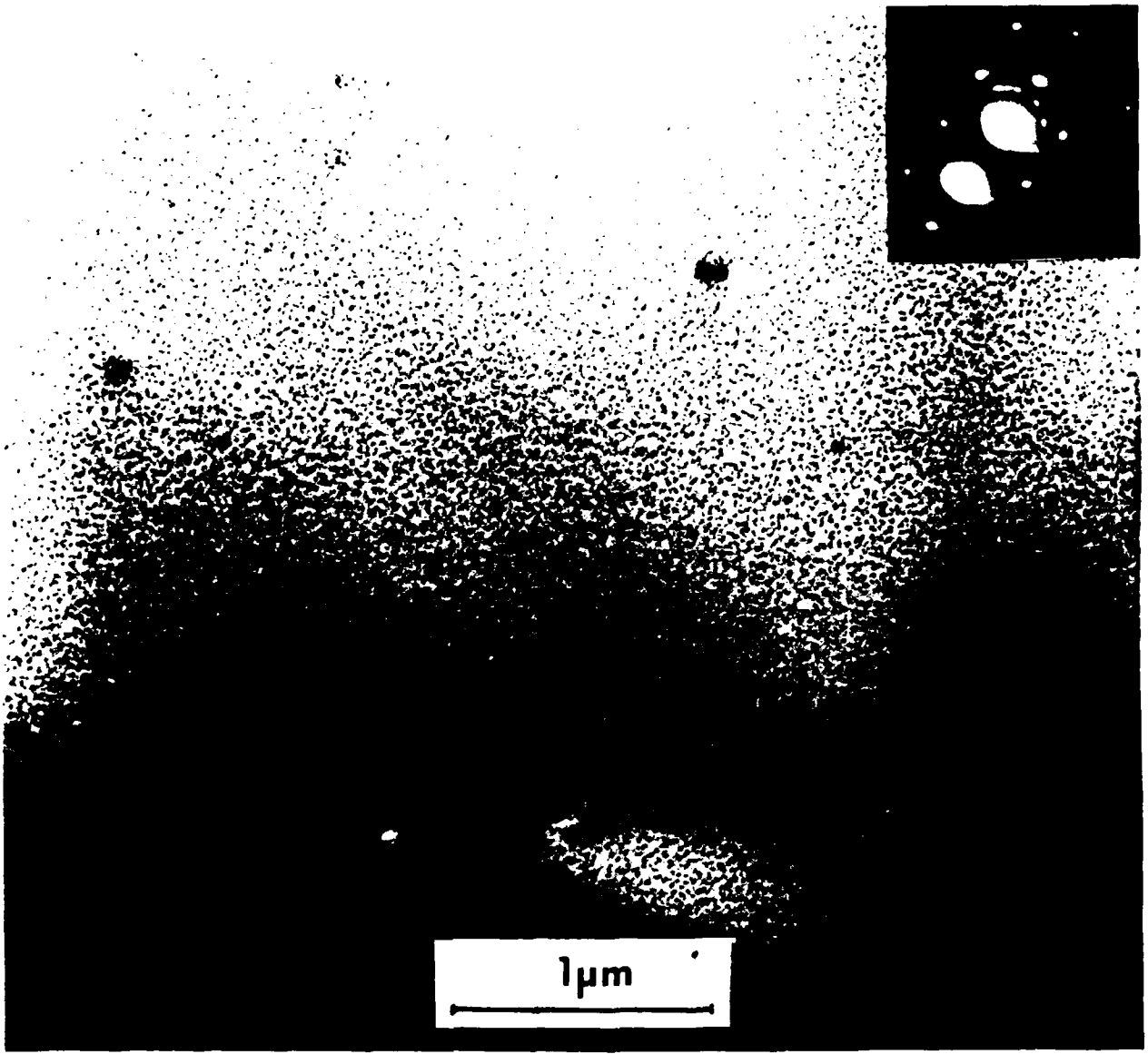
1μm

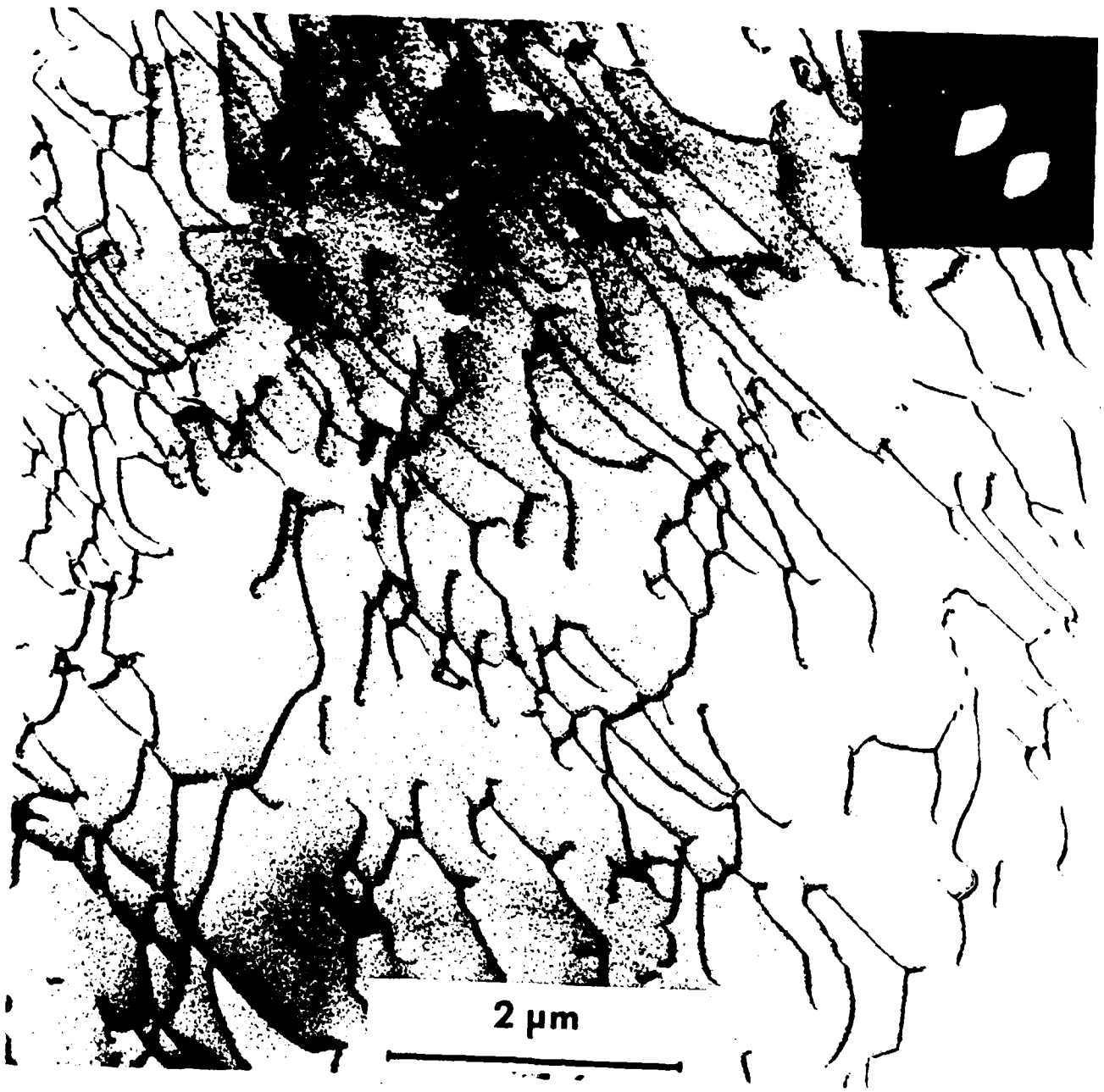
2 µm


1mm

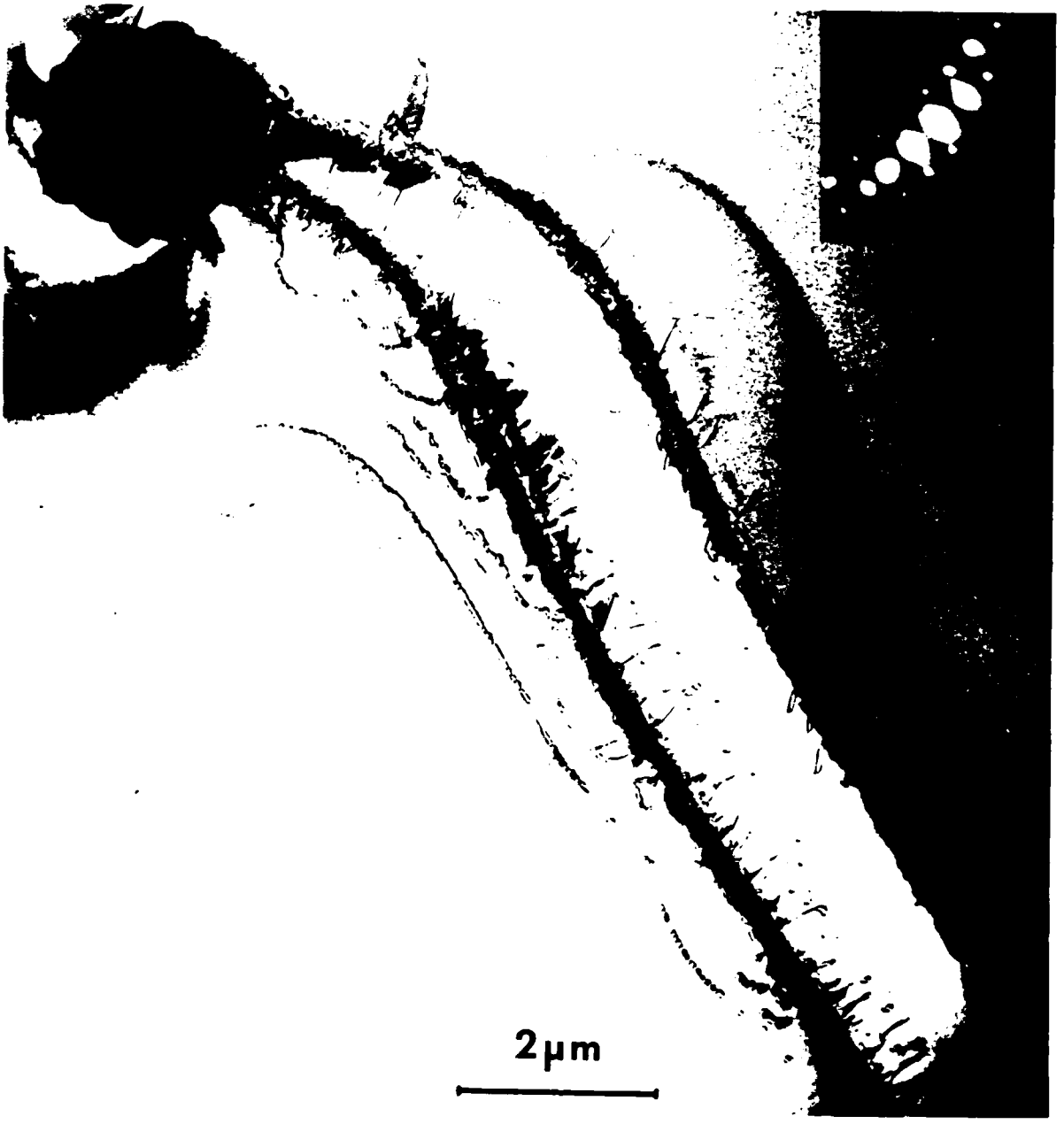
2µm

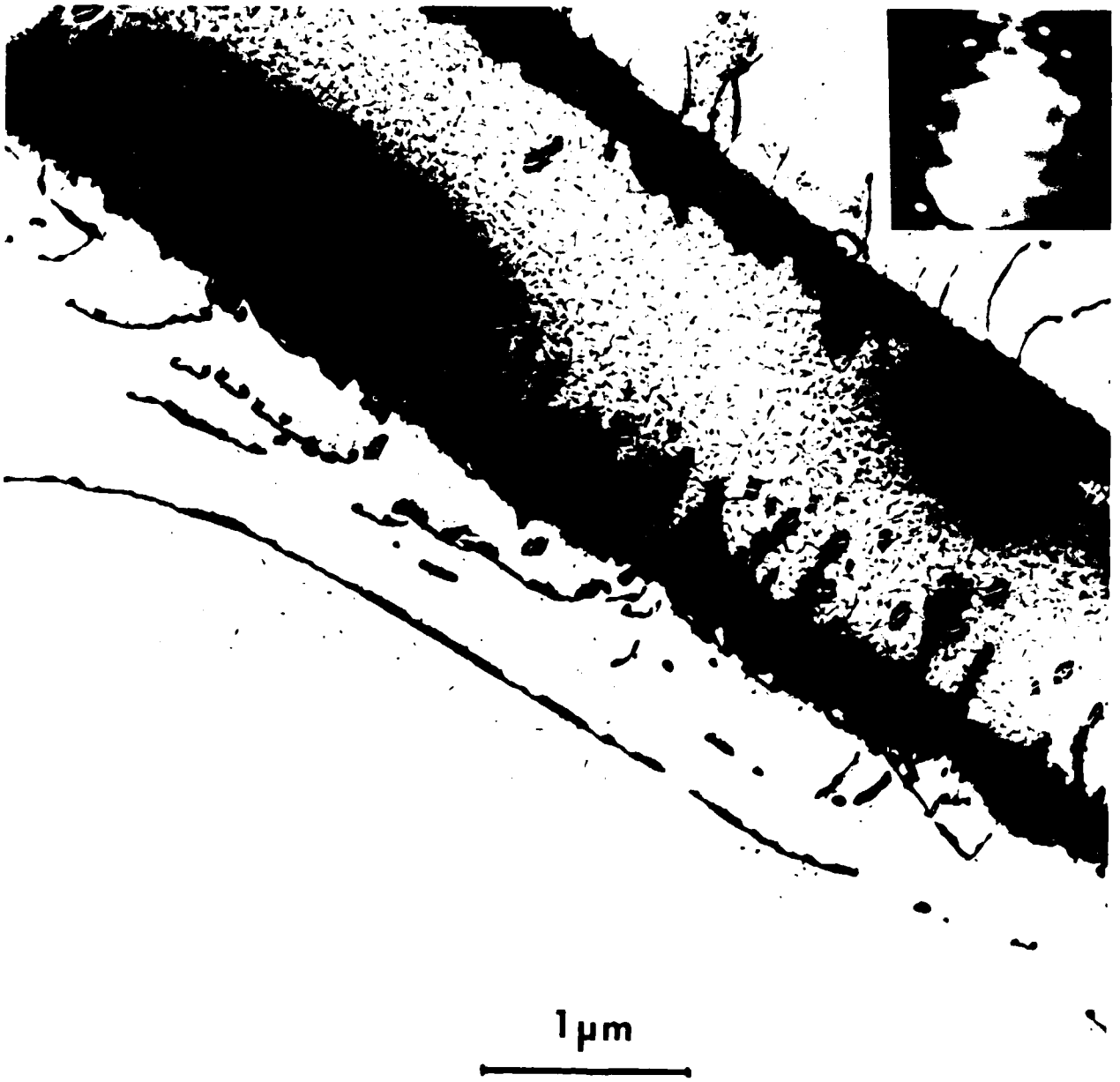
1μm

Section II-4

Initial Stages of Oxide Formation on HgCdTe Exposed to Activated Oxygen

J. A. Silberman*, D. Laser+, I. Lindau, and W. E. Spicer†

Stanford Electronics Laboratory
Stanford University
Stanford, California 94305

and

J. A. Wilson, Santa Barbara Research Center
Goleta, CA 93017

ABSTRACT

The changes in chemistry and electronic structure of the (110) cleavage surface of $Hg_{0.65}Cd_{0.35}Te$ and properties of the film produced are determined by monitoring with photoemission spectroscopy the growth of thin (10 A) oxide layers on initially clean surfaces. Oxygen uptake, normally quite slow, is stimulated in this case by operating an ionization gauge in line of sight of the sample during the exposures so as to provide a stream of excited oxygen striking the surface. A complex Te oxide is formed which retains Cd but not Hg. The Cd content appears enhanced at the oxide surface. An explanation for the behavior observed is sought in terms of the species produced by the activating gauge and the chemistry of the alloy surface.

* Fannie and John Hertz Foundation Fellow

+ Permanent address: Ministry of Defense, P. O. Box 2250, Haifa, Israel

† Stanford Ascherman Professor of Engineering

Introduction

Oxide interface electronic properties can have a first order effect on the performance of devices which have surfaces passivated by a protective oxide or which utilize an MIS structure. Passivation by anodic oxidation, for example, can alter device performance due to fixed charge at the interface and the possibility of a high density of surface states [1]. Similar electrical behavior has been obtained for plasma anodized samples [2]. In both of these cases of native oxide growth, the electrical properties can be modified somewhat by varying the growth conditions or pregrowth treatment [2,3]. For photochemically deposited SiO_2, a thin native oxide layer present on the HgCdTe prior to deposition is believed to have a beneficial impact on the ultimate interface quality [4]. Understanding oxide formation at the microscopic level can lead to optimization of this critical interface property.

In a preliminary study to identify the aspects of the alloy oxidation which influcence the interface quality, an effort has been made to monitor the changes in surface chemistry and electronic structure resulting from the step-by-step growth of thin (~ 10 Å) oxide films on atomically clean HgCdTe exposed to oxygen. Use of photoemission spectroscopy allows high surface sensitivity in following the oxygen uptake. Earlier applications of this technique to study dry oxidation determined HgCdTe to be highly inert with regard to uptake of oxygen in the molecular ground state on both the ion bombarded (111) [5,6] and cleaved (110) [7] surface. In thin oxides formed by stimulating uptake with ultraviolet radiation [6] or an operating ionization gauge [7], oxides containing Hg were not observed while oxides of Te, including those with appreciable Cd content, were proposed to explain the observed chemical composition

of the films obtained [6,7].

The data presented here were obtained on the (110) cleavage face of $Hg_{0.65}Cd_{0.35}Te$. In addition to a determination of the oxide elemental constituents in agreement with the earlier work - the oxide formed contains Cd which appears to segregate to the surface but lacks Hg - several observations of importance to the nature of the oxide - semiconductor interface are detailed. The trends observed with x = 0.35 material are typical of those seen with alloys of other compositions [8].

Experimental

The material used in this study consisted of a 5x5x15 mm^3 single crystal bar of $Hg_{0.65}Cd_{0.35}Te$ ($p \sim 10^{17} cm^{-3}$) grown by solid state recrystallization. The ability to transfer the sample into the main chamber without breaking vacuum allowed a good base pressure ($\leq 10^{-10}$ torr) to be obtained without heating the crystal. It also permitted the oxygen exposures described below to be performed in the small evacuated volume from which the crystal was originally transferred, thereby reducing pumping time following doses and preserving the quality of the vacuum in the main chamber. This evacuated appendage was separately baked prior to the oxidation to reduce the total pressure and water vapor content. Atomically clean surfaces for study were produced by cleaving in vacuum through the cross section of the bar to expose a (110) face.

Because HgCdTe is highly inert to ground state molecular oxygen [5,6,7] an operating ionization gauge positioned in line of sight of the sample surface served to stimulate uptake. In order to investigate the activated species responsible for oxidation, the evacuated appendage used for the exposures was configured to allow control of the sample potential. The dosing procedure consisted of transferring the sample from the

main chamber to the evacuated appendage and isolating the two volumes, positioning the sample in direct line of sight of the ionization gauge, making electrical contact to the sample, admitting research purity oxygen and maintaining a constant pressure for a fixed period, then removing the oxygen and returning the sample to the main chamber for analysis. The bias applied to the sample was either 0, 190 or - 190 VDC. (The highest potential in the guage is 175 VDC.) During the exposure, the guage emission current was regulated at 0.4 mA, permiting pressure measurement throughout the range used, 10^{-4} to 5 x 10^{-3} torr. The duration of each exposure was fixed at 500 sec, and the exposure level quoted is the accumulated pressure-time product in units of 10^{-6} torr - sec (1 Langmiur). A leak valve between the exposure volume and pumping system allowed continuous low speed pumping of the gas atmosphere so as to minimize the partial pressure of possible contaminants; no evidence of carbon on the surface was obtained in X-ray photoemission scans performed to assess cleanliness. With the procedure above, the time required to remove the sample, expose it, and replace it typically totalled 60 minutes. In the case of one exposure, discussed in the next section, eight hours elapsed between exposure and analysis because the light source was unavailable for the photoemission measurements. During this period, the sample remained in the main chamber ($p \leq 10^{-10}$ torr).

The photoemission measurements utilized monochromatic light in the energy range $65 \leq h\nu \leq 600$ eV from beam line I-1 at the Stanford Synchrotron Radiation Laboratory. The U. V. photons were incident on the sample face at an angle of 75° to the normal, and the distribution of electrons emitted were energy analyzed and collected by a double pass cylindrical mirror analyzer with symmetry axis along the sample normal.

The combined resolution of monochromater and electron analyzer in the spectra presented here is 0.18 eV.

In addition to the spectra of clean and oxygen exposed HgCdTe, the emission from a gold film evaporated in situ onto a stainless steel substrate was recorded; determination of the high kinetic energy cut off of the gold emission (the Fermi edge) allows measurement of the Fermi level position on the alloy surface [9].

Simultaneous to the measurement of the photoemission spectra, the relative intensity of the incident photon beam was monitored by measuring the photoelectron yield from an 80% transmitting stainless steel mesh coated with copper in situ and positioned to intercept the beam [10].

Results and Discussion

Both the nature of species produced by the gauge and the interaction of these species with the alloy surface affect the oxidation process. Through the range of oxygen pressure used (10^{-4} to 5×10^{-3} torr), the excited species vary in type and concentration. At the low pressure end, the primary source of excitation is electron impact ionization near the gauge, resulting in positive ions, atomic oxygen, metastable species and electrons [11,12]. As the pressure increases, so does the number of collisions between these species and molecular oxygen, and the ambient composition approaches that of an oxygen plasma, where the negative ion concentration can also be significant [13].

The interaction of the oxygen ions with the alloy surface can be controlled by biasing the sample. Because the highest potential in the gauge is 175 V, a bias of 190 V applied to the sample will repel positive ions while attracting negative species. The surface exposed while biased at ground potential is subject to the combined irradiation

of positive ions (with kinetic energy up to 175 eV) and neutrals, while negative particles will be attracted by the gauge rather than the sample. Biasing the sample negative serves to increase the energy of the positive ions and may increase the ion flux as well by drawing ions away from the grounded chamber walls.

Three surfaces of the same crystal were studied under differing bias conditions. One received a sequence of oxygen exposures while held at ground (surface A). A second, exposed under identical conditions of pressure, time, and gauge emission current was biased to 190 V to eliminated effects due to positive ion bombardment (surface B). The third surface was exposed to only the first two doses of the sequence with the initial exposure performed with positive bias as was the case for surface B, and the subsequent dose administered with the sample biased to -190 V in the hope of accentuating the influence of positive ions and eliminating interactions with negative species.

The conditions of exposure for the three surfaces are summarized in Table I, where features describing the three clean surfaces and the salient results of the initial dose for each are also given for future reference. The data presented below indicate several aspects of the oxidation which appear to depend on the sample bias and the ion contribution. The amount of elemental Te observed and type of oxide formed upon the initial exposure (Table I) are examples of these. Other observations, however, are independent of bias, suggesting processes other than ion bombardment contribute significantly to the oxidation. Because of the complexity of the excited oxygen in the geometry used as

well as of the O-Te-Cd-Hg system itself, further study is required to specify completely the reactions observed here. In light of this, the discussion presented is intended to delineate issues of importance for future investigation. Thus, the data is discussed both with regard to the influence of the ionic content of the oxidizing ambient and processes related to the alloy surface - oxygen interaction itself.

The trends in Hg and Cd content in the growing film remain the same whether positive ions are attracted (surface A) or repelled (surface B). The electron energy distribution curves from the valence band and Hg 5d and Cd 4d core levels as a function of accumulated oxygen exposure for the grounded sample (surface A) are presented in Figure 1 normalized to the copper photoyield from the grid used as an intensity monitor. In the spectrum for the clean surface, the valence band emission falls between 54 and 60 eV. The sharp peaks at 52.4 and 50.6 eV are the Hg 5d spin orbit split peaks; the Cd 4d lines with 0.6 eV splitting appear around 49.5 eV. As the oxygen exposure increases, oxygen 2p derived intensity grows in magnitude (56.4 eV), while the Hg 5d core emission falls. Resolution of the splitting in the Cd 4d levels is lost, indicating a change in the Cd environment, and the strength of the Cd derived signal increases with increasing oxygen coverage. By the highest exposure, the integrated Cd 4d emission is roughly 80% stronger than that obtained from the clean surface, while the Hg 5d core line has diminished to less than 10% of its original intensity. The ratio of Cd to Te following the 4.4×10^6 L dose is roughly 50% higher than the cleaved surface value. This suggests that either the oxide formed is Cd rich compared to the substrate or that Cd segregates to the film surface. Measurements

made with higher $h\nu$ give a Cd signal closer to that of the cleaved surface; because the emission in these cases includes a smaller proportion of surface information, the data support the second hypothesis, that Cd segregates to the surface of the growing film. Because this conclusion is based on an analysis which includes contributions from both the bulk and oxide weighted by the electron escape depth, it holds true even for thin films; an accurate determination of the escape length in the alloy and oxide is required to confirm this result, however.

From the region above 51 eV in the spectrum for the highest exposure, a two peaked electron distribution is observed, with structure at 56.4 and 52.6 eV. The lower kinetic energy feature is mainly due to oxygen rather than Hg despite the fact that it falls at an energy near that for the Hg peak. This was determined in two ways. First, the photon energy dependence of this peak is different than that expected for a 5d orbital: the variation in intensity of the 52.6 eV peak between $h\nu$ = 130 and $h\nu$ = 180 eV is approximately the same as that of the higher energy 2p derived structure rather the Hg 5d line in the case of the clean surface of HgCdTe or atomic Hg [14]. In addition, the valence emission from CdTe exposed to activated oxygen (but in a different experimental geometry) exhibits the same two structures with similar separation [8]. Thus both the 56.4 and 52.6 eV peaks are associated with the oxide.

Several important features of the oxide formation in the line-of-sight geometry appear in the Te 4d spectra. The data for the surface for which positive ions may play a role (surface A) are given in Figure 2 normalized to the copper photoyield. As was the case with the Hg core lines, the Te $4d_{5/2}$ and $4d_{3/2}$ levels at 50.6 and 49.1 eV, respectively, are attenuated

as the oxide film increases in thickness. Simultaneously, chemically shifted Te 4d emission is observed around 3.4 to 3.6 eV more tighly bound, signalling the growth of the oxide layer. At the highest exposure, the photoemission signal originates mainly within the oxide layer, as indicated by the small remaining contribution at the bulk peak position. This observation combined with those obtained from Fig. 1 implies that the Hg and Cd signals reflect mainly the composition of the oxide, confirming the exclusion of Hg and incorporation (and segregation) of Cd.

Detailed examination of both the bulk Te signal and oxidized Te emission reveals two additional aspects of the line of sight stimulated oxygen uptake. The spectrum recorded following the initial exposure (Figure 2) shows considerable asymmetry in the bulk core lines, with new intensity occuring at higher binding energy. This contribution persists until an exposure of 1.9×10^6 L is reached, although it is attenuated somewhat more rapidly than the bulk emission with the second and subsequent exposures. Using the peak shape and splitting in the spectrum from the cleaved surface, a quite accurate fit of the unoxidized, asymmetric 4d lines can be obtained by summing contributions from peaks at the bulk binding energy and 0.7 eV more tightly bound. The new state induced by the oxygen exposure corresponds to elemental Te. (The separation of 0.7 eV for the deconvolved peaks is somewhat larger than but consistent with the value of peak separation reported by other groups [15,16].) Presumably, the elemental component is oxidized with additional doses. When the initial exposure was performed with the sample biased to repel positive ions (surfaces B and C, Table I) an order of magnitude less free Te was detected, and the amount remained small in subsequent

exposures. The Hg loss upon the initial exposure was also smaller.

The second exposure related change apparent in Figure 2 is the variation in peak position and shape evident in the Te 4d emission arising from the oxidized Te. This is particularly evident in comparing the spectra for the two highest exposures. The broadening which occurs between the two doses and the width of the peaks in the oxide compared to those of the cleaved surface suggest at least two chemical environments or types of oxide contribute to the spectra. A change in peak position is therefore a reflection of a change in the proportion of the component peaks at different energies which contribute to the measured curve; the larger the fraction of an oxide with a higher binding energy Te core line, the greater the binding energy of the peak resulting from the sum of all contributions. Because suitable reference oxides were unavailable for examination, an attempt to identify the various components in the film produced in the line of sight configuration was not made. While efforts to use the cleaved spectrum or the relatively sharp lines in the 1.9×10^6 L curve to deconvolve the constituents resulted in only a qualitative fit, they indicate the probable separation in energy for the Te lines in the contributing compounds to be between 0.5 and 0.7 eV.

The change in the mixture of Te oxides as a function of exposure and bias is indicated in Figure 3, where the difference in energy between the oxide Te core lines and those for Te in HgCdTe (the chemical shift) is plotted for the three surfaces studied. Two composition regimes are apparent from chemical shifts around -3.4 eV and in excess of -3.6 eV. For the initial 5×10^4 L dose, liberation of elemental Te occurs for the sample at ground (see Fig. 2), and the chemical shift

produced indicates a larger fraction of an oxide with higher binding energy Te core lines (Table I). While subsequent exposure of the samples initially exposed with +190 V bias to repel positive ions increases the higher binding energy contribution, the oxidized Te 4d lines for the sample held at ground exhibit a roughly constant or slightly decreasing chemical shift up to an exposure of 1.9×10^6 L, where the shift changes abruptly by 0.2 eV (Figure 3) and the peaks sharpen (Figure 2). For the highest dose, the chemical shift is independent of bias and the oxide constituents result in an identical, broadened peak shape for the Te core lines for both surfaces studied.

The complex behavior suggested by the data in Figure 3 must originate from a combination of the activated oxygen - alloy surface chemistry and nature of the oxidizing ambient as influenced by ion gauge, sample bias, and pressure. An additional aspect of the oxygen uptake observed in the line of sight procedure is illustrated in Figure 4, where the thickness of the film [17] is plotted against exposure for the three surfaces exposed under different biases. The uptake for the sample at ground and 190 V is essentially the same over the sequence of exposures, and the 1.5×10^5 L dose performed with the sample biased to -190 V results in film growth similar to the 0 and 190 V cases. Because the grounded sample, surface A, was positioned improperly for the 4×10^5 L exposure, this point falls below the curve. A detailed explanation for the interaction of activated oxygen and HgCdTe must therefore explain

1) the apparent bias dependence of the oxide formed and elemental Te produced on the first exposure
2) the "anomolous" value of chemical shift at 1.9×10^6 L for

the zero bias sample and

3) the equivalent rate of uptake observed independent of bias.

One explanation for the behavior observed on activated oxygen uptake makes use of the change with exposure or pressure of the relative importance of two simultaneous processes - adsorption of an activated species and bombardment by the positive ions produced at the gauge, for example. In this picture, the initial oxygen uptake is accompanied by disordering of the surface by the positive ions for the sample at ground, resulting in the formation of a mixed oxide and elemental Te. For surfaces exposed under positive bias the ion related process is inhibited, and oxidation results in a different film. The sudden change in chemical shift after the exposure to total 1.9×10^6 L would in this description be the result of an inceased role for the ion related process at this pressure, although the final film at 4.4×10^6 L is independent of the sample bias and thus positive ion contribution. Two observations tend to corroborate this explanation that an alteration in the balance between ion bombardment and oxygen uptake is responsible for the changes observed. The positive ion current measured with a Faraday cup at the sample position showed a maximum near the pressure used to reach 1.9×10^6 L. Also, exposure in the same line-of-sight geometry of the film after the 4.4×10^6 L oxygen dose to 4×10^4 L of argon with the sample biased to -200 V to accelerate positive ions resulted in a chemical shift and peak shape similar to the 1.9×10^6 L, zero bias case.

The above arguments support in certain cases the importance of the ambient and sample bias in determining activated oxygen uptake. An important result of such an analysis is that ion irradiaion has quite

a different effect on the bare alloy than on the oxide, as evidenced by the independence of oxide thickness on sample bias. A complete understanding of the possible role of ion bombardment also requires consideration of the negative ion component of the gas, which may be significant at higher pressures [13].

For the purpose of highlighting issues related to oxide interface formation as suggested by the data from the line of sight stimulated uptake, it is perhaps fruitful to consider an explanation of the phenomena observed which subordinates the role of the oxidizing ambient and emphasizes the alloy surface chemistry instead. Such an approach is suggested, for example, by the increase in chemical shift from -3.4 to -3.6 eV for the oxide formed on the sample exposed under a bias to repel positive ions (surface B). This shift in the absence of positive ion bombardment indicates the mixture of oxides formed may be a manifestation of the alloy surface oxygen chemistry.

In the context of a description which emphasizes the surface reactions rather than the oxidizing medium, an explanation of the "anomolous" chemical shift at 1.9×10^6L for the grounded surface and the independence of uptake on bias proceeds as follows. The singular shift at 1.9×10^6L is associated with the delay between exposure and analysis unique to this dose. While all other exposures were immediately followed by the photoemission measurements so that the interval between doses was fairly constant, a period of eight hours elapsed after this exposure before the data could be recorded. The change in chemical shift thus indicates that one of the components contributing to the oxidized Te film may be unstable. Unfortunately, the spectra show the effects of both the change with time and exposure, so that

one cannot assign differences in the spectra to one process or the other. Further, the instability may be a transformation of the oxide rather than desorption [18]. Because this description assigns importance to the kinetics of the oxygen-surface interaction rather than the oxidizing agent, the same uptake on each surface studied is possible if the active species is not influenced by bias; atomic oxygen is thus a candidate for the active species. Finally, the implication of this picture is that for the initial exposure, the more stable oxide, as identified by the -3.4 eV chemical shift, is formed first (and less elemental Te liberated) on the 2nd and 3rd cleaves studied (at 190 V bias to exclude positive ions).

In addition to data on the chemical and structural changes which take place upon oxidation, information relating to the interface electronic properties was also determined. Photoemission spectroscopy can directly measure the surface Fermi level position of a material and can monitor changes in band bending in a semiconductor as modifications to the surface charge distribution take place [9]. The results of such a measurement after cleavage and as a function of exposure for the three (110) surfaces studied are presented in Figure 5. Depicted is the Fermi level position in the band gap as determined from location of the gold film Fermi edge and the clean surface valence band maximum (VBM) and from changes in the band bending obtained by tracking the Te core level emission arising from the bulk HgCdTe deconvolved from any elemental Te contribution. As the bulk value of E_F for the room temperature carrier concentration and band gap of this p-type x = 0.35 sample was 0.123 eV above the VBM, all three surfaces appear to have converted to n-type upon cleaving, a

phenomenon frequently observed in the alloy [19,20]. The degree of conversion varies from cleave to cleave, with a maximum difference in E_F of 0.16 eV. Upon oxygen exposure, the interface region of the semiconductor becomes increasingly n-type; in the case where the cleaved surface was degenerately n-type, no further band bending was observed, however. Changes in band bending upon oxidation are commonly observed in compound semiconductors and attributed to the introduction of defects with oxygen uptake [9]. Similarly, it is likely that defects introduced by cleavage are responsible for the surface type conversion [19,21] and perhaps play a role in the oxygen uptake.

Summary

Oxygen uptake by the cleaved (110) face of $Hg_{0.65}$ $Cd_{0.35}Te$ has been studied using photoemission spectroscopy. Activation of the oxygen by operating an ionization guage in line of sight of the sample surface serves to stimulate uptake, but may introduce extraneous effects as well. The trends observed as the coverage increases--formation of a mixed oxide with release of Hg and retention and segregation of Cd--are independent of sample bias, however, as is the rate of uptake, suggesting that while the nature of the oxidizing ambient produced with the gauge is clearly important, the alloy oxygen chemistry plays a fundamental role in the observed behavior. Detailed understanding of the types of oxide formed, their stability, the electrical nature of the interface, and the possible relationship between the factors which affect surface type conversion and the initial oxygen uptake--issues evident in the line-of-sight oxidation study reported here--requires continued investigation.

Acknowledgements

We express our appreciation to Roger A. Cole at SBRC for growth of the material used in this study. This study is supported by DARPA contract No. 800989-B8. The work reported herein was performed at the Stanford Synchrotron Radiation Laboratory, which is supported by the Department of Energy, Office of Basic Energy Sciences; and the National Science Foundation, Division of Materials Research.

References

1. Y. Nemirovsky and J. Kidron, Solid State Electr. 22, 831 (1979) T. S. Sun, S. P. Buchner, and N. E. Byer, J. Vac. Sci. Technol. 17, 1067 (1980).
2. Y. Nemirovsky, R. Goshen, and J. Kidron, J. Appl. Phys. 53, 4888 (1982).
3. Bruce K. Janousek and Richard C. Carscallen, J. Vac. Sci. Technol. 21, 442 (1982).
4. J. A. Wilson, V. A. Cotton, J. A. Silberman, D. Laser, W. E. Spicer, and P. Morgen, to appear in J. Vac. Sci. Technol., Proceedings of the 2nd U.S. Workshop on the Physics and Chemistry of HgCdTe, Dallas, TX, Feb. 8-10, 1983.
5. S. P. Kowalczyk and J. T. Cheung, J. Vac. Sci. Technol. 18, 944 (1981).
6. U. Solzbach and H. J. Richter, Surf. Sci. 97, 191 (1980).
7. P. Morgen, J. A. Silberman, I. Lindau, W. E. Spicer, and J. A. Wilson J. Electr. Mater. 11, 597 (1982).
8. J. A. Wilson, Joel Silberman, Per Morgen, and W. E. Spicer, Semiannual Technical Paper, DARPA contract No. MDA-903-80-C-9469, March (1982).
9. W. E. Spicer, P. Skeath, C. Y. Su, and I. Lindau, J. Phys. Soc. Japan 49, Suppl. a, 1071 (1980).
10. B. B. Pate, Ph.D. thesis, Stanford University (1983).
11. Donald Rapp and Paula Englander-Golden, J. Chem. Phys. 43, 1464 (1965). Donald Rapp and Donald D. Briglia, J. Chem. Phys. 43, 1480 (1965).
12. E. W. McDaniel, V. Cermak, A. Dalgarno, E. E. Ferguson, and L. Friedman, Ion-Molecule Reactions (John Wiley and Sons, New York, 1970).
13. J. B. Thompson, Poc. Roy. Soc. A 262, 519 (1961).

14. P. H. Kobrin, D. A. Heimann, H. G. Kerkoff, D. W. Lindle, C. M. Truedale, T. A. Ferrett, U. Becker, and D. A. Shirley, Phys. Rev. A 27, 3031 (1983).

15. G. D. Davis, T. S. Sun, S. P. Buchner, and N. E. Byer, J. Vac. Sci. Technol. 19, 472 (1981).

16. David R. Rhiger and Robert E. Kvass, J. Vac. Sci. Technol. 21, 448 (1982).

17. The thickness was estimated by modeling the oxide layer as homogeneous and uniformly distributed with an abrupt interface separating oxidized and bulk Te. The further assumptions of constant density for the Te and a mean free path of 7 Å at 50 eV kinetic energy were used. Thicknesses of parts of an angstrom represent coverages below a monolayer.

18. David R. Rhiger and Robert E. Kvass, to appear in J. Vac. Sci. Technol., Proceedings of the 2nd U. S. Workshop on the Physics and Chemistry of of HgCdTe, Dallas, TX, Feb. 8-10, 1983.

19. P. M. Raccah, U. Lee, J. A. Silberman, W. E. Spicer and J. A. Wilson, Appl. Phys. Lett. 42, 374 (1983).

20. R. R. Daniels, G. Margaritondo, G. D. Davis, and N. E. Byer, Appl. Phys. Lett. 42, 50 (1983).

21. W. E. Spicer, J. A. Silberman, I. Lindau, A.-B. Chen, A. Sher, and J. A. Wilson, to appear in J. Vac. Sci. Technol., Proceedings of the 2nd U.S. Workshop on the Physics and Chemistry of HgCdTe, Dallas, TX, Feb. 8-10, 1983.

22. G. L. Hansen, J. L. Schmit, and T. N. Casselman, J. Appl. Phys. 53, 7099 (1982).

FIGURE CAPTIONS

Figure 1 Valence band and Hg 5d and Cd 4d core level emission from clean and oxygen exposed $Hg_{0.65}Cd_{0.35}Te$ for the surface held at ground (Table I). With increasing exposure, the Cd lines and oxygen induced structure rise in intensity while the Hg emission is attenuated.

Figure 2 Te 4d core level emission as a function of line of sight oxygen exposure for the surface held at ground (Table I). The broadening of the bulk lines with exposure indicates formation of elemental Te, while the width of the oxidized Te results from formation of more than one oxide.

Figure 3 Variation of oxide composition as reflected by the chemical shift (difference between bulk and oxide peaks in Figure 2) as a function of exposure for samples dosed under different bias condition (see Table I). See text for discussion of the processes which produce the shifts shown.

Figure 4 Thickness of oxide film (Ref. 17) versus exposure for the three surfaces studied. The samples exposed at ground and 190 V potential (attracting and repelling positive ions) show similar uptake throughout the range of exposures used.

Figure 5 Position of the Fermi level at the surface for the three cleaves studied and variation in E_F with oxygen uptake. The uncertainly in the absolute value of E_F is 0.2 eV; the precision with which changes in E_F can be detected is approximately 0.05 eV. Initial cleavage renders each surface n-type (the bulk material is p-type) and the bands bend down increasingly with exposure. The value of E_g is from Ref. 22.

TABLE I: Summary of Exposure Conditions and Salient Results of Initial Uptake

Designation	Exposure Conditions		Clean Surface	After Initial Exposure	
	Bias	Influence of bias on oxygen ions	$E_{F,surface}$ (a)	Ratio of elemental Te to bulk Te intensity	Chemical shift of Te 4d peaks in oxide (b)
Surface A	0 V for all exposures	attracts positive ions	0.37 eV	0.30	-3.67 eV
Surface B	190 V for all exposures	repels positive ions, attracts negative species	0.26 eV	0.02	-3.42 eV
Surface C	190 V for initial dose (5×10^4 L) and -190 V for next dose (1.5×10^5 L)	-190 V accelerates positive ions, repels negative	0.22 eV	0.05	-3.46 eV

a) Fermi level position measured from the valence band maximum (VBM). The location of E_F in the bulk is 0.123 eV above the VBM, and the band gap is 0.36 eV (Ref. 22).

b) Difference is energy of Te 4d line for Te in the oxide and Te in the HgCdTe. See Figure 3 and the text for further discussion.

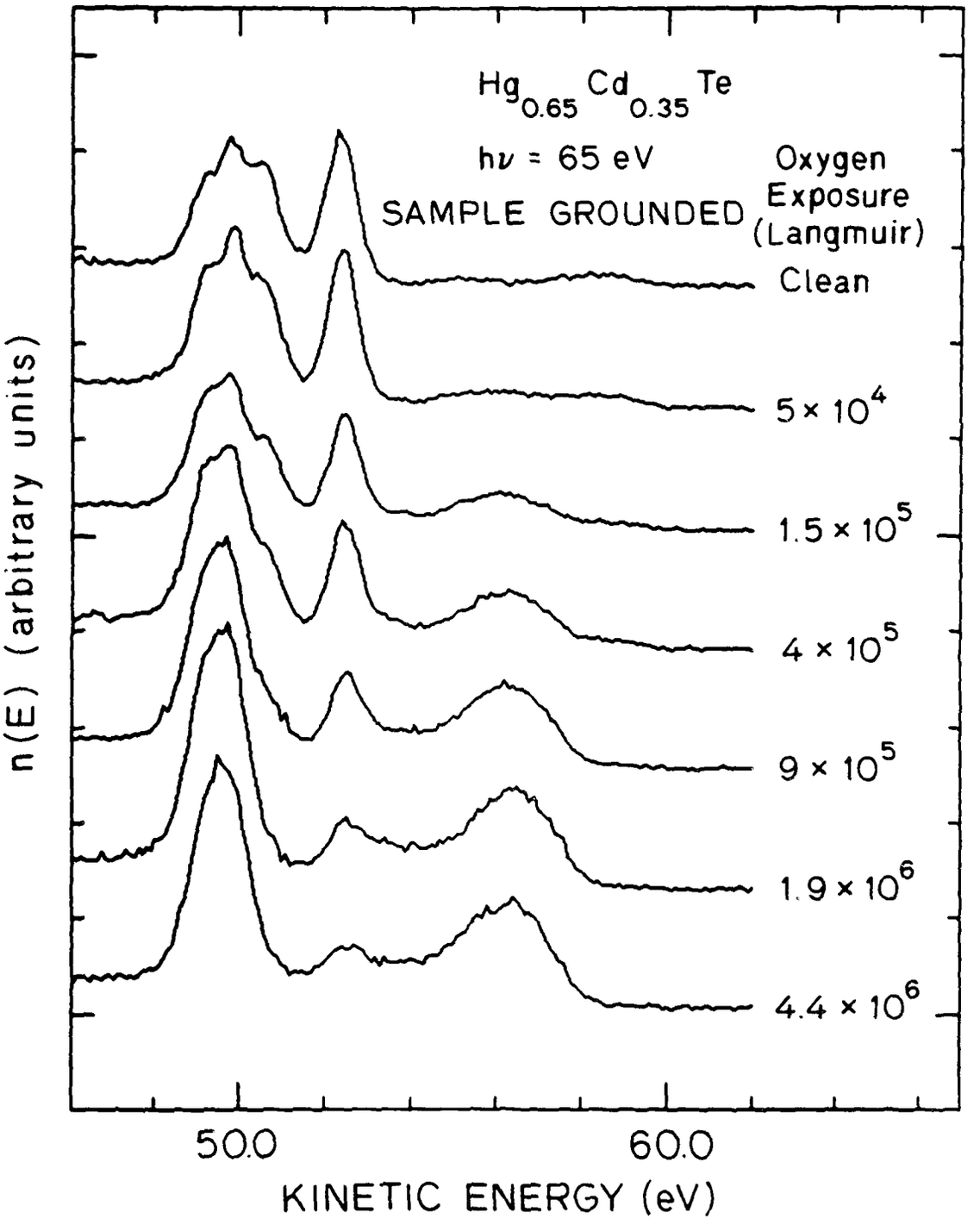
$Hg_{0.65}Cd_{0.35}Te$
$h\nu$ = 65 eV
SAMPLE GROUNDED
Oxygen Exposure (Langmuir)
Clean
5×10^4
1.5×10^5
4×10^5
9×10^5
1.9×10^6
4.4×10^6
n(E) (arbitrary units)
50.0
60.0
KINETIC ENERGY (eV)

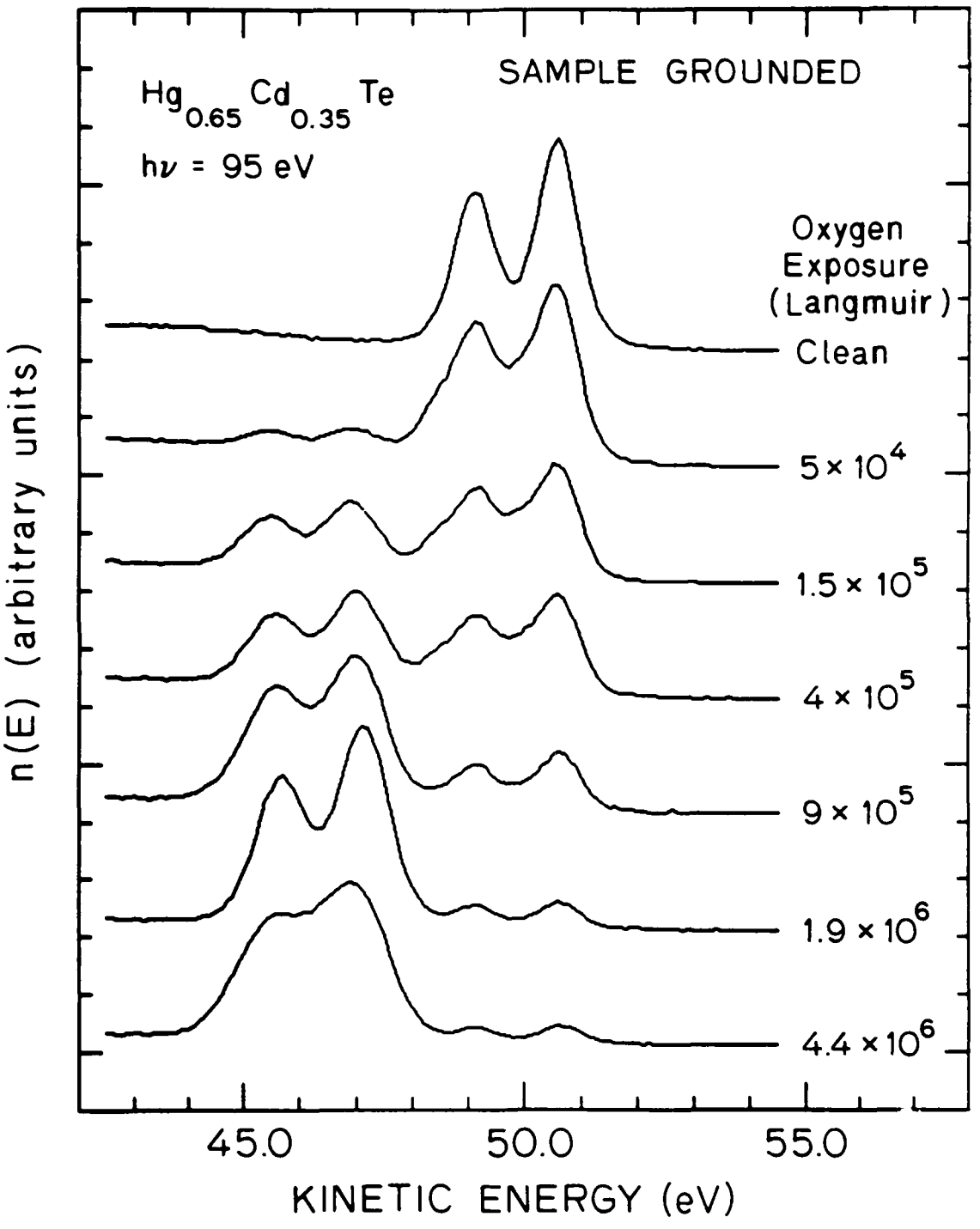
SAMPLE GROUNDED
$Hg_{0.65}Cd_{0.35}Te$
hν = 95 eV
Oxygen Exposure (Langmuir)
Clean
5 × 10^4
1.5 × 10^5
4 × 10^5
9 × 10^5
1.9 × 10^6
4.4 × 10^6
n(E) (arbitrary units)
45.0
50.0
55.0
KINETIC ENERGY (eV)

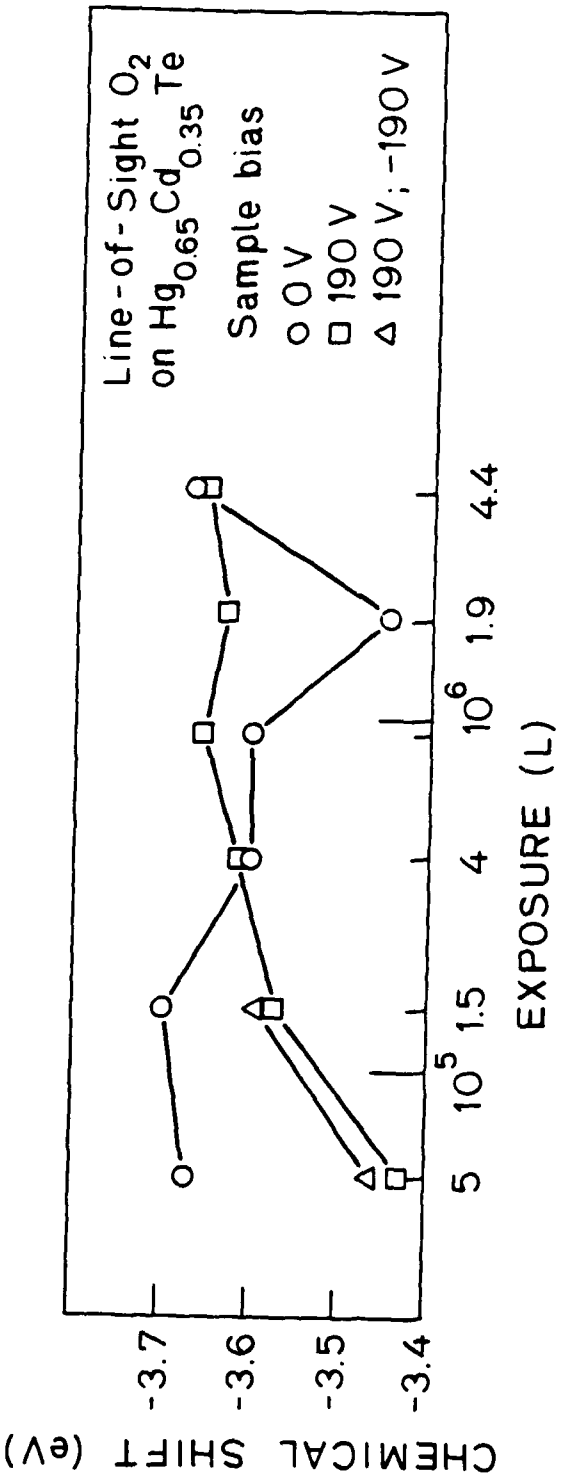
Line-of-Sight O_2 on $Hg_{0.65}Cd_{0.35}Te$
Sample bias
o 0 V
□ 190 V
Δ 190 V; -190 V
CHEMICAL SHIFT (eV)
-3.7
-3.6
-3.5
-3.4
EXPOSURE (L)
5
10^5
1.5
4
10^6
1.9
4.4

Fig. 3

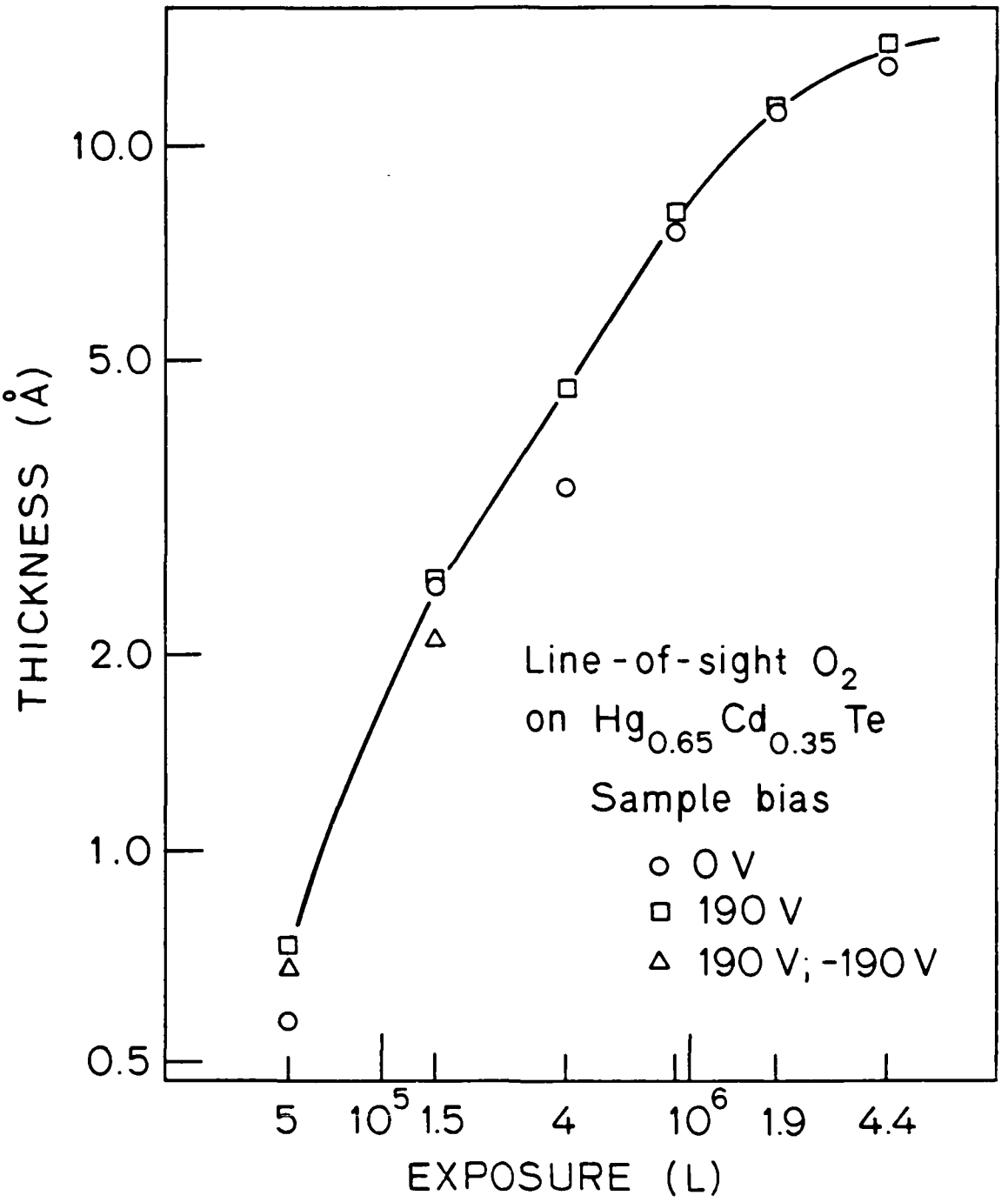
10.0
5.0
2.0
1.0
0.5
THICKNESS (Å)
Line-of-sight O_2
on $Hg_{0.65}Cd_{0.35}Te$
Sample bias
o 0 V
□ 190 V
△ 190 V; -190 V
5
10^5
1.5
4
10^6
1.9
4.4
EXPOSURE (L)

Fig. 4

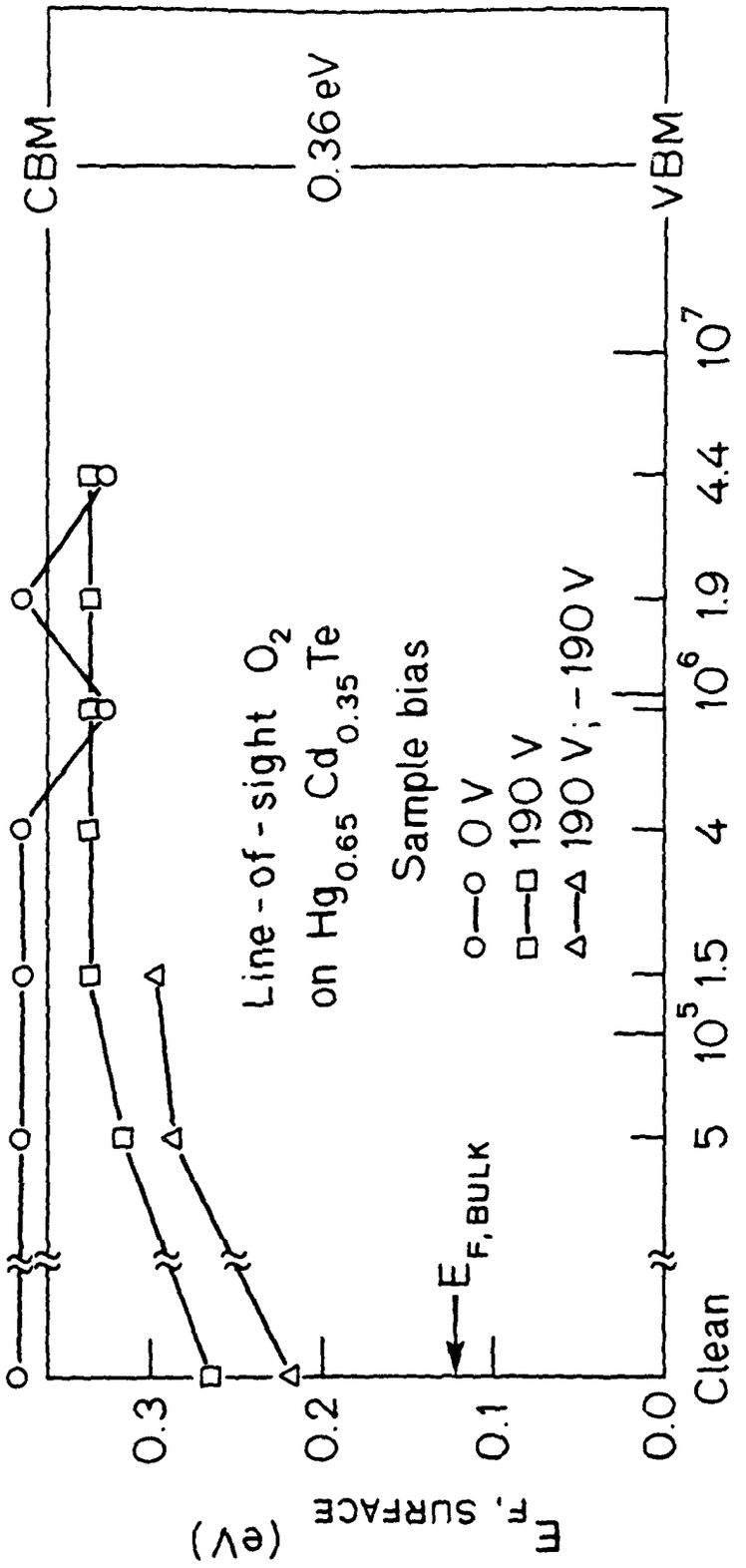
CBM
0.36 eV
VBM
Line-of-sight O_2
on $Hg_{0.65}Cd_{0.35}Te$
Sample bias
O—O 0 V
□—□ 190 V
Δ—Δ 190 V; −190 V
$E_{F,BULK}$
Clean
5
10^5 1.5
4
10^6 1.9
4.4
10^7
EXPOSURE (L)
0.3
0.2
0.1
0.0
$E_{F,SURFACE}$ (eV)

Fig. 5

Section 3
ALLOY BONDING

CONTRIBUTIONS TO BOND ENERGY

According to Harrison[1] there are several contributions to the bond energy in a II-VI compound semiconductor. These contributions are listed below:

1. Transfer Energy

   The transfer energy is

$$E_{transfer} = \frac{2(\varepsilon_{p+} - \varepsilon_{p-})}{4} = \frac{(\varepsilon_{p+} - \varepsilon_{p-})}{2}. \quad (1)$$

   The 2 in the numerator accounts for the energy required to transfer two electrons from each anion to each cation so each starts with four electrons. The 4 in the denominator is there because this energy is shared among four bonds.

2. Promotion Energy

   The promotion energy is

$$E_{promotions} = |V_{1+} + V_{1-}| \quad (2)$$

   where the hop energies between hybrids on the cation and anion are

$$V_{1\pm} \equiv \frac{1}{4}(\varepsilon_{p\pm} - \varepsilon_{s\pm}). \quad (3)$$

   The promotion energy accounts for the energy needed to form sp^3 hybrids on each ion.

3. Bond Formation Energy

   This energy is

$$E_{formation} = -2(V_2^2 + V_3^2)^{1/2} \quad (4)$$

[1] W.A. Harrison, "The Bonding Properties of Semiconductors," Microscience, Vol. 3, (1983) 35. (This is an SRI publication with limited distribution.)

where the covalent energy is expressed in terms of the bond length d

$$V_2 = \frac{24.5}{(d[\text{Å}])^2}\ [\text{eV}], \tag{5}$$

the ionic energy is

$$V_3 = \frac{1}{2}\left(\varepsilon_+ - \varepsilon_-\right), \tag{6}$$

and the hybrid energies are

$$\varepsilon_\pm = \frac{1}{4}\left(\varepsilon_{s^\pm} + 3\varepsilon_{p^\pm}\right). \tag{7}$$

4. Direct Metallization Energy

This energy is

$$E_{dm} = \frac{3.2\left[\left(U_+^b\, U_+^{a'}\, V_H\right)^2 + \left(U_-^b\, U_-^{a'}\, V_{1^-}\right)^2\right]}{\varepsilon_b - \varepsilon'_a}, \tag{8}$$

where the 3 enters because there are three bonds each, adjacent to the anion and cation sides of the bond in question, and the 2 is there because there are two electrons per bond. The quantities $U_\pm^b$ and $U_\pm^a$ are probability amplitudes of finding an electron at one ion or the other in a bonding and antibonding state. They are given by

$$\begin{aligned} U_+^b &= \sqrt{\frac{1 - \alpha_p}{2}} = U_-^a, \\ U_-^b &= \sqrt{\frac{1 + \alpha_p}{2}} = U_+^a, \end{aligned} \tag{9}$$

where the polarity α_p is

$$\alpha_p \equiv V_3/\sqrt{V_2^{\,2} + V_3^{\,2}}. \tag{10}$$

The primes designate quantities associated with an adjacent bond which are not functions of the bond length in question. For a pure compound semiconductor where the equilibrium bond lengths of all bonds are the same, Equation (8) simplifies to:

$$E_{dm} = -\frac{3}{4}\frac{(V_{1+}^2 + V_{1-}^2)\,\alpha_c^2}{(V_2^2 + V_3^2)^{1/2}}. \tag{11}$$

5. Total Overlap Energy

The total overlap energy can be expressed as

$$E_{TO} = Td/4, \tag{12}$$

where the total effective bond tension T has two contributions:

$$T = T_o + T_m. \tag{13}$$

One is from the interbond terms,

$$T_o = \frac{\partial \varepsilon_b}{\partial d} = -\frac{4V_2\alpha_c}{d}, \tag{14}$$

where the covalency is

$$\alpha_c \equiv |V_2|/(V_2^2 + V_3/2)^{1/2} \tag{15}$$

and the bond state energy is

$$\varepsilon_b = \frac{\varepsilon_+ + \varepsilon_-}{2} - \sqrt{V_2^2 + V_3^2}. \tag{16}$$

The other contribution is from metallization, which is an intrabond term:

$$T_m = \frac{\partial(E_{dm} + E'_{dm})}{\partial d}, \tag{17}$$

where E'_{dm} is

$$E'_{dm} \equiv \frac{6[(U_+^{b'}\ U_+^a\ V_{1+})^2 + (U_-^{b'}\ U_-^a\ V_{1-})^2]}{\varepsilon_b' - \varepsilon_a}. \tag{18}$$

It enters because there are terms in the direct metallization energy of the adjacent bonds that depend on the bond length d of the one in question. If the solid is a pure compound so all the bond lengths are the same, then Equations (17), (18), and (8) are equivalent to taking the derivative with respect to d of Equation (11). This is true because some of the d dependence in Equation (11) arises from adjacent bonds. This feature is no longer true in an alloy where Equations (17), (18), and (8) must be used.

All the terms arising from metallization are conveniently grouped into an energy called E_m, given by

$$E_m \equiv E_{dm} + T_m d/4 \tag{19}$$

which for a pure compound is

$$E_m = -\frac{9}{8}\alpha_c^4 \frac{(V_{1+}^2 + V_{1-}^2)}{(V_2^2 + V_3^2)^{1/2}}. \tag{20}$$

Finally, if one collects all these terms for a pure compound, one has

$$E_b = -(1+\alpha_p)^2 (V_2^2 + V_3^2)^{1/2} - \frac{9}{8}(1-\alpha_p^2)^2 \frac{(V_{1+}^2 + V_{1-}^2)}{(V_2^2 + V_3^2)^{1/2}} + |V_{1+} + V_{1-}| + \frac{\epsilon_{p+} - \epsilon_{p-}}{2}, \tag{21}$$

where the bond formation and interbond overlap energies are combined into the first term, the metallization is the second term, and the promotion and transfer energies make up the last two terms.

ALLOY MODIFICATION OF BOND ENERGIES

First focus attention on a bond with one impurity metal ion in a neighboring bond. The arrangement is depicted in Figure 3-1.

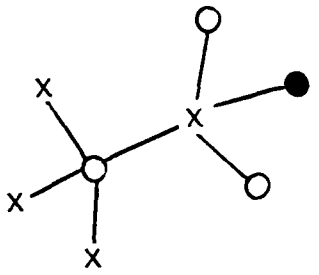

o - Host metal ion (cation)
x - Non etal ion (anion)
● - Impurity metal ion

Figure 3-1

Make the simplifying assumption that the bond lengths in the alloy retain their respective pure crystal values. Then the bond energy is shifted from its pure crystal value, and is given by

$$\Delta E_b^{\,l} = E_b^{\,l} - E_b$$

$$= \frac{2(U_-^{b}\, U_-^{ai}\, V_{-})^2}{\varepsilon_b - \varepsilon_a^{i}} - \frac{2(U_-^{b}\, U_-^{a'}\, V_{-})^2}{\varepsilon_b - \varepsilon_a'}$$

$$+ \frac{\partial d}{4\partial d}\, 2\left[\frac{(U_-^{b}\, U_-^{ai}\, V_{-})^2}{\varepsilon_b - \varepsilon_a^{i}} - \frac{(U_-^{b}\, U_-^{a'}\, V_{-})^2}{\varepsilon_b - \varepsilon_a'} + \frac{(U_-^{bi}\, U_-^{a}\, V_{-})^2}{\varepsilon_b^{i} - \varepsilon_a} - \frac{(U_-^{b'}\, U_-^{a}\, V_{-})^2}{\varepsilon_b' - \varepsilon_a}\right]$$

$$+ \frac{1}{3}\left(\frac{\varepsilon_{p+}^{i} - \varepsilon_{p+}}{2}\right), \qquad (22)$$

where only terms modified by the impurity are included in Equation (22). The notation $E_b^{\,l}$ is used to designate a case where there is one "impurity" in a bond attached to the nonmetal. Later E_b^{n}, $n = 0,1,2,3$, will be introduced as a generalization. The quantities that depend on the impurity are labeled with an i. Only the metallization and transfer energies are affected; the interbond overlap repulsion, the bond formation energy, and the promotion energies depend only on the atoms at the end of the bond in question. The portions of the metallization energy caused by the bonds adjacent to the metal ion are also unchanged.

If the bond lengths in the alloy are allowed to change from their pure crystal values, then extra terms will be added to Equation (22). This will complicate matters, and we shall try to see our way through the simpler calculation before adding this complication.

A useful collection of auxiliary equations is:

$$\frac{\partial V_2}{\partial d} = -\frac{2V_2}{d}, \tag{23}$$

$$\frac{\partial (V_2^2 + V_3^2)^{1/2}}{\partial d} = \frac{2\alpha_c^2}{d}(V_2^2 + V_3^2)^{-1/2}, \tag{24}$$

$$\frac{\partial U_-^b}{\partial d} = \frac{\alpha_c^2 \alpha_p}{1 + \alpha_p}\frac{U_-^b}{d} = \frac{\partial U_+^a}{\partial d}, \tag{25}$$

$$\frac{\partial U_-^a}{\partial d} = \frac{-\alpha_c^2 \alpha_p}{1 - \alpha_p}\frac{U_-^a}{d} = \frac{\partial U_+^b}{\partial d}, \tag{26}$$

and

$$\frac{\partial \epsilon_b}{\partial d} = \frac{2\alpha_c^2}{d}(V_2^2 + V_3^2)^{1/2} = -\frac{\partial \epsilon_a}{\partial d}. \tag{27}$$

Using these equations, Equation (22) becomes

$$\begin{aligned}\Delta E_b^{\,l} = 2V_{l-}^{\,2}(U_-^b)^2 \Bigg\{ & \frac{(U_-^{ai})^2}{\epsilon_b - \epsilon_a^i}\left[1 + \frac{\alpha_p(1-\alpha_p)}{2} - \frac{\alpha_c^2\sqrt{V_2^2 + V_3^2}}{2(\epsilon_b - \epsilon_b^i)}\right] \\ & + \frac{(U_-^a)^2}{2\sqrt{V_2^2 + V_3^2}}\left[1 + \frac{\alpha_p(1-\alpha_p)}{2} + \frac{\alpha_c^2}{4}\right] \\ & - 2V_{l-}^{\,2}(U_-^a)^2 \Bigg\{ \frac{(U_-^{bi})^2}{\epsilon_b^i - \epsilon_a}\left[\frac{\alpha_p(1+\alpha_p)}{2} + \frac{\alpha_c^2\sqrt{V_2^2 + V_3^2}}{2(\epsilon_b^i - \epsilon_a)}\right] \\ & + \frac{(U_-^b)^2}{2\sqrt{V_2^2 + V_3^2}}\left[\frac{\alpha_p(1+\alpha_p)}{2} - \frac{\alpha_c^2}{4}\right]\Bigg\} + \frac{\epsilon_{p+}^i - \epsilon_{p+}}{6}. \end{aligned} \tag{28}$$

While this is a bit complicated, it can be used to calculate $\Delta E_b^{\,l}$.

One can express ΔE_b^1 in terms of deviations of $V_2^{\,i}$ and $V_3^{\,i}$ from V_2 and V_3.

$$\delta_2 \equiv \frac{V_2^{\,i} - V_2}{V_2} \tag{29}$$

$$\delta_3 \equiv \frac{V_3^{\,i} - V_3}{V_3} \tag{30}$$

Then one can demonstrate that:

$$\sqrt{V_2^{\,i2} + V_3^{\,i2}} = \sqrt{V_2^2 + V_3^2}\left[1 + \alpha_c^2(2\delta_2 + \delta_3^2) + \alpha_p^2(2\delta_3 + \delta_3^2)\right]^{1/2}$$

$$= \sqrt{V_2^2 + V_3^2}\left[1 + \alpha_c^2\delta_2 + \alpha_p^2\delta_3 + \cdots\right], \tag{31}$$

$$\varepsilon_b - \varepsilon_a^{\,i} = \frac{\varepsilon_+ - \varepsilon_+^{\,i}}{2} - \sqrt{V_2^2 + V_3^2} - \sqrt{V_2^{\,i2} + V_3^{\,i2}}$$

$$= -\sqrt{V_2^2 + V_3^2}\left\{1 + \alpha_p\delta_3 + \left[1 + \alpha_c^2(2\delta_2 + \delta_2^2) + \alpha_p^2(2\delta_3 + \delta_3^2)\right]^{1/2}\right.$$

$$= -\sqrt{V_2^2 + V_3^2}\left[2 + \alpha_c^2\delta_2 + \alpha_p(1 + \alpha_p)\delta_3 + \cdots\right], \tag{32}$$

$$\varepsilon_b^{\,i} - \varepsilon_b = (\varepsilon_b - \varepsilon_a^{\,i}) + 2V_3\delta_3$$

$$= -\sqrt{V_2^2 + V_3^2}\left[2 + \alpha_c^2\delta_2 - \alpha_p(1 - \alpha_p)\delta_3 + \cdots\right], \tag{33}$$

$$\alpha_p^{\,i} = \alpha_p\left[1 - \alpha_c^2(\delta_2 - \delta_3) + \cdots\right], \tag{34}$$

$$\underline{U}^{bi} = \underline{U}^b\left[1 - \frac{\alpha_c^2\alpha_p}{2(1 + \alpha_p)}(\delta_2 - \delta_3) + \cdots\right], \tag{35}$$

$$\underline{U}^{ai} = \underline{U}^a\left[1 + \frac{\alpha_c^2\alpha_p}{2(1 - \alpha_p)}(\delta_2 - \delta_3) + \cdots\right], \tag{36}$$

and

$$\Delta E_b^{\,1} = \frac{-\alpha_c^{\,4} V_1^{\,-2}(1+\alpha_p)}{16\sqrt{V_2^{\,2}+V_3^{\,2}}}\left[\frac{(1+\alpha_p)}{4}\left(-3+6\alpha_p-8\alpha_p^{\,2}++5\alpha_p^{\,3}+11\alpha_p^{\,4}-12\alpha_p^{\,4}\right)\delta_2\right.$$

$$\left.+\left(-3-8\alpha_p+5\alpha_p^{\,2}-\alpha_p^{\,3}+\alpha_p^{\,4}\right)\delta_3+\ldots\right]+\left(\varepsilon^{i}_{p+}-\varepsilon_{p+}\right)/6. \qquad (37)$$

In fact, Equation (37) is not too useful since, for reasons that will become evident presently, one actually needs terms in $\delta_2^{\,2}$ and $\delta_3^{\,2}$. Because those terms will be a mess, it is easier to calculate $\Delta E_b^{\,1}$ from Equation (28).

If the bond of interest is surrounded by η bonds ($\eta = 0,1,2,3$) containing "impurities", then the energy shift in this approximation where bond lengths are fixed is

$$\Delta E_b^{\eta} = \eta \Delta E_b^{\,1}. \qquad (38)$$

The total bond energy of an $A_{1-x}B_x$ alloy E_{bT} is given by the sum over the individual bond energies at each bond n.

$$E_{bT}\sum_n E_{bn} = N\left[(1-x)\bar{E}_{bA} + x\bar{E}_{bB}\right] \qquad (39)$$

where

$$\bar{E}_{bA} = E_{bA} + \sum_{\eta=0}^{3} \eta \Delta E_{bA}^{\,1}\, P_{A\eta}, \qquad (40)$$

and

$$\bar{E}_{bB} = E_{bB} + \sum_{\eta=0}^{3} \eta \Delta E_{bB}^{\,2}\, P_{B\eta}. \qquad (41)$$

The quantities $P_{A\eta}$ and $P_{B\eta}$ are the probabilities that η cations of the opposite species (impurities) to the one on the designated bond are located on the adjacent bonds connected to the anion. These probabilities are binomial distributions if there is no tendency to cluster.

$$\begin{aligned} P_{A0} &= (1-x)^3 &&= P_{B3} \\ P_{A1} &= 3x(1-x)^2 &&= P_{B2} \\ P_{A1} &= 3x^2(1-x) &&= P_{B1} \\ P_{A3} &= x^3 &&= P_{B0}. \end{aligned} \qquad (42)$$

Note that

$$\sum_{\eta=0}^{3} \eta P_{A\eta} = 3x, \tag{43}$$

and

$$\sum_{\eta=0}^{3} \eta P_{B\eta} = 3(1-x), \tag{44}$$

so one has

$$\overline{E}_b \equiv \frac{E_{bT}}{N} = (1 - x)E_{bA} + xE_{bB} + 3x(1 - x)\left[\Delta E_{bA}{}^{1} + \Delta E_{bB}{}^{1}\right]. \tag{45}$$

All terms that tend to produce contributions to $\Delta E_{bA}{}^{1}$ and $\Delta E_{bB}{}^{1}$ that are of equal magnitude but opposite sign will cancel from the average energy per bond. These terms may, however, make contributions to other properties; e.g., those like strain constants that depend on higher powers of individual bond energies. The transfer energy is an example of a term that contributes to $\Delta E_{bA}{}^{1}$ and $\Delta E_{bB}{}^{1}$ but not to their sum. In fact, all the terms written explicitly in Equation (37) have this character since they depend linearly on δ_2, δ_3, and $\left(\varepsilon_{p+}^{i} - \varepsilon_{p+}\right)$.

Table 3-1 contains our present best estimates of the effective ε_s and ε_p deduced from extraction and excitation energies. These values still differ from experiment by ~5% for Hg and Cd and by ~10% for Zn. Therefore, they need to be improved before accurate bond energies can be calculated. The pure compound bond energies and other important parameters are collected in Table 3-2. Finally, the changes in bond energy caused by forming alloys are given in Table 3-3. The theory can be generalized so the meaningful pseudobinary alloy blanks in Table 3-3 can be filled.

While the numbers in the tables are inaccurate, the trends are mostly correct. The one exception is the bond energy of Zn, which once the ε_s and ε_p energies are correct will have a larger ionic contribution and be larger than that of CdTe.

There are several important trends in the tables. First note that the HgTe bond is destabilized by the addition of CdTe, but slightly stabilized by adding ZnTe. This occurs because there is a net charge transfer from Hg to Cd in a HgCdTe alloy, but the charge transfer in HgZnTe is from Zn to Hg. This trend is a consequence of the relative magnitude of the Hg, Cd, and Zn hybrid energies listed in Table 3-1. The normal trend as one goes from light to heavy

Table 3-1. Present Best Estimates of s,p and Hybrid State Energies, in eV

MATERIAL	ε_s	ε_p	ε
Hg	-10.946	-4.872	-6.390
Cd	-9.611	-4.784	-5.991
Zn	-10.224	-4.920	-6.246
Te	-19.620	-9.824	-12.273
Se	-22.473	-10.945	-13.827
S	-22.648	-11.847	-14.547

Table 3-2. Parameters Contributing to the Energy per Bond, in eV

MATERIAL	d [Å]	V_2	V_3	$-V_1^+$	$-V_1^-$	$(\varepsilon_{p^+} - \varepsilon_{p^-})/2$	E_b
HgTe	2.797	3.13	2.933	1.520	2.425	2.481	-0.478
CdTe	2.805	3.11	3.162	1.230	2.425	2.564	-0.924
ZnTe	2.643	3.51	2.692	1.489	2.425	2.425	-0.740
HgSe	2.635	3.53	3.720	1.520	2.882	3.039	-0.909
CdSe	2.62	3.57	3.949	1.230	2.882	3.123	-1.438
ZnSe	2.455	4.07	3.479	1.489	2.882	2.782	-1.200
HgS	2.543	3.79	4.080	1.520	2.700	3.490	-1.264
CdS	2.527	3.84	4.309	1.230	2.700	3.574	-1.821
ZnS	2.406	4.23	3.839	1.489	2.700	3.233	-1.433

Table 3-3. Shifts in the Bond Energies due to a Single Neighboring Metal Impurity ΔE_b^1, in eV

	IMPURITY								
	HgTe	CdTe	ZnTe	HgSe	CdSe	ZnSe	HgS	CdS	ZnS
HgTe	---	0.0600	-0.149						
CdTe	-0.0606	--	-0.211						
ZnTe	0.145	0.202	--						
HgSe				---	0.0527	-0.158			
CdSe				-0.0528	--	-0.211			
ZnSe				0.154	0.205	--			
HgS							---	0.0455	-0.134
CdS							-0.0456	--	-0.180
ZnS							0.132	0.177	--

elements in a column is for the atomic s-state extraction energies to decrease. However, at Hg there is a reversal because of the relativistic terms. Hence the s-state energies of Zn are low, increase going to Cd, and then decrease once more in Hg to about equal those in Zn. The p-state energies are all nearly the same. The third and possibly most important trend arises from the fact that the ZnTe bond length is smaller than that of CdTe, so V_2 is larger.

This d or V_2 dependence is quite important since the coefficient C_{44} in tetrahedrally bonded solids is shown by Harrison[2] to vary at least at d^{-5} and possibly much faster ($\sim d^{-11}$). The activation energy to form dislocations is mostly due to bond angle distortions and is proportional to C_{44}.[3] Hence, decreasing d by 10% can change the activation energy for dislocation formation by more than 60%. Thus one expects the dislocation formation energy of ZnTe to be significantly higher than that of CdTe. Hence, $Hg_{1-x}Zn_xTe$ should be a more stable compound than $Hg_{1-x}Cd_xTe$. These comments still must be made more quantitative.

[2]Harrison, ibid.
[3]C. Kittel, Introduction to Solid State Physics, 5th Ed., (Wiley, New York, 1976), Ch. 18.

(This Page Intentionally Left Blank)

Section 4

CHANNELED IMPLANT

CHANNELED IMPLANT TASK

This task is aimed at identification of the mechanism of the electrically active implant damage seen in HgCdTe. As has been well documented, implantation into HgCdTe always results in n-type activity.[1] When junction diodes are formed by ion implantation, the junction location is significantly deeper than expected from the ion profile itself. The actual ion profiles produced have been shown to closely follow that predicted by the LSS theory, for an expected combination of electronic and nuclear stopping.[2] In this task both random and channeled implants will be produced and their ion profiles compared to profiled electronic activity. These will be compared to TEM examination at different depths to visualize the damage profile and mechanism. Ions have been chosen for study which are likely to produce donor, acceptor or isoelectronic activity on either the cation or anion site. These are listed in Table 4-1.

Table 4-1

ION	HYPOTHETICAL ACTIVITY	REPLACEMENT SITE
H	p	Cation
Li, Na, Cn	p	Cation
Zn, Be	Isoelectronic	Cation
B, Aℓ	n	Cation
N, P, As	p	Anion
O, S	Isoelectronic	Anion
F, Cl, Br	n	Anion
Ar	Inert	Anion

In addition, particular attention will be paid to H^+ and D^+ implants because of their low mass (hence low potential damage) and their success in producing buried channels by inactivating other implants in Si and GaAs, for example.[3-4]

The electrical activity will be profiled by use of C-V, Hall, possibly Far IR spectroscopy (FIR).[1] Specific trap parameters will be measured by DLTS with ion profiles obtained by use of SIMS (Charles Evans).

We have prepared several lots of bulk SSR-grown HgCdTe at SBRC with different surface preparations. Various lots are unannealed and annealed and etched in both the standard way (removes <1 μm) and for much longer to remove ~20 μm of the surface. Samples with these surface treatments have been implanted and a few have been profiled. We plan to add surfaces covered with thin layers of SiO_2 to this list for future evaluation.

We have channeled a few ions of several types of (110) HgCdTe surfaces and have profiled the depth distributions by SIMS with successful results. Selected samples have been sent to Stanford (S. Cole) for TEM analysis and to Evans & Associates (M. Strathman) for RBS analysis for measurement of damage magnitude and depth distribution.

One goal is to find the best n- and p-dopant ions for channeled implantation in HgCdTe, causing less damage during implant and creating doping profiles deeper than the native defected surface layer. Ultimately our goal is to create n and p regions that are chemically doped rather than defect/compensation doped for use in device fabrication.

We channeled B ions in surface in bulk SSR-grown (110) HgCdTe prepared in three ways:

a. unannealed plus standard etch,

b. annealed (350°C for 3 weeks) plus standard etch, and

c. as in (b) plus a deep etch that removed ~22 μm additional HgCdTe from the surface.

The results are shown in Figure 4-1, which is a SIMS profile of B. The two annealed but differently etched samples have about the same profile. The profile for the unannealed sample shows a greater random component (shallower) and a poorer channel component (deeper). We estimate that about 20% fewer ions were channeled in this sample (implant). Either the sample has a blocked lattice channel (poor crystal quality) or the implant was not well enough aligned. We should perform another channeled implant to verify this conclusion, but the preliminary result indicates that annealing produces a better ordered lattice and therefore better channeled profiles. The channeled boron depth distribution for 200 keV ions is about 2.3 μm depth and quite abrupt. It would create a sharp junction (n in p) if chemical doping were effective. The "doping density" is about 10^{17} cm^{-3} for the 3×10^{13} cm^{-2} implant fluence.

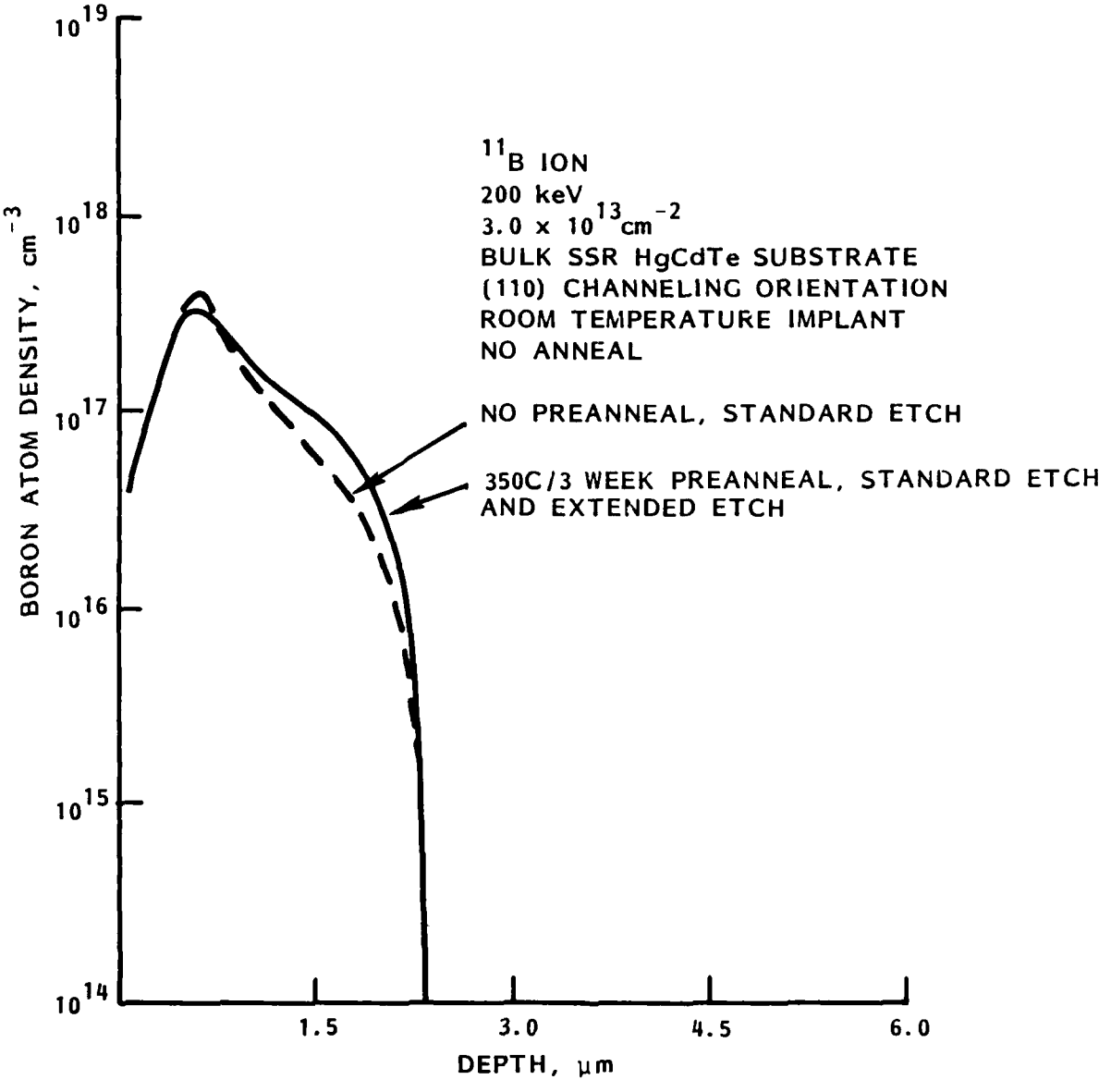

Figure 4-1. Ion Profile (from SIMS) of B Implanted into (110) Face of HgCdTe, with Preimplant Anneal Compared to No Preimplant Anneal

In Figure 4-2 we show SIMS profiles for three channeled ions, the B from Figure 4-1, plus Aℓ and Na. Na is a potential p dopant in HgCdTe and Aℓ a potential n dopant. B is a relatively small ion that has relatively high electronic stopping (the predominant stopping mechanism for channeling), so its depth is relatively shallow but the doping density is high. Na and Aℓ are larger ions but have low electronic stopping so their depths are deeper, but the achievable doping densities (at room temperature) are lower. Most other ions of interest at 150 or 200 keV will have depths and doping densities between those shown for 200 keV B and for Na and Aℓ. The depths for Na and Aℓ are quite deep for the modest 200 keV ion energy, being ~10 μm or greater. Hopefully these depths are deeper than the electrical effects of the native and implantation-induced defects. Little damage is done by the well channeled ions (that is, those that penetrate deeply) in the deep "junction region".

Other potential n and p dopants that are light ions (create less damage) are, for p, Li and K, and for n, P, F, Cℓ, and possibly N. Based on size and electronic stopping, F will be fairly deep, Cℓ fairly shallow, N would be like B, P and Li moderate, deeper than B, but shallower than Aℓ (see Figure 4-2). We will attempt to measure channeled profiles for Li, K, P, F, Cℓ, and possibly N during the next six months.

All HgCdTe prepared for channeling studies is SSR grown and (110) oriented. Material for other studies are both zone melt and SSR material, unoriented and (111) oriented. X values vary from 0.19 to 0.35.

The detection limits seen in Figure 4-2 of ~10^{13} cm^{-3} for Aℓ and Na are ten times better than for B (and for most other ions) because the SIMS sensitivities for Na and Aℓ are ten times better than for B, and many other ions.

Acknowledgements

We gratefully acknowledge the assistance in this work of V.A. Cotton. Also, the many helpful discussions with T.N. Casselman, R.E. Kvaas and D.R. Rhiger. We especially acknowledge the outstanding efforts made by R.E. Cole and C.R. Curtis in growing the bulk crystals used for all tasks in this study, and to A.E. Stevens for the creative work and extraordinary effort which facilitated the growth and transfer in an inert atmosphere of LPE HgCdTe.

We are also appreciative of the many collaborators which have aided this work, specifically, W.A. Harrison, A-B Chen and P.M. Raccah. This work is sponsored by R.A. Reynolds of DARPA and the technical monitor is B. Sumner of NV&EOL.

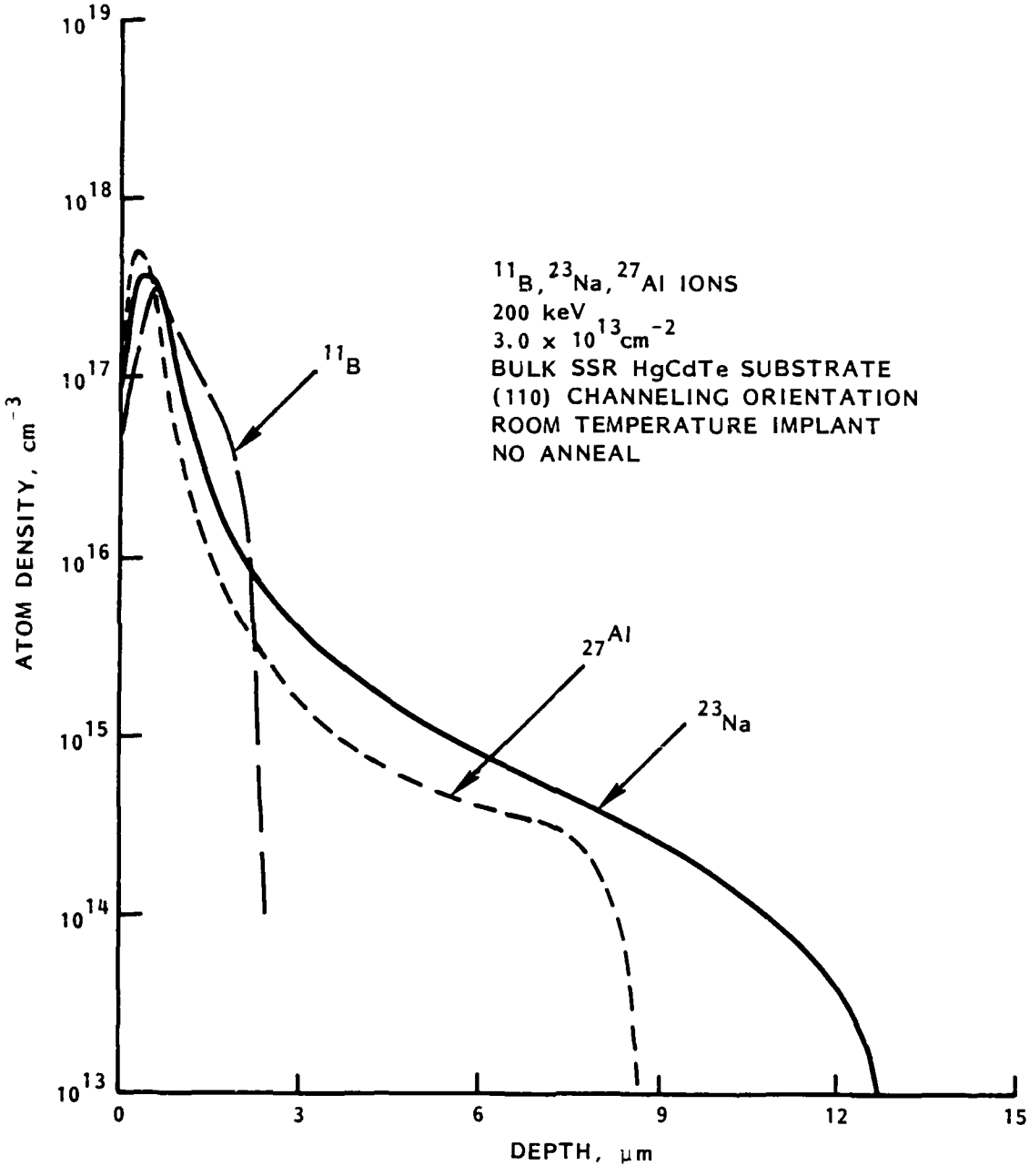

Figure 4-2. Ion Profiles (from SIMS) of B, Na, and Al in (110) Face of HgCdTe, Showing Depths Available with Channeling

REFERENCES
(Section 1)

1. HgCdTe Surface Study Program Final Report, Report Number 83-1069, DARPA Contract MDA-903-80-C-0496.

2. J.A. Wilson, V.A. Cotton, J.A. Silkerman, O. Lacer, W.E. Spicer and P. Morgen, J. Vac. Sci. Tech., A1 (1983), 1719.

3. B.K. Janorsek, R.C. Carscallen and P.A. Bertrand, J. Vac. Sci. Tech., A1 (1983), 1723.

4. P.M. Raccah, U. Lee, J.A. Silberman, W.E. Spicer and J.A. Wilson. Appl. Phys. Lett., 42 (1983), 374.

5. A.S. Grove and D.J. Fitzgerald, Solid State Electronics, 9 (1966), 783.

6. S.T. Hsu, Solid State Electronics, 13 (1970), 843.

7. S.P. Tobin, S. Iwasa and T.J. Tredwell, IEEE Trans on Electronic Devices, 27 (1980), 43.

8. S.M. Sze, Physics of Semiconductor Devices, (Wiley-Interscience, 1969), 366.

9. D.R. Rhiger and R.E. Kvaas, J. Vac. Sci. Tech., 21 (1982), 168.

10. B.K. Janorsek and R.E. Carscallen, J. Vac. Sci. Tech., 21 (1982), 442.

11. P. Morgen, J.A. Silberman, I. Lindau, W.E. Spicer and J.A. Wilson, J. Vac. Sci. Tech., 21 (1982), 161.

REFERENCES
(Section 4)

1. J. Baars, A. Hurrle, W. Rothemund, C.R. Fritsche and T. Jakobus, J. Appl. Physics, 53 (1982), 1461.

2. K.J. Riley, A.H. Lockwood and P.R. Bratt, Proc. Joint Meeting IRIS Specialty Group on Infrared Detectors and Imagery, 1 (1978), 363 (DDC AD B033464).

3. D.C. D'Avanzo, IEEE Trans. on Elect. Dev., 29 (1982), 1051.

4. K. Steepler, G. Rearnaley and A.M. Stoneham, Appl. Phys. Lett., 36 (1980), 981.

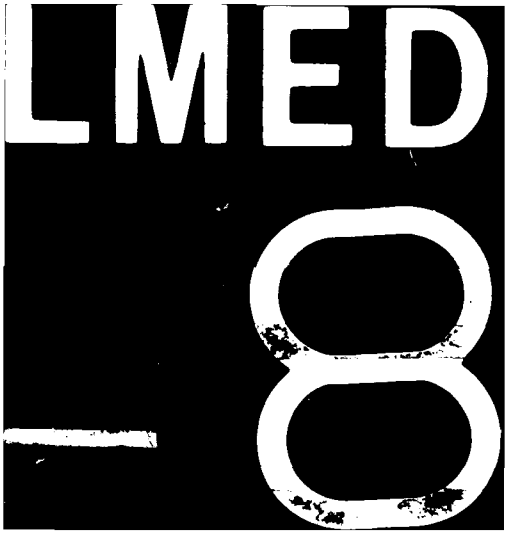
LMED
8